UNIVERSITY OF CALIFORNIA, SAN DIEGO

Micromagnetic modeling of spintronic devices for memory and recording applications

A dissertation submitted in partial satisfaction of the
requirements for the degree
Doctor of Philosophy

in

Electrical Engineering (Nanoscale Devices and Systems)

by

Majd Kuteifan

Committee in charge:

Professor Vitaliy Lomakin, Chair
Professor Prabhakar Bandaru
Professor Eric E. Fullerton
Professor Boubacar Kanté
Professor Vlado Lubarda

2018

The dissertation of Majd Kuteifan is approved, and it is acceptable in quality and form for publication on microfilm and electronically:

_____

_____

_____

_____

_____

Chair

University of California, San Diego

2018

TABLE OF CONTENTS

LIST OF FIGURES

LIST OF TABLES

ACKNOWLEDGEMENTS

I thank my advisor Vitaliy Lomakin for the advice and guidance he provided during my years at UCSD. His constantly good mood and great support since my first internship in 2012 have been an invaluable help and motivation for my doctoral studies. From barbecues to paintball and April's fool pranks, he also knows how to create essential links and reinforce collaboration within our group. His deep knowledge in the diverse areas connected to micromagnetic simulations and his ability to always look at the bright side of things make him the best possible advisor I could have asked for.

I would like to thank Professor Stéphane Mangin for sending me to this first internship to UCSD in 2012 and for giving me the chance to spend some time in his lab in Nancy during my PhD. I also thank Professor Eric Fullerton for his guidance and for the time I spent in his group.

From Professor Lomakin's group I would like to thank Marko Lubarda who helped me get accustomed to the new world that micromagnetics was to me and for the fruitful collaborations that ensued. I thank Ruinan Chang for his help on numerical methods, and especially in the implementation of Dzialoshinskii-Moriya interactions. I would like to thank Iana Volvach for the help in MRAM modelling and all the Ukrainian food. I am grateful to Sidi Fu for his numerous pieces of advice on programming, GPU-computation and the tennis games. I want to thank Simon Couture for his help on theoretical electromagnetism and for providing some French language conversation. I further aknowledge Marco Menarini for the interesting discussions and board games. I would also like to thank Jean-Baptiste Puel, Marion Fuhrmann, Alain Truong, Xueyang Wang, Zhuonan Lin and Philippe Scheid.

I have met many people from other groups at UCSD who made these five years of PhD studies fly faster than I could have imagined. I would like to thank Charles-Henri Lambert for the Alsatian connection, Soraya Hannane for the good mood, games of Sun Tzu and improving my Swiss-French vocabulary, Sohini Manna for the music discussions, Mohammed El-Hadri for the football games and my roommate Quentin Gauthier.

From my internships at Samsung, I am very grateful to Dima Apalkov, Sue Wang, Alexey Khvalkovskiy and all my other colleagues from the NMT group for always being so helpful and making me feel part of the team.

Chapter 3 is a more detailed version of the work presented in a journal article [1] written in collaboration with M. V. Lubarda, S. Fu, R. Chang, M. A. Escobar, S. Mangin, E. E. Fullerton and V. Lomakin.

Chapter 5 is based on the contribution I have brought to the journal article authored by J. Sampaio [2], with the following co-authors: A. V. Khvalkovskiy, M. Cubukcu, D. Apalkov, V. Lomakin, V. Cros and N. Reyren.

Finally, I am grateful to my family for their infallible support.

VITA

2012	MS in Engineering, École Nationale Supérieure des Mines de Nancy, France
2018	Ph. D. in Electrical Engineering (Nanoscale Devices and Systems), University of California, San Diego

PUBLICATIONS

M. Kuteifan, M. V. Lubarda, S. Fu, R. Chang, M. A. Escobar, S. Mangin, E. E. Fullerton and V. Lomakin, "Large exchange-dominated domain wall velocities in antiferromagnetically coupled nanowires", *AIP Advances*, 6, 2016

M. Kuteifan, C.-H. Lambert, M. V. Lubarda, V. Lomakin, E. E. Fullerton and S. Mangin, "Spin transfer torque magnetization reversal in a hard/soft composite structures", *AIP Advances*, forthcoming

J. Sampaio, A. V. Khvalkovskiy, M. Kuteifan, M. Cubukcu, D. Apalkov, V. Lomakin, V. Cros and N. Reyren, "Disruptive effect of Dzyaloshinskii-Moriya interaction on the magnetic memory cell performance", *Appl. Phys. Lett.*, 108, 2016

A. Singh, S. Gupta1, M. Kuteifan, M. Lubarda, V. Lomakin and O. Mryasov, "Effect of interlayer exchange coupling parameter on switching time and critical current density in composite free layer", *J. Appl. Phys.*, 115, 2014

S. Fu, R. Chang, S. Couture, M. Menarini, M. A. Escobar, M. Kuteifan, M. Lubarda, D. Gabay and V. Lomakin, "Micromagnetics on high-performance workstation and mobile computational platforms", *J. Appl. Phys.*, 117, 2015

CONFERENCE PRESENTATIONS

M. Kuteifan, M. V. Lubarda, S. Fu, R. Chang, M. A. Escobar, S. Mangin, E. E. Fullerton and V. Lomakin, "Study of domain wall motion in antiferromagnetically coupled nanowires", *2013 Annual Conference on Magnetism and Magnetic Materials*, Denver, CO, USA, Nov. 4 – Nov. 8, 2013

M. Kuteifan, M. V. Lubarda, S. Fu, R. Chang, M. A. Escobar, S. Mangin, E. E. Fullerton and V. Lomakin, "Ferromagnetically and antiferromagnetically coupled nanowire multilayers for higher peak velocities, improved mobility and greater stability of domain walls for future memory and logic applications", *2014 Annual Conference on Magnetism and Magnetic Materials*, Honolulu, HI, USA, Nov. 3 – Nov. 7, 2014

M. Kuteifan, C.-H. Lambert, M. Lubarda, S. Mangin and V. Lomakin, "Dynamics of domain wall oscillators", *13th Joint MMM-Intermag Conference*, San Diego, CA, USA, Jan. 11 – Jan. 15, 2016

M. Kuteifan, C.-H. Lambert, M. Lubarda, S. Mangin and V. Lomakin, "Spin transfer torque magnetization reversal in hard/soft composite structures", *2016 Annual Conference on Magnetism and Magnetic Materials*, New Orleans, LA, USA, Oct. 31 – Nov. 4, 2016

M. Kuteifan, C.-H. Lambert, M. Lubarda, S. Mangin and V. Lomakin, "Spin transfer torque magnetization reversal in hard/soft composite structures", *International Workshop and School on Spin Transfer*, Nancy, France, Sep. 19 – Sep. 23, 2016

M. Kuteifan and V. Lomakin, "Forward flux sampling method with spin transfer torque for the calculation of thermal relaxation times of free layers", *2017 Annual Conference on Magnetism and Magnetic Materials*, Pittsburgh, PA, USA, Nov 6. – Nov. 10, 2017

ABSTRACT OF THE DISSERTATION

Micromagnetic modeling of spintronic devices for memory and recording applications

by

Majd Kuteifan

Doctor of Philosophy in Electrical Engineering (Nanoscale Devices and Systems)

University of California, San Diego, 2018

Professor Vitaliy Lomakin, Chair

Magnetic materials and nanoscale devices are at the heart of data storage technologies, from decades-old hard drives to future technologies such as magnetoresistive random access memory or racetrack memory. Driven by the constantly increasing demand for more storage space and performances, the focus has shifted from magnetic field-based applications to spin current-based applications. This thesis discusses some of the challenges faced when studying interactions between electrical currents and magnetic materials. It starts with an introduction to micromagnetics and the description of the main magnetic interactions. It then focuses on racetrack memories and details the advantages of antiferromagnetically coupled nanowires. The next chapters are dedicated to spin-valves, including a study of composite free-layers, the

influence of Dzialoshinskii-Moriya interactions on the performance of memory cells, and the forward flux sampling method to predict the switching probability under non-zero temperature. All of these chapters contain work done on the FastMag micromagnetic simulation software, developed in-house. Some general ideas and details on the implementation of magnetic fields and methods for simulation are also provided.

Chapter 1

Introduction

Technologies based on magnetic materials have a prominent role in our daily environment. With the emergence of computers and other electronic devices, magnetic-based hard drives have become the main tool for data storage and have been uncontested for several decades. With the exponentially increasing demand for storage capacity coming together with people's modern data consumption habits such as high definition video and extensive use of social networks, new technologies are constantly challenging the market and trying to offer better performances. The recent years have seen the emergence of solid states hard drives as a serious competitors to hard-drives, first in terms of access speed and also in terms of storage capacity. These shifts in technology have led the scientific community to look towards new kinds of data storage devices as it becomes increasingly harder to improve the performances of classical hard drives. Many ideas and prototypes have sprouted in the last decade, all hoping to push back the performance limits of current designs. Among them, spintronic devices are implements that are taking advantage of the interactions between magnetic materials and electric currents. Several designs based on this technology are envisioned and are research topics for a large part of the scientific community, such as spin-transfer torque magnetoresistive random access memory (STT-MRAM), domain wall-based racetrack memory or skyrmion-based racetrack memory.

Simulation is an essential tool when it comes to exploring the possibilities offered by spintronic technologies. Building and testing complex nanoscale devices is fastidious, which is why robust models are needed to fasten the R&D process. This is the field of micromagnetic modeling. The FastMag code developed at UCSD brings solutions to address these issues. Taking advantage of high-performance Graphics Processing Units (GPUs) and latest algorithms, the FastMag micromagnetic solver can compute the dynamics of magnetization within nanoscale to microscale magnetic materials and devices efficiently. It is a flexible software that offers a wide range of possibilities, from simulating current interactions to complex write head modeling, and allows for time-domain simulation as well as other algorithms used to compute energy barriers or thermal stability. However, the world of scientific research is progressing rapidly and new phenomena are regularly given increasing interest. It is important for simulation software to stay up to date to be able to answer the needs created by these breakthroughs.

This manuscript presents how the interactions between electrical currents and the magnetization is handled by a simulation tool like FastMag, and some of the challenges that can be addressed with this feature. Through different devices and designs, advantages and drawbacks of some of the previously mentioned technologies are evaluated and studied. This work focuses on three aspects: study of the physics and analytical models of different problems, numerical implementation and calculations, and modeling of different types of devices such as STT-MRAM or racetrack memory. This manuscript is divided in fours main chapters. Chapter 2 reiterates the basic knowledge of micromagnetics focusing mainly on the expression of the most important interactions that are evaluated in most models. It gives some insight into how these interactions are implemented in a finite-element software such as FastMag and what the challenges are when it comes to efficiency and performance. Chapter 3 discusses a proposed design to increase the performance and velocity of current-driven domain wall motion in nanowires, one of the main candidates studied for racetrack memory. The proposed structure of an antiferromagnetically coupled nanowire exhibits interesting properties that are promising for future applications. Chapter 4

studies the behavior of a composite free layer structure under current in terms of switching as well as oscillations. The switching efficiency defined as the ratio between the thermal stability and the critical switching current of a magnetic layer is studied as a function of the composition of the composite sublayers. This is the main characteristic that should be improved in the future generations of STT-MRAM to achieve more cost-efficient and more reliable devices. Chapter 5 addresses the influence of Dzyaloshinskii-Moriya interactions on the stability of STT-MRAM dots. Finally, Chapter 6 discusses how the forward flux sampling method can be used to study the response of the thermal stability of a magnetic layer to an applied current. This method also allows the attempt frequency of the thermal activation of magnetic layers to be extracted.

Chapter 2

Elements of micromagnetics

Different approaches are possible to predict the behavior of a magnetic system. The choice depends on the nature of the system and the properties at play. Ideally, all problems could be described using an atomistic formulation, thus perfectly resolving all interactions within the material. However, for performance and resource considerations, other approaches have to be considered. Micromagnetics is a discipline that predicts and studies the interactions between magnetic particles at the mesoscopic scale. Its foundations were laid down by William F. Brown whose equations can be used to find equilibrium magnetization configurations from a set of continuous material parameters [3]. The Landau-Lifshitz-Gilbert (LLG) equation is commonly used to describe the dynamics of a magnetic system at that scale. The energies related to the different magnetic interactions are calculated based on input material parameters and give rise to fields such that the system tends to minimize its total energy in presence of damping. Various iterations of the LLG equation exist depending on the interactions taken into consideration. Optional terms can include effects related to currents, interfaces or interactions that are often regarded as negligible. This chapter will describe the main features of micromagnetics and give some insight into a few specific fields relevant to this work.

2.1 Problem modeling

Micromagnetics is a discipline that focuses on the simulation of magnetization dynamics and the first step to any simulation work is to generate the model that is to be studied. In our case this model consists of a mesh that discretizes a volume representing a part of material or a device. Generally the model size can be of the range of a few nanometers to a hundred of microns and the distance between the nodes of the mesh spans from less than a nanometer to tens of nanometers depending on the application. The system is typically discretized into tetrahedrons that form links between the nodes. These links are important to propagate proximity interactions and compute important simulation components such as gradient or laplacian matrices.

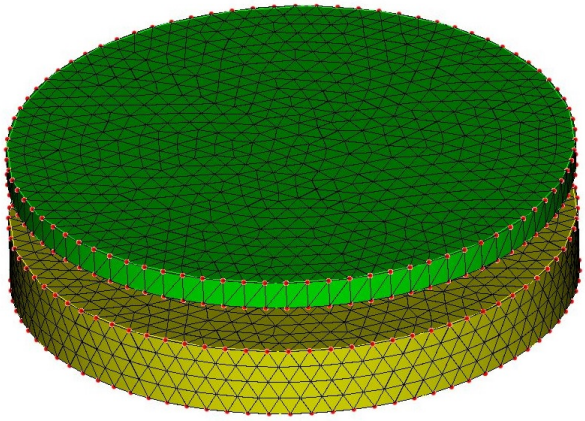

Figure 2.1: A mesh of a model containing two cylinders. Each node corresponds to a magnetic moment whose time evolution is to be computer by the numercal solver.

Each node represents a magnetic moment whose evolution is to be computed. Depending on the interactions that are considered, the magnetic moments can interact with each other and their respective behaviors depends on their neighbors. These interactions induce limits to consider when it comes to creating the model and the mesh. Indeed some of them can introduce critical scales and effects that require a fine enough mesh size to be resolved, the main one being the exchange interaction, which typically has a critical length that can be defined as $l_{ex} = \sqrt{A_{ex}/K}$, where the exchange constant A_{ex} and the anisotropy energy density K are material parameters.

The number of nodes allowed by the simulation depends on the amount of available memory, as well as the computation power required to obtain results in a reasonable time frame. Models can include up to tens of millions of nodes in the case of very large simulations such as hard drive write head modeling. However the total size of the model is limited by a combination of the upper mesh size limit imposed by the correct resolution of all interactions and the upper node count limit imposed by the hardware.

2.2 Landau-Lifshitz-Gilbert equation

The equation describing the dynamics of magnetization in micromagnetics considers interactions through the form of an effective magnetic field in its most basic expression. In this case two main driving factors are taken into account: the precession of the magnetic moment around the effective field and its damping (energy loss) towards the same effective field. This equation is the Landau-Lifshitz-Gilbert (LLG) equation and is expressed as [4, 5]:

$$\frac{d\mathbf{M}}{dt} = -\gamma \mathbf{M} \times \mathbf{H} + \alpha \mathbf{M} \times \frac{d\mathbf{M}}{dt}, \tag{2.1}$$

where $\mathbf{M}$ is the magnetic moment of the considered node, γ is the gyromagnetic ratio, α is the damping constant and $\mathbf{H}$ is the effective magnetic field at that node.

This equation corresponds to the theorem of conservation of angular momentum applied to the magnetic moments. The gyromagnetic ratio γ is the link that converts angular momentum in the equation into magnetic moments as it is defined as:

$$\gamma = \frac{\mu}{L}, \tag{2.2}$$

where μ is the magnetic moment of a body and L is its angular momentum.

The first term of the right-hand side of (2.1) is the total torque applied on the system. It

describes the precession of the magnetic moments about the effective field. The second term of the right-hand side is the damping term representing the energy loss and parametrized by α. The magnitude of the damping depends on the environment surrounding the spins and its origin can be of different natures. One main factor to take into consideration is the interaction between the spins and the heat bath. The energy lost by the system mostly goes to the lattice under the form of heat as it seeks to reach thermal equilibrium[6].

The effective field $\mathbf{H}$ depends on the state of the magnetization and the LLG equation is non-linear. In general, it has to be solved using time-stepping schemes such as Euler, Heun or backward differentiation formula[7, 8]. Under this form, the LLG equations is implicit, i.e. the $\frac{d\mathbf{M}}{dt}$ term is present on both the left-hand side and the right-hand side. In order to be able to integrate (2.1) with a simple time solver, it can be made explicit. We can do so by replacing the right-hand side occurrence of $\frac{d\mathbf{M}}{dt}$ with the whole right-hand side, leading to:

$$\frac{d\mathbf{M}}{dt} = -\gamma\mathbf{M}\times\mathbf{H} + \alpha\mathbf{M}\times\left(-\gamma\mathbf{M}\times\mathbf{H} + \alpha\mathbf{M}\times\frac{d\mathbf{M}}{dt}\right). \tag{2.3}$$

We know that $\mathbf{M}$ and $\frac{d\mathbf{M}}{dt}$ are perpendicular so we can use the identity:

$$\mathbf{M}\times\mathbf{M}\times\frac{d\mathbf{M}}{dt} = -\frac{d\mathbf{M}}{dt}, \tag{2.4}$$

allowing us to rewrite (2.3) into:

$$\frac{d\mathbf{M}}{dt} = -\frac{\gamma}{1+\alpha^2}\mathbf{M}\times\mathbf{H} - \frac{\alpha\gamma}{1+\alpha^2}\mathbf{M}\times\mathbf{M}\times\mathbf{H}. \tag{2.5}$$

This is the explicit form of the LLG equation.

The interactions that are considered as part of the effective field vary depending on the considered model. Some of them will be described in sections to follow. Some of them cannot be interpreted as effective fields and require additional torques to be added to (2.5). The LLG

equation would then be written as:

$$\frac{d\mathbf{M}}{dt} = -\frac{\gamma}{1+\alpha^2}\mathbf{M}\times\mathbf{H} - \frac{\alpha\gamma}{1+\alpha^2}\mathbf{M}\times\mathbf{M}\times\mathbf{H} + \mathbf{T}\,. \tag{2.6}$$

These additional terms can include spin-transfer torques which are described in more details in section 3.1.

2.3 Fundamental interactions

The effective field **H** from (2.1) represents the sum of the fields originating from the different interactions affecting the magnetic moments of the system. This section describes the fundamental interactions as usually encountered in micromagnetics. Indeed, this discipline focuses on emulating magnetic systems, and as though the range of interactions that can be included in the model is very large, most of them often are negligible and should be taken into account only if needed in order to save computational power. The most dominant interactions are: the Zeeman field, the diploar field, the magnetocrystalline anisotropy and the exchange field.

Interactions are usually described through their potential energy densities. When this energy density is known, the corresponding field can be calculated using:

$$\mathbf{H} = -\frac{dE}{d\mathbf{M}}\,. \tag{2.7}$$

We have analytical expression for the energies resulting from the different interactions. It is then convenient to derive the field associated to each interaction using (2.7) and sum them all up to get the total effective field.

2.3.1 Zeeman interaction

The Zeeman interaction is the one occurring between the magnetization of the system $\mathbf{M}$ and an external applied field $\mathbf{H}_{app}$ called Zeeman field. The potential energy of the magnetic system under an external field is written as (in the CGS system):

$$E = -\int_{\Omega} \mathbf{M} \cdot \mathbf{H}_{app} dV \,. \tag{2.8}$$

We note that E is minimized when $\mathbf{M}$ and $\mathbf{H}_{app}$ are oriented towards the same direction, meaning that magnetic moments tend to align with external magnetic fields, just like compasses.

$\mathbf{H}_{app}$ generally is an input value chosen by the user and it is directly added to the effective field $\mathbf{H}$.

2.3.2 Magnetostatic interaction

In a system made of several magnetic moments, we can consider that each of them is an independent dipole generating a magnetic field in the entire space. That means that each magnetic moment is interacting with each other magnetic moment through its dipolar field, also called magnetostatic field or demagnetizing (or demag) field. The field generated by a dipole, which can be thought of as a small magnetic domain of volume V, is:

$$\mathbf{H}_{dipole}(\mathbf{r}) = \frac{V}{4\pi} \frac{3\mathbf{r}\,(\mathbf{M} \cdot \mathbf{r})}{r^5} - \frac{\mathbf{M}}{r^3} \,, \tag{2.9}$$

where $\mathbf{M}$ is the magnetic moment of the dipole and $\mathbf{r}$ is the distance vector from the source to the considered point.

This field can be seen as an external field by other magnetic moments. Based on the formulation used in section 2.3.1, the magnetostatic energy of the whole system Ω can then be written:

$$E_{ms} = -\frac{1}{2}\int_{\Omega} \mathbf{M}\cdot\mathbf{H}_{dipole}dV\,, \tag{2.10}$$

or in the case of a discretized system with N magnetic moments:

$$E_{ms} = -\frac{1}{2}\sum_{i=0}^{N}\sum_{\substack{j=0\\ j\neq i}}^{N} V_i\mathbf{M}_i\cdot\mathbf{H}_{j,demag}|_i\,. \tag{2.11}$$

These complex interactions are very important in understanding the dynamic and static behavior of magnetization. One of their effects is to prevent the existence of magnetic charges when possible (fig. 2.2). This leads to magnetic moments rearranging themselves in a way such that they try to follow each others' field lines.

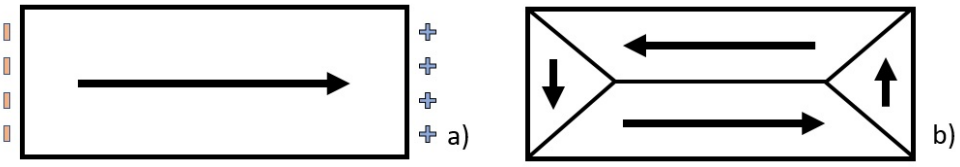

Figure 2.2: a) Magnetic structure within a metal bar if the magnetization is forced in the same direction, for example using a strong external field. Magnetic charges appear at both ends of the magnetic bar. b) If demagnetizing fields are the dominant interaction, the magnetization within the bar rearranges itself to make the magnetic charges disappear. The charges of the different spins within the material tend to compensate themselves.

This effect has many repercussions, mainly the appearance of magnetic domains. Because of the exchange interaction detailed in section 2.3.3, neighboring magnetic spins try to stay parallel to each other. However, when too many of them are consecutively parallel, their total dipolar field becomes very large in the direction opposite to their magnetization, leading the next neighbors to orient in the antiparallel direction as shown in fig. 2.3.

Computing the demagnetizing field is computationally very expensive. Because each magnetic moment has to interact with all other moments, the complexity of such a computation is $O(N^2)$, which can significantly slow down the simulation of large systems. Different methods are used to get around this issue. In many magnetic systems, the magnetization within a volume can

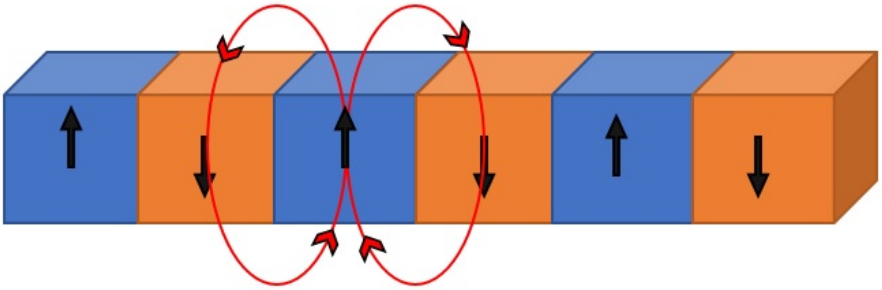

Figure 2.3: Magnetic domain structure due to dipolar fields. The dipolar field generated by the central domain on its neighbors is drawn. The neighbors tend to follow its field lines. However, the domains have locally uniform magnetization due to the exchange interaction.

be regarded as uniform. In these cases, magnetic charges appear at the surfaces of the volume, thus generating a demagnetizing field. To simplify the computation of this demagnetizing field, it is very common to use demagnetization factors. These factors depend on the shape of the considered volume and they allow for the computation of the demagnetizing field affecting it as follows: [9]

$$\mathbf{H}_{demag} = -\begin{bmatrix} N_{xx} & N_{xy} & N_{xz} \\ N_{yx} & N_{yy} & N_{yz} \\ N_{zx} & N_{zy} & N_{zz} \end{bmatrix} \mathbf{M}. \tag{2.12}$$

This matrix is called the demagnetization tensor. Its diagonal elements are positive and its trace is 1. The N_{ij} elements are called demagnetization factors. Since many simple systems have one or several axis or planes of symmetry, we find that in most cases $N_{ij,i\neq j} = 0$. For example, any axis going through the center of a sphere is an axis of symmetry. For this reason, the only non-zero elements of the demagnetizing tensor of a sphere are $N_{xx} = N_{yy} = N_{zz} = \frac{1}{3}$. This shows that there is no preferential direction for the orientation of the magnetization within a magnetic sphere: whatever the direction of $\mathbf{M}$ is, there will always be a demagnetizing field opposing it. In the case of an infinite thin film along the (x,y) plane, the only non-zero demagnetizing factor is $N_{zz} = 1$. If $\mathbf{M}$ has a non-zero component along z in this case, a demagnetizing field will oppose its direction,

pushing it into the plane. However, if $\mathbf{M}$ is in the (x,y) plane, no demagnetizing field exists. This field forces the magnetization to stay in the plane of the thin film. Based on (2.10) we can express the magnetostatic energy per unit volume of a thin film with perpendicular magnetization as:

$$E_{ms} = 2\pi M_s^2 \,. \tag{2.13}$$

There are general formulas to compute the demagnetizing factors of rectangular cuboids [10]. These will be particularly useful for section 3.5 when demangetization factors of the portion of the nanowire that includes the domain wall are mentioned.

In many cases, demagnetization factors can not accurately represent the dipolar field in the simulation: this is mostly due to non-uniform magnetization profile in the system. The field has to be precisely computed for each node using (2.11). In micromagnetic simulations, the position of all nodes is known in advance so we can precompute the relative positions and distance vectors of all combinations of nodes. Precomputation is important to save time and increase performance during the actual time-stepping. However, the value of $\mathbf{M}$ can not be known in advance. We need to create a demagnetizing tensor for each couple of nodes (i,j), based on the distance vector $\mathbf{r}_{ij}$ between these nodes, so that the algorithm does not have to re-calculate it on the fly when computing $\mathbf{H}_{demag}$. The demagnetizing tensor for (i,j) can be written based on (2.9):

$$D_{ij} = \frac{1}{4\pi \left\|\mathbf{r}_{ij}\right\|^3} \begin{bmatrix} 3r_{ij,x}^2 - 1 & 3r_{ij,x}r_{ij,y} & 3r_{ij,x}r_{ij,z} \\ 3r_{ij,y}r_{ij,x} & 3r_{ij,y}^2 - 1 & 3r_{ij,y}r_{ij,z} \\ 3r_{ij,z}r_{ij,x} & 3r_{ij,z}r_{ij,y} & 3r_{ij,z}^2 - 1 \end{bmatrix} , \tag{2.14}$$

and can be used to compute the demagnetizing field exerted by node j on node i as:

$$\mathbf{H}_{demag,j\to i} = D_{ij}\mathbf{M}_j \,. \tag{2.15}$$

The D_{ij} matrix is symmetric, so only six values need to be stored for each (i,j) couple. The total

demagnetizing field exerted by the N nodes on node i is then written:

$$\mathbf{H}_{demag,i} = \sum_{\substack{j=0 \\ j\neq i}}^{N} D_{ij}\mathbf{M}_j \,. \tag{2.16}$$

This operation has to be repeated for each node. Using this method, computing the demagnetizing field within a system of N nodes corresponds to realizing N^2 matrix-vector multiplications. However there are ways to accelerate its computation and reduce the complexity from $O(N^2)$ to $O(N\log N)$ [11, 12, 13, 14, 15, 16].

2.3.3 Exchange interaction

Bulk exchange interaction

The fact that magnetic spins arrange themselves into order to form a macroscopic magnetic moment is due to the exchange interaction. This interaction originates from the Coulomb interaction and the Pauli exclusion principle that states that two electrons can not occupy the same state. It is characterized by the exchange constant J_{ex} and its energy is related to the orientation of both spins $\mathbf{S}_1$ and $\mathbf{S}_2$ as follows:

$$E_{ex} = -J_{ex}\mathbf{S}_1 \cdot \mathbf{S}_2 \,. \tag{2.17}$$

The sign of J_{ex} determines the exchange type. If $J_{ex} > 0$ the material is ferromagnetic, meaning that the exchange energy E_{ex} is minimized when neighboring spins are aligned. In this situation, spins tend to form domains where they all point towards the same direction. If $J_{ex} < 0$ the material is ferrimagnetic. The exchange energy E_{ex} is minimized when neighboring spins are antiparallel (fig. 2.4). The exchange interaction is a short-ranged one. It dictates the orientation of cluster of spins, whereas other interaction like the magnetostatic one dictate the long-range order. This often leads to the creation of magnetic domains.

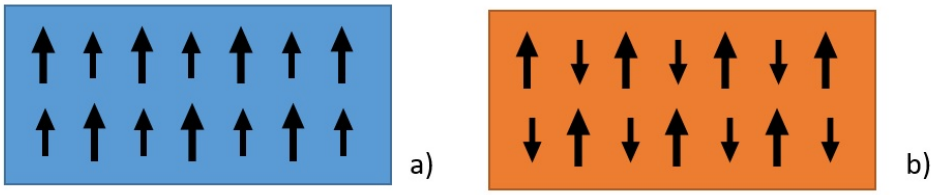

Figure 2.4: a) Ferromagnetic material ($J_{ex} > 0$) where neighboring spins are aligned. b) Ferrimagnetic material ($J_{ex} < 0$) composed of two atomic sublattices with opposite orientations.

(2.17) represents the atomistic formulation of the exchange interaction, also called Heisenberg Hamiltonian. It describes the exchange energy between two atoms. In micromagnetics, the model does not simulate the behavior of atoms. It rather integrates continuous energies over a shape discretized with finite elements. The continuous form of the exchange interaction has been derived from the Heisenberg Hamiltonian as [17]:

$$E_{ex} = \int_{\Omega} A \left(\nabla \mathbf{M}\right)^2 dV \,, \tag{2.18}$$

where A is the exchange energy density in erg/cm that depends on J_{ex}. It is important to note that since finite element modeling does not simulate atoms, ferrimagnetic exchange interactions (with $J_{ex} < 0$) can not be easily represented through this expression. Such systems could rather be represented as arrays of effective spins, where each magnetic moment is the average of the magnetic moments of two atoms of the opposite ferrimagnetic sublattices. Accurate representation of ferrimagnetic systems may require atomistic modeling that can directly implement (2.17) but whose performances are much worse.

We can write the exchange field from (2.7) and (2.17) as:

$$\mathbf{H}_{ex} = \frac{2A}{M_s} \nabla^2 \mathbf{M} \,. \tag{2.19}$$

We can once again take advantage of precomputation in this case. Since we already know the relative position of all nodes in the finite-element model, we can create a Laplacian matrix ∇^2 at

preprocessing time and store it in the memory. The only operation needed at run-time to calculate the exchange field is a multiplication between this ∇^2 matrix and the magnetization vector.

Interface exchange coupling

Interface exchange occurs when the magnetization of two materials is coupled through a thin interlayer (thickness of about 1nm). This effect is mediated by the Ruderman-Kittel-Kasuya-Yosida (RKKY) interaction. The magnitude of the coupling and even its sign can be changed by tuning the material and thickness of the interlayer, granting the ability to get both ferromagnetic and antiferromagnetic coupling [18, 19, 20]. This is the main mechanism of coupling allowing us to build the antiferromagnetically coupled nanowires discussed in chapter 3. The potential energy due to the RKKY interaction can be written as:

$$E_{RKKY} = -\int_S J_c \mathbf{M}_1 \cdot \mathbf{M}_2 dS, \tag{2.20}$$

where $\mathbf{M}_1$ and $\mathbf{M}_2$ are the normalized magnetization vectors on both sides of the interface and J_c is the interface exchange coupling energy density in CGS units of erg/cm^2. When $J_c > 0$ the interface coupling is ferromagnetic and the magnetizations of both layers tend to align towards the same direction. When $J_c < 0$ the coupling is antiferromagnetic and the magnetizations of both layers tend to take opposite directions. This is the case that is studied in chapter 3.

Implementing interface effects in micromagnetics requires specific methods. Indeed, the interlayer material is non-magnetic, thus it is not discretized and does not carry any connection information. In order to get around this issue a mirrored mesh scheme is used. The coupled surfaces show the exact same discretization so that nodes on one surface can easily find their neighbor on the opposite surface. The connection information is then propagated through node position rather than tetrahedrons. In the case of exchange coupling, the magnetic moments only affect each other when they are direct interface neighbors. The interface exchange field exerted by the normalized magnetic moment $\mathbf{M}_2$ on its interface neighbor $\mathbf{M}_1$ can be computed from

(2.7) and (2.20) as:

$$\mathbf{H}_{iex,1} = \frac{J_c}{M_{s1} t_1} \mathbf{M}_2 \,, \tag{2.21}$$

where t_1 is the effective thickness of the node representing $\mathbf{M}_1$. This effective thickness can be computed as the effective volume of this node, defined as the sum of the volumes of all tetrahedrons containing it divided by 4, divided by the effective surface of the node, defined as the sum of all the surface triangles containing it divided by 3.

2.3.4 Magnetocrystalline anisotropy

The magnetocrystalline anistropy originates from the spin-orbit interactions related to the potentials due to the lattice structure. This leads to preferential directions for the orientation of the magnetization within the material. Orientations that are favored by the magnetocrystalline anisotropy are called easy axes. Those that are highly disfavored by this interaction are called hard axes. There are different types of anisotropy due to different lattice structures. The most important type for applications is the uniaxial anisotropy. In this case there exists a single easy axis corresponding to two antiparallel preferential directions for the orientation of the magnetic moments within the material. This essentially leads to the existence of two easily distinguishable stable states. This property is useful for data storage, where the detection of these states can correspond to reading a 1 or a 0, the elementary components of binary data.

The potential energy corresponding to the uniaxial anisotropy is written:

$$E_{K_u} = K_1 V \sin^2 \theta + K_2 V \sin^4 \theta \,, \tag{2.22}$$

where K_1 is the first order uniaxial anisotropy constant in CGS units of erg/cm^3, K_1 is the second order uniaxial anisotropy constant in erg/cm^3, V is the volume occupied by the considered magnetic moment in cm^3 and θ is the angle between the easy axis and the magnetic moment. The

energy is minimized when $\theta = 0$ or $\theta = \pi$, i.e. when the magnetization is oriented along the easy axis. The general expression of the total uniaxial anisotropy energy over a volume with uniform anisotropy axis $\mathbf{k}_u$ and magnetization $\mathbf{M}$ can be expressed as:

$$E_{K_u} = \int_\Omega K_1 \left(1 - (\mathbf{M}\cdot\mathbf{k}_u)^2\right) + K_2 \left(1 - (\mathbf{M}\cdot\mathbf{k}_u)^2\right)^2 dV\,. \tag{2.23}$$

The anisotropy field at one node can be computed from (2.7) and (2.23) as:

$$\mathbf{H}_K = \frac{2K_1}{M_s}(\mathbf{M}\cdot\mathbf{k}_u)\,\mathbf{k}_u + \frac{4K_2}{M_s}\left(1 - (\mathbf{M}\cdot\mathbf{k}_u)^2\right)(\mathbf{M}\cdot\mathbf{k}_u)\,\mathbf{k}_u\,. \tag{2.24}$$

The first term of the right-hand side of (2.24) represents the first-order uniaxial anisotropy. The second term of the right-hand side is the second-order uniaxial anisotropy. In many cases the influence of this second-order term is negligible and K_2 is set to 0, simplifying the expression of the anisotropy field.

The second common type of anisotropy is called cubic anisotropy. In this case there are three different easy axes $\mathbf{k}_{c1}$, $\mathbf{k}_{c2}$ and $\mathbf{k}_{c3}$ usually along the [100], [010] and [001] crystallographic directions and two energy density constants K_1 and K_2 in erg/cm^3. The potential energy density can be written:

$$E_{cubic} = K_1\left(M_1^2M_2^2 + M_1^2M_3^2 + M_2^2M_3^2\right) + K_2M_1^2M_2^2M_3^2\,, \tag{2.25}$$

where $M_i = \mathbf{M}\cdot\mathbf{k}_{ci}$.

The cubic anisotropy field at one node can be computed from (2.7) and (2.25) as:

$$\mathbf{H}_{K,cubic} = -\frac{1}{M_s}\begin{bmatrix} 2K_1M_1\left(M_2^2+M_3^2\right) + 2K_2M_1M_2^2M_3^2 \\ 2K_1M_2\left(M_1^2+M_3^2\right) + 2K_2M_1^2M_2M_3^2 \\ 2K_1M_3\left(M_1^2+M_2^2\right) + 2K_2M_1^2M_2^2M_3 \end{bmatrix}\,. \tag{2.26}$$

Unlike the demagnetizing field or the exchange field, the anisotropy field at one node does not

depend on the magnetization state at other nodes.

2.4 Domain walls

The competition between the interactions described in section 2.3 leads to a set of effects. One of the most notable ones is the appearance of domains in thin magnetic structures. At short range, magnetic spins tend to keep an aligned order due to the strong local influence of the exchange field. However, at long range the influence of the dipolar field becomes stronger and tend to orient the magnetic moment antiparallel to each other. The anisotropy field can be used to force the magnetization into one of two states determined by the easy axis. This combination generates areas where the magnetization is uniformly oriented towards one direction of the easy axis, surrounded with similar sized areas, where the magnetization is antiparallel. These are magnetic domains. The volume between domains where the magnetization is transitioning between one and the other direction of the easy axis is called a domain wall.

We can distinguish two main categories of domain walls, called Bloch and Néel domain walls (fig. 2.5). The difference between these domain walls is the axis about which the magnetization transitions from one to the other easy directions. Various factors determine which kind of domain wall is most favored. Among them, the Dzyaloshinskii-Moriya interaction, talked about in a later section, is known to cause the transition from Néel to Bloch wall as its influence increases [21]. In strips where the easy axis of the magnetization is in plane, the Bloch wall is favored when the track is wide whereas the Néel wall is favored when the track is narrower than the domain wall width[22]. More complex domain walls can exist, such as vortex domain walls in wide racetracks [23].

The characteristics of domain walls strongly depend on the material parameters, mainly its exchange and anisotropy energy densities. Indeed having a thick domain wall means the spins will carry more anisotropy energy, whereas a narrow domain wall will have neighboring spins

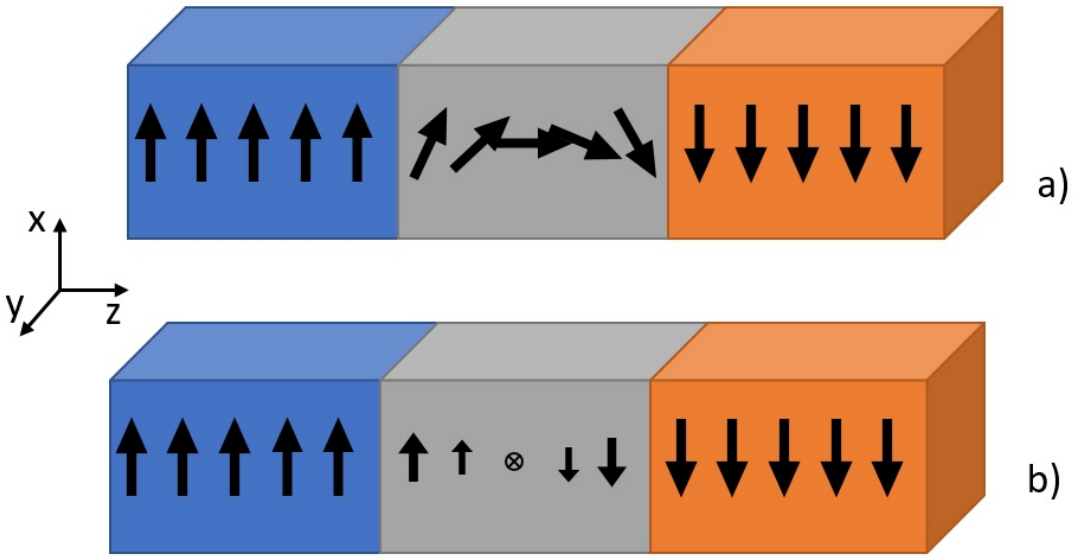

Figure 2.5: Domain walls in two magnetic tracks with perpendicular anisotropy along the x axis. Between the domains, the gray area corresponds to domain walls. a) Example of a Néel domain wall. The magnetization within the wall transitions between the two opposite directions of the easy axis by rotating about the y axis. b) Example of a Bloch domain wall. The magnetization within the wall transitions between the two opposite directions of the easy axis by rotating about the z axis.

with large differences in direction, carrying more exchange energy. In the typical case of a thin film with perpendicular uniaxial anisotropy energy density K and exchange constant A, the energy per unit surface of a domain wall is:

$$\sigma_{DW} = 4\sqrt{AK}\,. \tag{2.27}$$

Moreover the domain wall length can be expressed as:

$$\delta_{DW} = \sqrt{\frac{A}{K}} \tag{2.28}$$

Equation (2.28) shows that higher exchange constant leads to larger domain walls whereas higher anisotropy constant leads to narrower domain walls. Typically the domain wall width can range from a few atoms to hundreds of nanometers[24].

Domain walls are important topics of study and discussion because of their role in information storage. Classically, bits of data are stored on magnetic materials as magnetic domains with the magnetization pointing towards one or the other easy axis direction to represent a 1 or a 0. Domain walls are structures that need to be under control to make sure the data is not corrupted.

Some type of applications such as racetrack memory[25, 26] or domain wall logic [27, 28, 29] focus on manipulating domain walls for information storage or processing. Moving domain walls raises a few problems. Domain walls are very sensitive to the local variations in their environment; defects in materials can create areas where they can minimize their energy, thus making it hard to push them out of it. These areas are called pinning sites. Performance issues include occurrence of the Walker breakdown limit and the difficulty to tune the material parameters. Some of these aspects are described in more details in chapter 3.

2.5 Thermal effects

Real-world applications and magnetic devices typically have to work at room or chip temperature. The energy contained in the lattice under the form of thermal excitation introduces a certain amount of disorder that simulations have to take into account in order to be able to accurately evaluate the reliability of potential systems.

2.5.1 The Curie temperature

Magnetic order at the atomistic scale allows for mesoscopic or macroscopic magnetic moments to exist. When an external field (or anisotropy field) is applied to a magnetic system, the spins tend to align towards it in order to minimize their energy. However, thermal excitation induces a distribution of the magnetic moments around this energy minimum and that distribution increases with the temperature. This explains the fact that higher temperatures generate higher

magnetic disorder at the atomistic scale. When the magnetic disorder is high, the moments are oriented in random directions to some degree and compensating each other, reducing the total macroscopic moment. The temperature at which the material does not display a macroscopic spontaneous (i.e. under no applied field) magnetic moment is called the Curie temperature T_C. For $T < T_C$, we can write:

$$M \sim (T - T_C)^{\beta}\,, \tag{2.29}$$

where M is the spontaneous magnetization, T is the temperature and β is a parameter that depends on the type of considered material.

The magnetic susceptibility χ of a material represents the ease with which the magnetization of this material is affected by an external field $\mathbf{H}$. It is defined as:

$$\mathbf{M} = \chi \mathbf{H}\,. \tag{2.30}$$

The higher the temperature, the higher the magnetic disorder and the harder it is to compensate this disorder by an external field. As a result, the magnetic susceptibility for $T > T_C$ described by the Curie-Weiss law as:

$$\chi = \frac{C}{T - T_C}\,, \tag{2.31}$$

where C is the material-dependent Curie constant.

The Curie temperature imposes a restriction on the kind of material that can be used for data storage purposes. Indeed these applications require data that is stable at room temperature, so the considered materials must have a reasonably high Curie temperature to prevent their demagnetization.

2.5.2 The stochastic LLG equation

The LLG equation expressed in (2.1) is fully deterministic and the evolution of the magnetization computed by it only depends on the competition between the magnetic fields. This corresponds to simulating the behavior of a system at a temperature of 0K. For many devices this kind of modeling is not satisfying: some processes related to magnetization dynamics strongly depend on the thermal excitation of the spins such as the magnetization reversal in a magnetic dot.

To accurately represent the influence of temperature in our finite element model, it is necessary to adapt (2.1). For this reason, a stochastic thermal field $\mathbf{H}_{th}$ is added to the equation. Its purpose is to account for the random excitation that is affecting each spin. The thermal field takes the form of a Gaussian noise that takes a different random value at each node. Its amplitude has to be adapted to the time-step used by the solver. Indeed, the thermal effects originate from the heat transfer between phonons, magnons and electrons, which occurs at a much faster scale (femtoseconds to picoseconds) than magnetization dynamics. We can then understand that over a large time step, the influence of the thermal excitation on a single spin, kicking it into a random direction in relatively small intervals, tends to even out. This amplitude is calculated using the fluctuation-dissipation theorem [30]. The thermal field at each node can be expressed as[6]:

$$\mathbf{H}_{th} = \sqrt{\frac{2\alpha k_B T}{\gamma M_s (1+\alpha^2) V dt}}\mathbf{\Gamma}, \tag{2.32}$$

where $\mathbf{\Gamma}$ is a random Gaussian noise vector, α is the damping parameter, k_B is the Boltzmann constant, T is the temperature, γ is the gyromagnetic ratio, M_s is the saturation magnetization, V is the effective volume of the considered node and dt is the time step.

This field can be included in the LLG equation as:

$$\frac{d\mathbf{M}}{dt} = -\frac{\gamma}{1+\alpha^2}\mathbf{M}\times\left(\mathbf{H}_{eff}+\mathbf{H}_{th}\right) - \frac{\alpha\gamma}{1+\alpha^2}\mathbf{M}\times\mathbf{M}\times\left(\mathbf{H}_{eff}+\mathbf{H}_{th}\right). \tag{2.33}$$

Equation (2.33) can be used to simulate the behavior of systems at temperatures significantly lower than the Curie temperature. Closer to the Curie temperature, the reduction of the total spontaneous magnetization described in (2.29) becomes significant and the model is not able to accurately take this effect into account. Indeed, we are always assuming that the magnitudes of all magnetic moments are constant. Other options are available for this case. In finite-element simulations, the Landau-Lifshitz-Bloch (LLB) equation can be used instead of the LLG one [31]. The LLB equation allows the magnitude of the magnetic moments at each node to vary independently such that when $T = T_C$, $\|\mathbf{M}\| = 0$. The other option is to use an atomistic model [32, 33, 34]. In this case, each atom is simulated so the averaging of the magnetization and the Curie temperature emerge by themselves from the material parameters. In particular, the form of the exchange field used for atomistic simulations is the Heisenberg Hamiltonian described in (2.17) rather than the continuous exchange field (2.19) used in finite-elements modeling. The exchange constant J_{ex} and the lattice type carry all the informations needed to calculate the Curie temperature. Alternatively, the material properties can be parameterized.

2.5.3 Validating the implementation of thermal fields

When developing simulation softwares like FastMag, it is important to have a set of standard tests to be able to make sure the implementations of the different components is correct. Stochastic fields are a complex part to validate due to their random nature. In order to make sure thermal fields are working correctly, a probabilistic Boltzmann test can be performed. Let us consider a macrospin with anisotropy and thermal effects as the only fields affecting it. As described in (2.22), the energy of such a system can be written as:

$$E = -K_u V \left(\mathbf{M} \cdot \mathbf{k}\right)^2 , \tag{2.34}$$

where K_u is the magnetocrystalline anisotropy constant with an anisotropy axis $\mathbf{k}$, V is the

volume of the considered magnetic particle and **M** is the normalized magnetization vector of the macropsin. If we consider that the anisotropy axis is along z, we can rewrite (2.34) as:

$$E = -K_u V M_z^2 \,. \tag{2.35}$$

Under a given temperature T, the probability for the system to be in a state of a given energy E follows a Boltzmann distribution that can be written:

$$p(E) = C^{te} e^{\frac{-E}{k_B T}} \,, \tag{2.36}$$

where k_B is the Boltzmann constant.

Using (2.35), this gives:

$$p(E) = C^{te} e^{\frac{K_u V M_z^2}{k_B T}} \,. \tag{2.37}$$

From this result we can theoretically link the distribution of the z components of the magnetizations in an array of small particles to the temperature. A correctly computed thermal field should yield the same distribution for such an array.

In order to perform this test, a magnetic particle small enough to always have a uniform magnetization was created. This was a disk with a diameter of 5nm and a thickness of 1nm, with its flat surfaces normal to the y axis and with a uniaxial anisotropy axis along z. The mesh size was chosen to be 1nm. For different values of the anisotropy energy density K_u, 10000 simulations are launched in parallel, each of them only including thermal fields with a temperature of 300K and anisotropy. Dipolar fields are neglected. The system can evolve freely during 10ns during which the macrospin oscillates around the anisotropy axis (position of the energy minimum) due to thermal activation. After these 10ns, the z component of magnetization is recorded, then all results are compiled to draw the distribution (fig. 2.6).

The results shown are the linear regression of the distribution of M_z^2 after letting the dots

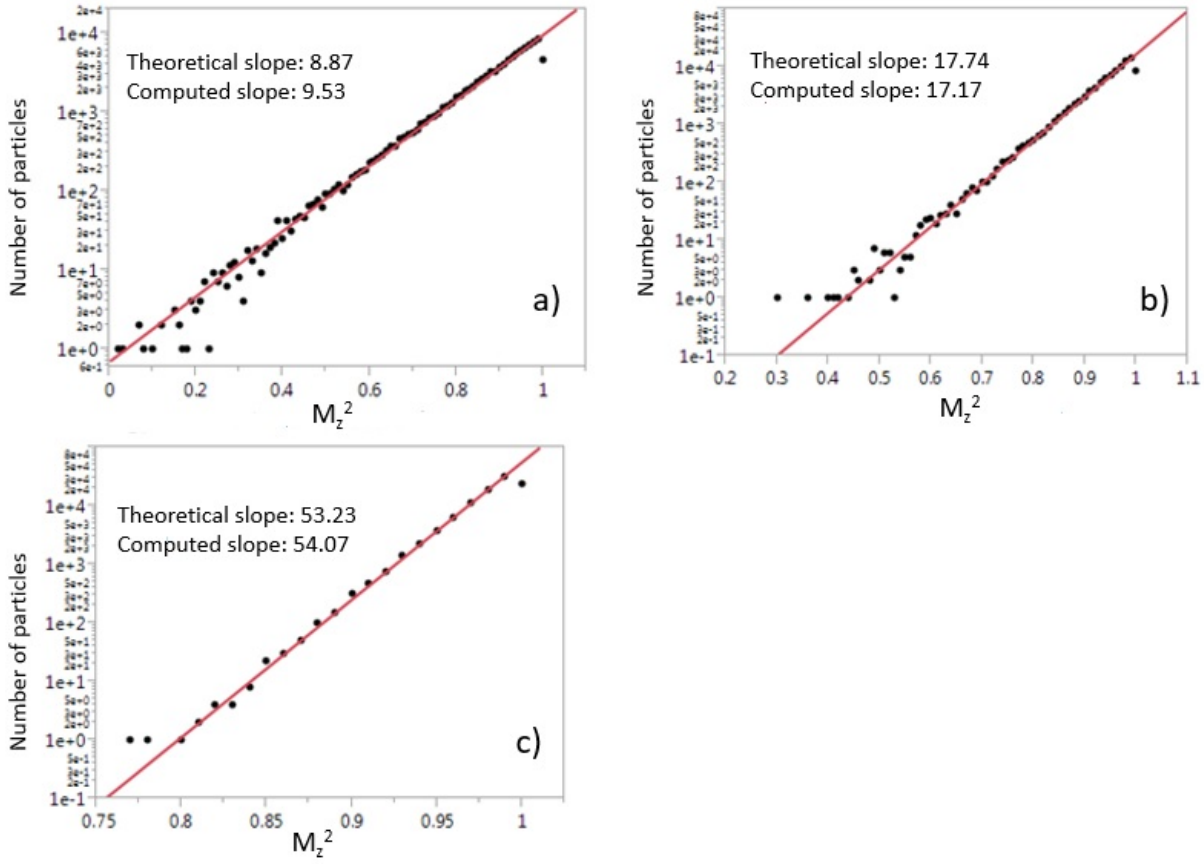

Figure 2.6: Distribution of M_z^2 to test thermal fields for different values of the anisotropy field $H_k = \frac{2K_u}{M_s}$. Each case represents the distribution of a sample of 10000 results. a) $H_k = 1$kOe. b) $H_k = 2$kOe. c) $H_k = 6$kOe.

evolve freely for 10ns. The slope of the logarithm of M_z^2 can be calculated analytically from (2.37) to be $\frac{K_u V}{k_B T}$. This predicted slope is compared to our results. In the three different cases considered, the slope obtained from the simulations is very close from what is predicted. We can conclude that thermal fields are correctly implemented in FastMag.

2.6 Nudged elastic band method

Switching dynamics and processes are one of the most studied topics in micromagnetics due to its importance in controlling device behavior. As a result, several methods have been developed to predict critical switching properties, such as minimum energy paths between two

states or energy barriers for thermal stability [35, 36, 37]. The nudged elastic band (NEB) method is a common method employed in micromagnetics to find the minimum energy path between two configuration states by starting from any path connecting these states in the configuration space, discretized into images [38, 39, 40, 41, 6]. This barrier gives direct insight into the thermal stability, because it corresponds to the minimum energy that has to be brought to the system in order for it to be modified, i. e. in magnetic recording, for the recorded bit to be erased. Indeed the time for which a system can expected to be stable at a given temperature is directly related to this energy barrier through the Néel-Arrhenius law as:

$$\tau = \tau_0 e^{\frac{\Delta E}{K_b T}}, \tag{2.38}$$

where τ_0 is the relaxation time, alternatively expressed as $\tau_0 = \frac{1}{f_0}$ where f_0 is the thermal attempt frequency in Hz, ΔE is the energy barrier, K_b is the Boltzmann constant and T is the temperature. For convenience the energy barrier is typically expressed in units of $K_b T$ and commercial-grade devices aim for a thermal stability of approximately $100 K_b T$.

In the nudged elastic band method, each image corresponds to a magnetization state $\mathbf{M}^k$. The initial images are usually calculated based on a time-domain calculation forcing the magnetization state from the initial to the final configuration, and selecting a few of them as the input for NEB. The path finding procedure corresponds to an energy gradient descent scheme done in parallel on each of these images, with the added constraint of images being unable to get close to one another. This translates to the following formula:

$$\frac{d\mathbf{M}^k}{d\xi} = -\left[\nabla E^k - \left(\nabla E^k \cdot \mathbf{t}^k\right)\mathbf{t}^k\right], \tag{2.39}$$

where ξ is an integration parameter, ∇E^k is the gradient in energy of image k with respect to $\mathbf{M}^k$ and $\mathbf{t}^k$ is a unit tangent vector to the path, defined as:

$$\mathbf{t}^k = \frac{\mathbf{M}^{k+1} - \mathbf{M}^{k-1}}{\left\|\mathbf{M}^{k+1} - \mathbf{M}^{k-1}\right\|}. \tag{2.40}$$

After waiting for convergence, the images of the final magnetization states correspond to the minimum energy path as shown in fig. 2.7.

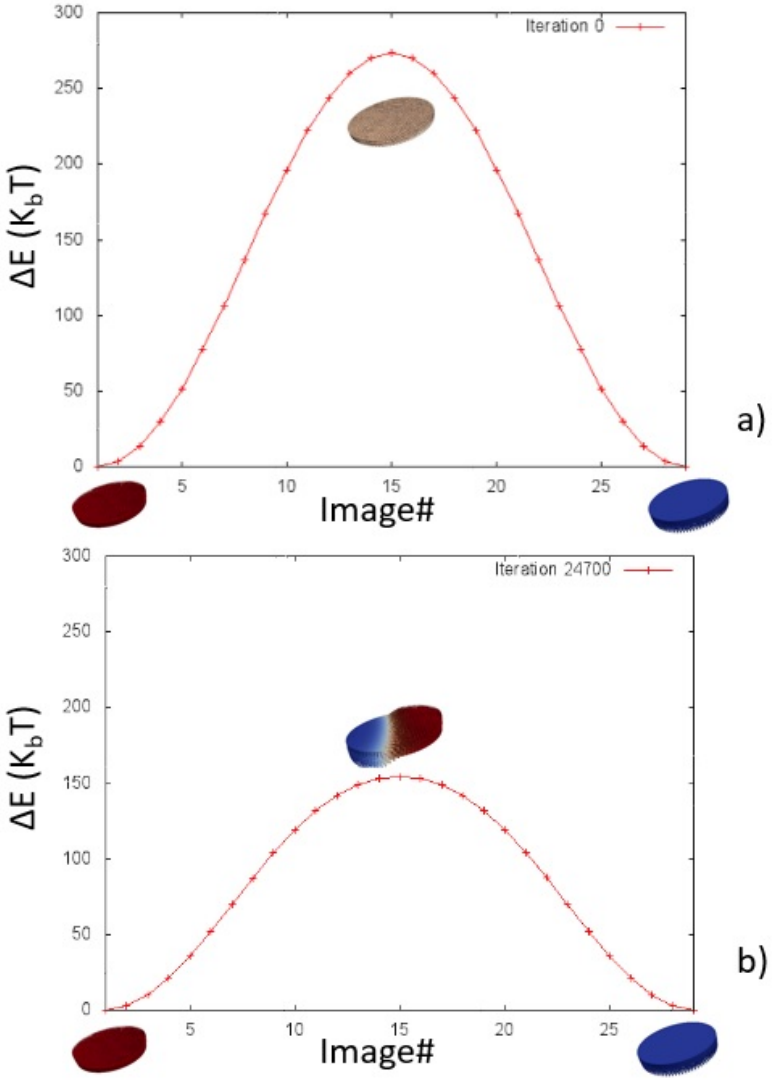

Figure 2.7: Energy of the different images along the reversal path of a single magnetic layer. a) The initial path is considered to be a uniform switching. The insets show the magnetic configurations of the first, middle and last images. b) After 24700 NEB iterations, the minimum energy path has been found. The energy barrier is almost twice as small as the one observed in case a. The inset shows that the maximum energy configuration is a domain wall. In this case, domain wall switching is more energy-efficient than uniform switching.

Chapter 3

Current-driven domain walls in antiferromagnetically coupled nanowires

3.1 Bulk spin-transfer torque

The interactions between electrical currents and magnetic materials take a large place in the conception of future magnetic-based memory technologies. They arise from the fact that spins of the electrons composing the flowing current interact with the atoms of the lattice by reciprocal transfer of their angular momenta. This effect is called spin-transfer torque. When an electron reaches the vicinity of an atomic moment, the momentum transfer from the atom to the electron is strong enough to polarize its spin along the direction of this moment. Reciprocally, the momentum of the atom is slightly moved towards the incident electron spin direction. When a sufficient number of electrons interact with the atom, its momentum eventually becomes fully aligned with the incident electron spin direction. This way the direction of the magnetization of two consecutive momenta along the current path can be transferred from the first one to the second one (fig. 3.1).

This effect is called bulk spin-transfer torque when it occurs inside continuous systems

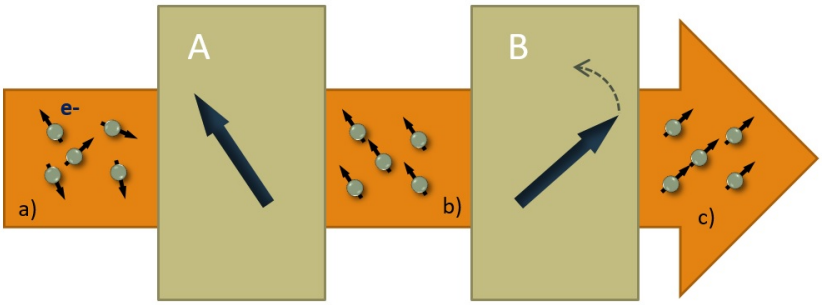

Figure 3.1: Electrons flowing through two magnetic layers A and B. a) Before entering any magnetic material the current is not polarized: electron spins have a random direction. b) Electrons become polarized by momentum transfer with the atoms of material A and their spin take the same direction. c) Reciprocal momentum transfer happens within layer B. Electrons become polarized towards the direction of the magnetization of material B, and the magnetic momenta within layer B are kicked towards the incident polarization direction.

within which the magnetization is not uniform. When electrons traverse such a system, they constantly change their spin direction in order to align with the local angular momenta of surrounding atoms. Reciprocally, these electrons continuously transfer the momentum that was previously acquired from atoms they interacted with earlier along their path. Bulk spin-transfer torque can be added to the LLG equation (2.1) by including torques terms as formulated by Zhang [42] and Thiaville [43]. Its expression then becomes:

$$\frac{d\mathbf{M}}{dt} = -\gamma\mathbf{M}\times\mathbf{H} + \alpha\mathbf{M}\times\frac{d\mathbf{M}}{dt} - (\mathbf{u}\cdot\nabla\mathbf{M}) + \beta\mathbf{M}\times(\mathbf{u}\cdot\nabla\mathbf{M}) \,, \tag{3.1}$$

where $\mathbf{u}$ is the domain wall mobility defined as $\mathbf{u} = \frac{g\hbar P}{4eM_s}\mathbf{J} = \frac{g\mu_B P}{2eM_s}\mathbf{J}$, where g is the Land factor of the electron, $\hbar$ is the reduced Plank constant, P is the current polarization, e is the electron charge, M_s is the saturation magnetization and $\mathbf{J}$ is the current density. The part of (3.1) corresponding to the bulk spin-transfer torque can be divided into two components. The first one is the term in $-(\mathbf{u}\cdot\nabla\mathbf{M})$. This term describes how the magnetic moment at any point of the material is affected by the transport processes incoming electrons whose conduction spin follows the local spatial magnetization variation. For this reason it is called the adiabatic torque [44, 45]. The second term,

in $\beta\mathbf{M} \times (\mathbf{u} \cdot \nabla\mathbf{M})$ accounts for the deviation of spin-transfer from the adiabatic condition. It is called non-adiabatic (or field-like) torque and is characterized by the non-adiabatic parameter β [46, 47, 48, 49]. The origin and nature of components from which it is originating is still unclear as well as its magnitude.

This property makes it seem like magnetic textures within the system are pushed by the electrical current. This leads to several possible applications such as domain-wall or skyrmion-based racetrack memory or logic devices.

3.2 Magnetic nanowires

Magnetic materials are most useful for information storage due to their ability to retain their state without the need to sustain power (non-volatility). Hard drives are the most successful example of magnetic memory but development is ongoing on future candidates for faster and more efficient technologies.

Manipulating magnetic domain walls (DW) to store and transfer information is envisioned to enable high-density, low-power, non-volatile, and non-mechanical memory, recording and processing systems. Related concepts have been explored in the past, e.g. bubble memory [50], and are promising for future systems, e.g. racetrack memory[25] where DWs can be moved by applied magnetic fields[51] and/or by currents[52] via the spin transfer torque (STT) effects[53, 54] (fig. 3.2. STT arises from the transfer of angular momentum from spin-polarized electrons to the DW magnetic moments and provides particularly attractive opportunities for DW manipulation[55].

However, there are several obstacles to be overcome to enable these technologies. One obstacle is the Walker breakdown limit[56, 43], which imposes a maximum velocity on the domain wall motion at low field or current in magnetic systems posing a major problem in terms of the information transfer and storage speed. The domain wall dynamics in a single-layer

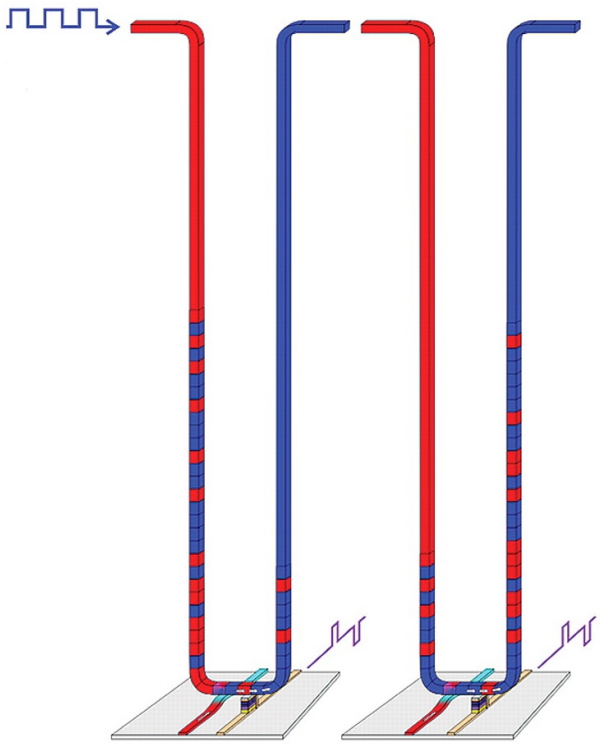

Figure 3.2: Racetrack memory as introduced by S. S. P. Parkin[25]. This type of memory consists in an array of magnetic nanowires where bits are represented by domains (blue and red areas) within which the magnetization points towards the same direction. These domains can be pushed through the wire using spin-transfer torque until they reach a reading or writing point.

nanowire can fall into different regimes depending on the relative values of the parameters. In the absence of current, if the magnitude of the external magnetic field is below the Walker threshold, the wall moves at a constant velocity that increases linearly with field. If the applied field is stronger than this threshold field, there is precession, intervals of backward motion and overall slowdown of the domain wall propagation (fig 3.3 and fig 3.4). When only current is applied, the dynamics depend on the relative values of the damping parameter α and the non-adiabatic spin-transfer parameter β . If $\beta = \alpha$ the DW motion is steady for any DC applied current. If $\beta > \alpha$, the domain wall motion is steady for currents smaller than a certain limit, but slows down for stronger currents due to the onset of precession and backward motion. If $\beta < \alpha$, there is a range of low currents for which the spins of the domain wall tilt out of plane, after which the DW is stationary, i.e., no motion. For yet stronger currents, the domain wall propagates during which

its magnetization undergoes precession. All these limits correspond to the Walker threshold that depends on α, the saturation magnetization M_s, and the geometry of the domain wall.

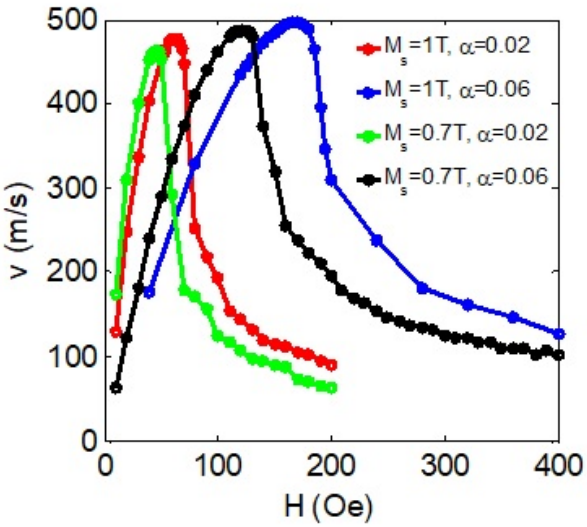

Figure 3.3: Micromagnetic simulation of the velocity of a domain wall within a single nanowire as a function of applied field for different values of the saturation magnetization M_S and damping parameter α. For low fields, the domain wall speed increases up to a certain point. After this critical point, a sharp decrease in domain wall velocity is observed. This critical point is called the Walker breakdown limit.

The Walker breakdown limit originates from the demagnetization field that imparts to the magnetization a torque, which takes the opposite direction once the applied field and/or current exceed a certain critical value. Below these critical field or current values the domain wall velocity increases with increasing field or current, whereas above this critical value the domain wall motion exhibits back and forth oscillations . If the Walker breakdown effect could be eliminated then the increased DW speed would allow a major improvement in terms of data rates. Approaches have been presented for reducing or eliminating the Walker breakdown, such as those based on complex topologies or alternative physical effects[57, 58, 59, 50], or the use of transverse magnetic fields[60]. However, these approaches may be hard to implement in practical systems.

In this work, we present numerical simulations and an analytical model of antiferromag-

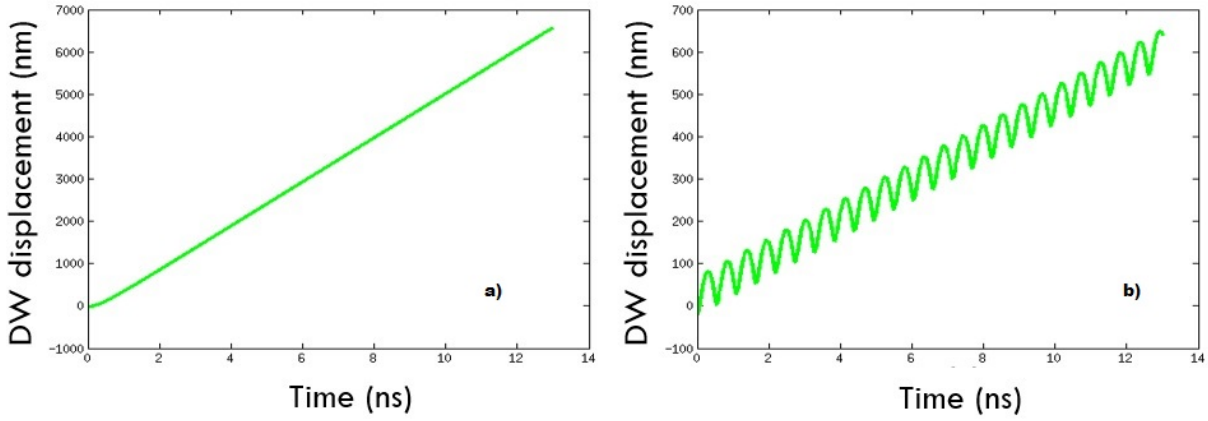

Figure 3.4: a) Micromagnetic simulation of the position of a domain wall within a nanowire as a function of time for a field lower than the Walker breakdown critical field. The velocity of the domain wall is constant. b) Micromagnetic simulation of the position of a domain wall within the same nanowire as a) as a function of time for a field higher than the Walker breakdown limit. The domain wall is moving back and forth along the wire and its overall speed is lower than case a).

netically coupled (AFC) nanowires subject to applied fields and currents. In an AFC nanowire system the symmetry of the problem is altered through interlayer exchange fields, which allow compensation of torque terms that lead to the domain wall instability. The AFC nanowire geometry significantly reduces the Walker breakdown effects and even eliminates Walker breakdown when current is used to move the domain walls via the STT effect. This results in a dramatic increase of the domain wall velocities in a simple geometry that is practically feasible using different materials such as in-plane anisotropy CoFeB/Ru/CoFeB or Fe/Cr/Fe structures or out-of-plane [Co/Ni]/Ru/[Co/Ni] structures. For field-driven domain wall motion the maximum domain wall velocities and corresponding applied fields can be much higher than those of single-layer nanowires. For STT induced domain wall motion the Walker breakdown can not only be reduced but also eliminated. Importantly, this structure can be readily realized experimentally and enhanced domain wall velocities have been reported for AFC films with perpendicular anisotropy[61].

3.3 Bulk spin-transfer torque in micromagnetics

The proposed antiferromagnetically coupled nanowire structure is studied by micromagnetic simulations using FastMag. This requires the spin-transfer torque within the bulk of the magnetic material to be accurately represented and added to the Landau-Lifshitz-Gilbert equation as described in (3.1). Effects induced by currents have to be implemented as additional torques as they do not originate from potential energies. This section explains how the computation of the bulk spin-transfer torque is done within FastMag.

3.3.1 Computing the current density

One of the main input parameters of the LLG equations with bulk STT terms (3.1) is the current density. A model used for micromagnetic simulations can have an arbitrary shape in which case the current density is probably not constant over the whole structure. Instead of choosing to input a constant current density, the software computes it based on a set of inputs including: two boundary surfaces where a high and low potential are applied and an average current density. Once the input potential at the boundaries is known, we can calculate the potential at each internal node of the mesh by applying Poisson's equation which states:

$$\begin{cases} \nabla(\sigma\nabla\Phi) = 0 & \text{for internal nodes} \\ \nabla\Phi\cdot\mathbf{n} = 0 & \text{at boundary if potential is not defined} \\ \Phi = \Phi_0 & \text{at boundary if potential is defined} \end{cases}, \tag{3.2}$$

where Φ is the potential, Φ_0 is the input surface potential, σ is the conductivity and $\mathbf{n}$ is a vector normal to the surface. This equation can be solved using an iterative linear solver such as GMRES[62, 63] with a precomputed Laplacian matrix. This way the electric potential on each node of the model can be computed even for arbitrary shapes and structures. Once this potential is known, the non-uniform current density can be calculated at node *i* by:

$$\mathbf{J}_i = \sigma_i \mathbf{E}_i = -\sigma_i \nabla \Phi_i \,, \tag{3.3}$$

where $\mathbf{E}_i$ is the electric field at node i.

When the current density is known at each point, the average current density can be calculated and rescaled by multiplying the current density value at each node by a constant to fit the user's input.

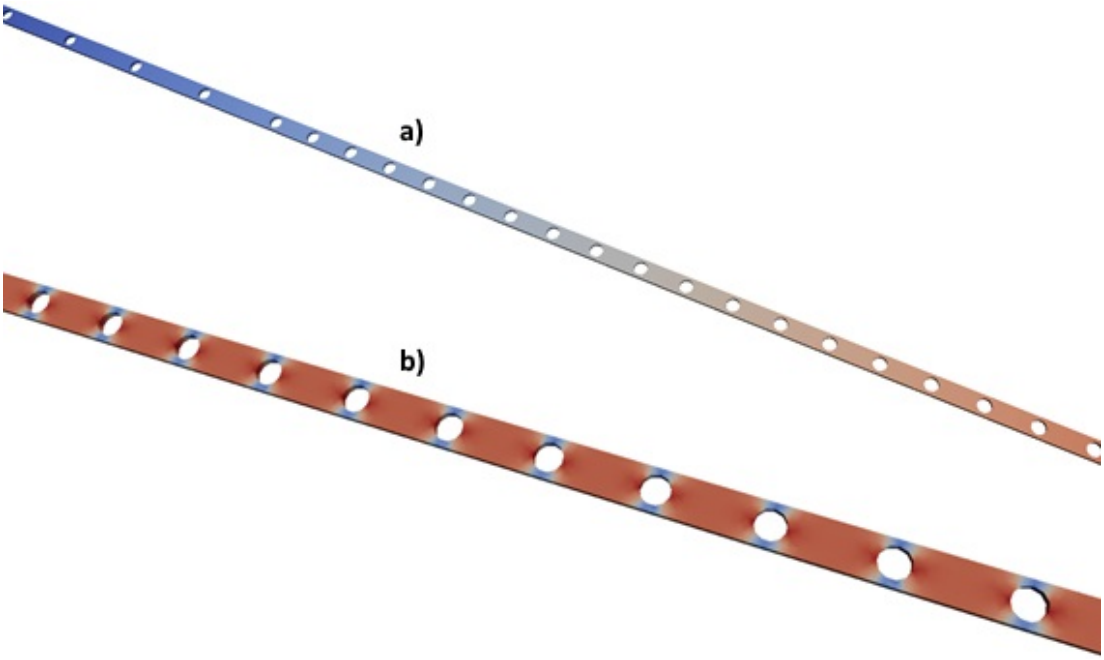

Figure 3.5: a) Electric potential as calculated at each node within a complex structure (nanowire with holes) when the input potential is applied at both extremities of the model. The blue color corresponds to high potential, red to low potential. b) Current density as computed within the nanowire with holes when electrons are flowing from one end to the other. Red corresponds to low current density, blue corresponds to high current density. The current density is higher around the holes because the electrons have to travel through a smaller cross-section.

3.3.2 Implementing the bulk spin-transfer torques

As described in (3.1) the bulk spin-transfer torque is added to the LLG equation under the form of two terms: the adiabatic and the non-adiabatic torques. To implement these torques into

our simulation software we need to make this equation explicit, i.e. we need to get rid of the $\frac{d\mathbf{M}}{dt}$ term on the right-hand side. This is possible by replacing the right-hand side occurrence of $\frac{d\mathbf{M}}{dt}$ by the whole right-hand side itself, which gives:

$$\begin{aligned}\frac{d\mathbf{M}}{dt} = &-\gamma\mathbf{M}\times\mathbf{H}+\alpha\mathbf{M}\times\left(-\gamma\mathbf{M}\times\mathbf{H}+\alpha\mathbf{M}\times\frac{d\mathbf{M}}{dt}-(\mathbf{u}\cdot\nabla\mathbf{M})+\beta\mathbf{M}\times(\mathbf{u}\cdot\nabla\mathbf{M})\right)\\ &-(\mathbf{u}\cdot\nabla\mathbf{M})+\beta\mathbf{M}\times(\mathbf{u}\cdot\nabla\mathbf{M})\,.\end{aligned} \tag{3.4}$$

We know that $\mathbf{M}$ and $\frac{d\mathbf{M}}{dt}$ are perpendicular so we can use the identity:

$$\mathbf{M}\times\mathbf{M}\times\frac{d\mathbf{M}}{dt} = -\frac{d\mathbf{M}}{dt} \tag{3.5}$$

to simplify (3.4) into:

$$\begin{aligned}\left(1+\alpha^2\right)\frac{d\mathbf{M}}{dt} = &-\gamma\mathbf{M}\times\mathbf{H}-\alpha\gamma\mathbf{M}\times\mathbf{M}\times\mathbf{H}-(\mathbf{u}\cdot\nabla\mathbf{M})-\alpha\mathbf{M}\times(\mathbf{u}\cdot\nabla\mathbf{M})\\ &+\beta\mathbf{M}\times(\mathbf{u}\cdot\nabla\mathbf{M})+\alpha\beta\mathbf{M}\times\mathbf{M}\times(\mathbf{u}\cdot\nabla\mathbf{M})\,.\end{aligned} \tag{3.6}$$

In this explicit expression, the bulk STT terms have a new form. We can define an effective non-adiabatic field:

$$\mathbf{H}_{non-adiab} = \frac{\beta}{\gamma}(\mathbf{u}\cdot\nabla\mathbf{M})\,, \tag{3.7}$$

and write (3.6) as:

$$\begin{aligned}\left(1+\alpha^2\right)\frac{d\mathbf{M}}{dt} = &-\gamma\mathbf{M}\times(\mathbf{H}+\mathbf{H}_{non-adiab})-\alpha\gamma\mathbf{M}\times\mathbf{M}\times(\mathbf{H}+\mathbf{H}_{non-adiab})\\ &-(\mathbf{u}\cdot\nabla\mathbf{M})-\alpha\mathbf{M}\times(\mathbf{u}\cdot\nabla\mathbf{M})\,.\end{aligned} \tag{3.8}$$

Including the non-adiabatic term inside the effective field makes for an easier and cleaner code. This property reinforces the analogy between the non-adiabatic spin-transfer torque and an effective field and validates its other appellation: field-like torque.

The main term in both $\mathbf{H}_{non-adiab}$ and the adiabatic torque is $(\mathbf{u}\cdot\nabla\mathbf{M})$. To reduce the computational weight of this part, the gradient matrix can be precomputed based on the mesh information. If we consider that the current density is relatively constant within the system (i.e. it varies with time by the same factor at every node in the model), we can precompute $\mathbf{u}\cdot\nabla$. This way $\mathbf{M}$ is the only varying factor and we are left with a straightforward matrix multiplication at each time step.

3.4 Micromagnetic modeling

The proposed structure is made of two antiferromagnetic (AFC) magnetic layers. The specific model used is made of two soft magnetic nanowires antiferromagnetically coupled through their common interface. The antiferromagnetic coupling between the nanowires is sufficiently strong such that a single domain wall across both nanowires is present. The wire width is chosen relatively small, compatible with the wire sizes envisioned in memory applications. In this case the domain wall structure is a transverse wall in each layer, with opposite directions. We are studying the propagation of such a domain wall within this structure.

The presented simulation results were obtained by solving the LLG equation using both FastMag[64] and OOMMF[65] simulators, which gave nearly identical results. These simulators respectively use finite element method (FEM) and finite differences method and provide a variety of tools that can be used to study domain wall motion. For each simulation the transverse domain wall was located inside the nanowire and its position was monitored. The domain wall speed in the numerical simulations was obtained by calculating the time for the domain wall to propagate over a fixed distance (chosen as 10 micron). We studied the evolution of the domain wall velocity as a

function of the applied field in single-layer and AFC nanowires for different values of saturation magnetization, damping and exchange fields. For the AFC nanowire case, each nanowire had a 4-nm thickness and a 20-nm width. The single-layer nanowire had a 4-nm thickness and 20-nm width. The cell size was 2 nm. The ferromagnetic exchange constant was chosen to be 1.3×10^{-6} erg/cm. In these cases, the values for the damping, non-adiabatic STT parameter and thicknesses of both wires are identical to facilitate comparisons with single wire simulations. However the results can be easily extended to systems where the two layer have different parameters and the conclusions are similar.

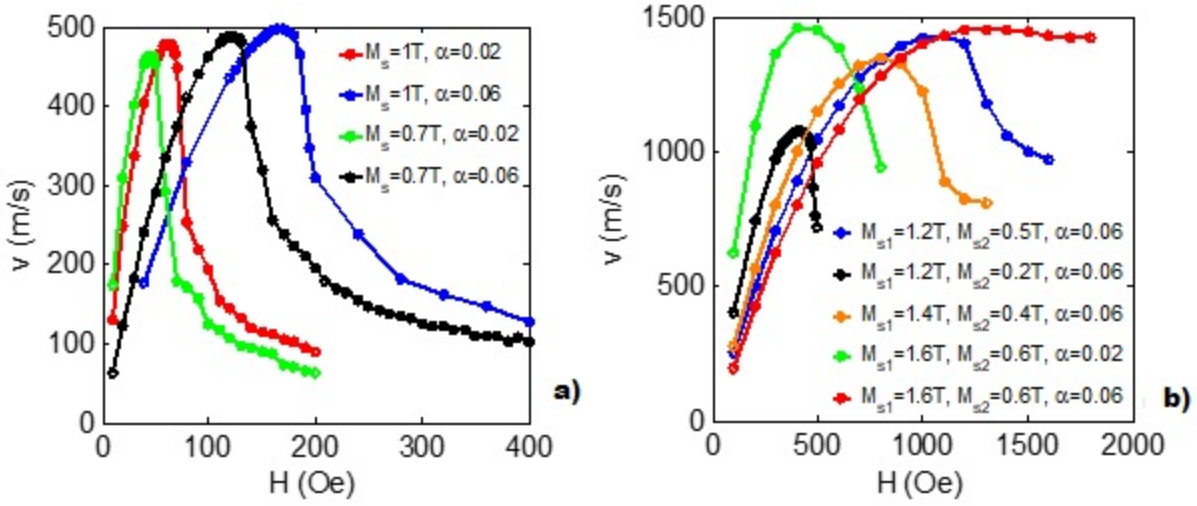

Figure 3.6: Average domain velocities (v) driven for applied magnetic field (H) obtained via FEM micromagnetic simulations. a) single-layer nanowire with different values of the damping and saturation magnetization; b) antiferromagnetically coupled nanowire with different values of the damping and saturation magnetization with exchange energy density of 10^{-3} J/m2.

Figures 3.6 a and b show the domain wall velocity versus the applied field for single-layer and AFC nanowires, respectively. The results are given for different damping constants and saturation magnetization values. The magnetocrystalline anisotropy was kept to zero in both models, hence the anisotropy was entirely due to magnetostatics (shape anisotropy). However, this approach is also applicable to perpendicular anisotropy systems. For a single-layer nanowire, changing the saturation magnetization and damping only affects the domain wall mobility and

the Walker breakdown critical field, but not the maximum achievable domain wall velocity in the system, as seen from Fig. 3.6a. This limitation clearly does not hold for AFC NW (Fig. 3.6b), where the mobility, Walker breakdown critical field, and peak velocity can be modulated through the saturation magnetization and damping of the constituent layers (Fig. 3.6b). Indeed, even when the total saturation magnetization of the composite system $|M_{s1} - M_{s2}|$ is identical to the saturation magnetization of the single-layer nanowire, the domain wall motion characteristics are different. The interaction between the two antiferromagnetically coupled layers and the symmetry of the system under the applied field must be taken into account to explain this phenomenon.

Several observations from Fig. 3.6b can be made. First, the closer the saturation magnetizations M_{s1} and M_{s2} are to each other the greater the peak velocity. However, in the pre-Walker breakdown regime, the smaller the net magnetization the slower the domain wall motion for a given magnetic field. The mobility, defined as the rate of change of domain wall velocity with the applied field $\frac{dv}{dH}$, is, therefore, proportional to the net magnetization of the AFC nanowire. If the saturation magnetization is equal in both layers, there is no motion under an applied field.

The operation of the AFC nanowire can be understood by considering the compensation of torques in the antiferromagnetically-coupled system, which is mediated through antiferromagnetic interlayer exchange. Indeed, in the strong coupling limit, the directions of the precessional Zeeman torques in each layer are opposite, resulting in a weaker total precessional Zeeman torque $\mathbf{\Gamma}_H^{AFC} \propto M_{s1} - M_{s2}$ acting on the rigid AFC domain wall. The way this dependency is established will be described in the next section explaining the analytical calculations. This torque is responsible for the out of plane tilting of the spins, which eventually triggers the Walker breakdown for strong enough applied fields. On the other hand, the direction of the precessional demagnetization and damping torques in each layer complement each other, $\mathbf{\Gamma}_{demag}^{AFC} \propto M_{s1}^2 + M_{s2}^2$ and $\mathbf{\Gamma}_{damping}^{AFC} \propto M_{s1} + M_{s2}$, resulting in a strong torque preventing the Walker breakdown. As a consequence, the Walker breakdown occurs for much greater fields and far greater domain wall velocities. We note that these modified torque expressions come from the strong coupling assumption, and reflect

that the interlayer exchange interaction mediates the dynamical response. A disadvantage to field driven operation, however, is that increases in peak velocities are accompanied with a reduced domain wall mobility. The situation is different when the domain wall is driven by current. The difference is due to the fact that the symmetry changes and the characteristics describing motion for the same parameter sets are significantly different.

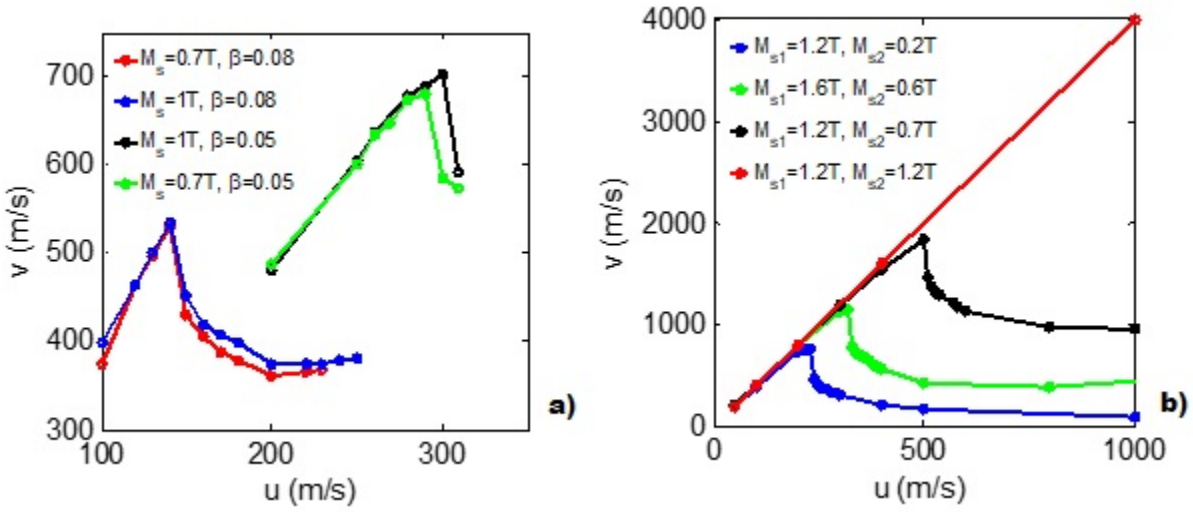

Figure 3.7: Domain wall velocity (v) as a function of u obtained via FEM micromagnetic simulations. (a) single-layer nanowire with different values of the non-adiabatic parameter β and saturation magnetization with $\alpha = 0.02$; (b) AFC NW with different values of the saturation magnetization with exchange energy density of 10^{-3} J/m2, $\alpha = 0.02$ and $\beta = 0.08$.

Figure 3.7b shows the velocity of a domain wall in AFC nanowires for different values of the applied current, the non-adiabatic parameter β , M_{s1} and M_{s2}. In AFC nanowire simulations, u corresponds to an effective domain wall mobility defined as $u = \frac{gJ\mu_B P}{2eM_{s,ave}}$ where $M_{s,ave} = \frac{M_{s1}+M_{s2}}{2}$. In the case of $M_{s1} = M_{s2}$ the Walker breakdown is not encountered for any value of current amplitude for the AFC nanowire. The torques responsible for triggering the Walker breakdown fully compensate each other. This will be detailed in the next section. For both field and current bias, the simulations indicate that the peak velocities and the Walker breakdown threshold are higher for an AFC nanowire than for single-layer nanowire. In both cases, the outcome is due to the compensation of different torque terms on account of system symmetry under given bias,

which is mediated though the interlayer exchange interaction.

3.5 Analytical formulation

To gain a better understanding of the behavior of the domain wall in antiferromagnetically coupled nanowires, we developed an analytical formulation of this problem. The motion of the DW is due to the torques applied on the magnetic moment. By calculating all these torques, it is possible to find the DW velocity and the Walker breakdown limit. This method has been described in detail for a conventional single-phase NW by A. Mougin et al [66]. The Walker breakdown condition for a single wire can be expressed as:

$$\left| H_{ext} + (\beta - \alpha) \frac{u}{\gamma \Delta} \right| > 2\pi\alpha M_s \left(N_y - N_x \right) , \tag{3.9}$$

where H_{ext} is the external field, β is the non-adiabatic parameter, α is the damping term, u is the domain wall mobility,γ is the gyromagnetic ratio, Δ is the domain wall length, M_s is the saturation magnetization and N_x and N_y are the demagnetization factors along the x and y directions.

The domain wall velocity under the Walker breakdown limit within a single wire is written:

$$\upsilon_{single} = \frac{\Delta\gamma}{\alpha} H_{ext} + \frac{\beta}{\alpha} u . \tag{3.10}$$

It is equally applicable to systems with in-plane and out-of-plane magnetic anisotropies. A similar process is used to calculate these values in the AFC nanowire case.

3.5.1 Problem definition

We consider two superposed and antiferromagnetically coupled nanowires infinitely long along the z direction. The nanowires are thin along the x and y direction and we can assume that

the magnetization is uniform along those axis. We focus on a domain wall within such a structure as shown in fig. 3.8a), propagating along the z direction. We assume that the antiferromagnetic coupling between the nanowires is infinite, thus the magnetic moments at a similar z coordinate in each wire are always perfectly opposite.

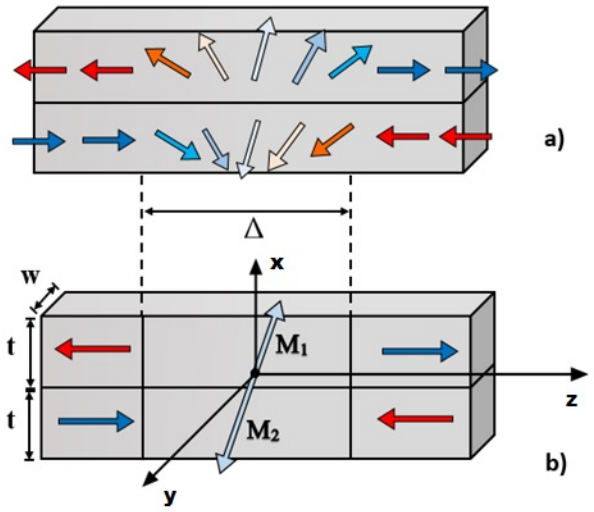

Figure 3.8: Schematic of a DW in an AFC NW. (a) The DW represented by a continuous variation of the magnetization states; (b) Representation in the analytical model in which the DW in each layer is represented by a single macrospin with its width w, thickness t and length Δ.

The profile of the magnetization along the domain wall in the top nanowire is given by[67]:

$$\theta_1(z) = 2\arctan(e^{\frac{z-z_0}{\Delta}}), \tag{3.11}$$

where $\theta(z)$ is the angle of the magnetic moment at coordinate z with respect to the z axis and z_0 is the position of the center of the domain wall where $\theta(z) = \frac{\pi}{2}$. Δ is the width of the domain wall, given by:

$$\Delta = \sqrt{\frac{A}{K_u + 2\pi M_{s,eff}^2 (N_x \cos(\phi(t))^2 + N_y \sin(\phi(t))^2 - N_z)}}, \tag{3.12}$$

where A is the exchange constant, K_u is the magnetocrystalline anisotropy constant, $M_{s,eff}$ is the effective saturation magnetization, ϕ is the angle of the magnetzation with respect to the x axis and N_x, N_y and N_z are the demagnetization factors of the volume containing the domain wall[68].

The magnetization in the bottom wire is always opposite so we have:

$$\theta_2(z) = \theta_1(z) + \pi = 2\arctan(e^{\frac{z-z_0}{\Delta}}) + \pi. \tag{3.13}$$

Moreover it ensues from (3.11) and (3.13) that:

$$\frac{d\theta_1}{dz}(z) = \frac{d\theta_2}{dz}(z) = 2\frac{e^{\frac{z-z_0}{\Delta}}}{\Delta(1+(e^{\frac{z-z_0}{\Delta}})^2)}. \tag{3.14}$$

Using the trivial identity:

$$\sin(2\arctan(x)) = \frac{2x}{x^2+1}, \tag{3.15}$$

and combining (3.11), (3.13) and (3.14) we find that:

$$\frac{d}{dz}\theta_1 = \frac{d}{dz}\theta_2 = \frac{\sin(\theta)}{\Delta}. \tag{3.16}$$

This identity will be useful for this work. Knowing the internal profile of the domain wall, we can now consider it as two opposite macrospins $\mathbf{M}_1$ and $\mathbf{M}_2$ fixed at the same origin (the center of the domain wall) as shown in fig. 3.8b). Given the fact that θ_2 can be expressed as a function of θ_1, we will now write:

$$\begin{cases} \theta = \theta_1 = \theta_2 + \pi \\ \phi = \phi_1 = \phi_2 + \pi \end{cases}, \tag{3.17}$$

We can now express $\mathbf{M_1}$ and $\mathbf{M_2}$ as:

$$\mathbf{M}_1 = M_{s1}\begin{bmatrix}\sin(\theta)\cos(\phi)\\ \sin(\theta)\sin(\phi)\\ \cos(\theta)\end{bmatrix};\mathbf{M}_2 = -M_{s2}\begin{bmatrix}\sin(\theta)\cos(\phi)\\ \sin(\theta)\sin(\phi)\\ \cos(\theta)\end{bmatrix}. \tag{3.18}$$

3.5.2 Angular momentum conservation

The behavior of the domain wall can be derived from the angular momentum conservation theorem applied on $\mathbf{M}_1$ and $\mathbf{M}_2$. Indeed, we have that:

$$\frac{d}{dt}\mathbf{L}_{total}(t) = \mathbf{\Gamma}_{total}(t), \tag{3.19}$$

where $\mathbf{\Gamma}_{total}$ is the sum of all torques applied on the system and

$$\mathbf{L}_{total} = \mathbf{L}_1 + \mathbf{L}_2 = -\frac{\mathbf{M}_1}{\gamma} - \frac{\mathbf{M}_2}{\gamma}, \tag{3.20}$$

with γ being the gyromagnetic ratio.

Combining (3.19) with (3.20) gives:

$$\frac{d}{dt}(\mathbf{M}_1 + \mathbf{M}_2) = -\gamma\mathbf{\Gamma}_{total}. \tag{3.21}$$

The left-hand side of (3.21) can be calculated from (3.18):

$$\frac{d}{dt}(\mathbf{M}_1 + \mathbf{M}_2) = (M_{s1} - M_{s2})\begin{bmatrix}\cos(\theta)\dot{\theta}\cos(\phi) - \sin(\theta)\sin(\phi)\dot{\phi}\\ \cos(\theta)\dot{\theta}\sin(\phi) + \sin(\theta)\cos(\phi)\dot{\phi}\\ -\sin(\theta)\dot{\theta}\end{bmatrix}. \tag{3.22}$$

For convenience, we convert this matrix to spherical coordinates system using the transfer matrix

from x, y, z to r, θ, ϕ that follows:

$$M_{transfer} = \begin{bmatrix} \sin(\theta)\cos(\phi) & \sin(\theta)\sin(\phi) & \cos(\theta) \\ \cos(\theta)\cos(\phi) & \cos(\theta)\sin(\phi) & -\sin(\theta) \\ -\sin(\theta) & \cos(\phi) & 0 \end{bmatrix}. \tag{3.23}$$

Equation (3.22) written in spherical coordinates becomes:

$$\frac{d}{dt}(\mathbf{M}_1 + \mathbf{M}_2)_{(r,\theta,\phi)} = (M_{s1} - M_{s2}) \begin{bmatrix} 0 \\ \dot{\theta} \\ \sin(\theta)\dot{\phi} \end{bmatrix}_{(r,\theta,\phi)}. \tag{3.24}$$

From there, we can get the two main equations of motion with respect to the components of $\mathbf{\Gamma}_{total}$ in spherical coordinates by incorporating this result back into (3.21):

$$\dot{\theta} = -\frac{\gamma}{M_{s1} - M_{s2}} \Gamma_{total,\theta}; \tag{3.25}$$

$$\dot{\phi} = -\frac{\gamma}{M_{s1} - M_{s2}} \Gamma_{total,\phi}. \tag{3.26}$$

3.5.3 Contributions to the total torque

We now need to find all the contributions to the total torque $\mathbf{\Gamma}_{total}$. These include the typical magnetic fields used in macrospin models: the external field $\mathbf{H}_{ext}$ and the self demagnetizing field $\mathbf{H}_{demag}$. The two spins representing each sublayer being always perfectly opposite, the dipolar field they generate on each other is 0. When considering the torques we also need to take into account the damping torque and eventually the spin transfer torque.

Torque generated by the external field

We consider the external field applied along z to push the domain wall. The torque generated by the external field on the top macrospin $\mathbf{M}_1$ can be computed in cartesian coordinates by:

$$\mathbf{\Gamma}_{ext,1} = \mathbf{M}_1 \times \mathbf{H}_{ext} = M_{s1} H_{ext} \sin\theta \begin{bmatrix} \sin\phi \\ -\cos\phi \\ 0 \end{bmatrix} . \tag{3.27}$$

Similarly, the torque applied on the bottom macrospin $\mathbf{M}_2$ is written:

$$\mathbf{\Gamma}_{ext,2} = \mathbf{M}_2 \times \mathbf{H}_{ext} = M_{s2} H_{ext} \sin\theta \begin{bmatrix} -\sin\phi \\ \cos\phi \\ 0 \end{bmatrix} . \tag{3.28}$$

We can write the total external torque applied on the $\{\mathbf{M}_1, \mathbf{M}_2\}$ system in spherical coordinates by summing (3.27) and (3.28) and applying the transfer matrix (3.23):

$$\mathbf{\Gamma}_{ext,(r,\theta,\phi)} = \begin{bmatrix} 0 \\ 0 \\ -H_{ext} \sin\theta (M_{s1} - M_{s2}) \end{bmatrix} . \tag{3.29}$$

It appears that the torque due to the external field depends on $M_{s1} - M_{s2}$ and becomes 0 when $M_{s1} = M_{s2}$. This is to be expected. Indeed, in this case the AFC nanowire has a fully compensated total saturation magnetization and becomes unaffected by any external field.

Torque generated by the demagnetizing field

The volume of magnetic material represented by the macrospin is a rectangular bar, which has some self-demagnetizing properties depending on its aspect ratio [68]. The demagnetizing

factors corresponding to the x, y and z directions are noted N_x, N_y and N_z. In the model we are considering, the top and bottom wires have the same aspect ratio so they share the same demagnetizing factors. As a first approximation, increasing the thickness of a layer is roughly equivalent to increasing M_s. This method can be used to create asymmetrical AFC wires using the same material for each wire like the previously described CoFeB/Ru/CoFeB structure. We can then write the expression for the demagnetizing field applied on the top macrospin as:

$$\mathbf{H}_{demag,1} = -4\pi M_{s1} \begin{bmatrix} N_x \sin\theta\cos\phi \\ N_y \sin\theta\sin\phi \\ N_z \cos\theta \end{bmatrix}, \tag{3.30}$$

and similarly for the bottom macrospin:

$$\mathbf{H}_{demag,2} = 4\pi M_{s2} \begin{bmatrix} N_x \sin\theta\cos\phi \\ N_y \sin\theta\sin\phi \\ N_z \cos\theta \end{bmatrix}. \tag{3.31}$$

Thus the torques applied on the top and bottom macrospin are:

$$\mathbf{\Gamma}_{demag,1} = \mathbf{M}_1 \times \mathbf{H}_{demag,1} = 4\pi M_{s1}^2 \begin{bmatrix} \sin\phi\cos\theta\sin\theta(N_y - N_z) \\ -\cos\theta\cos\phi\sin\theta(N_x - N_z) \\ \sin\phi\cos\phi\sin^2\theta(N_x - N_y) \end{bmatrix}; \tag{3.32}$$

$$\mathbf{\Gamma}_{demag,2} = \mathbf{M}_2 \times \mathbf{H}_{demag,2} = 4\pi M_{s2}^2 \begin{bmatrix} \sin\phi\cos\theta\sin\theta(N_y - N_z) \\ -\cos\theta\cos\phi\sin\theta(N_x - N_z) \\ \sin\phi\cos\phi\sin^2\theta(N_x - N_y) \end{bmatrix}. \tag{3.33}$$

We can write the total demagnetizing torque applied on the $\{\mathbf{M}_1, \mathbf{M}_2\}$ system in spherical coordinates by summing (3.32) and (3.33) and applying the transfer matrix (3.23):

$$\mathbf{\Gamma}_{demag,(r,\theta,\phi)} = -4\pi(M_{s1}^2 + M_{s2}^2) \begin{bmatrix} 0 \\ \cos\phi\sin\phi\sin\theta(N_x - N_y) \\ \cos\theta\sin\theta(\cos^2\phi(N_x - N_y) + N_y - N_z) \end{bmatrix}. \tag{3.34}$$

We notice that the torque due to the demagnetizing field depends on $M_{s1}^2 + M_{s2}^2$, which is not the same as the dependence observed for the external field torque. Indeed, this time the demagnetizing interactions are not compensating each other, but adding to each other. This is only valid in the case where $\mathbf{M}_1$ and $\mathbf{M}_2$ are always perfectly opposite to each other, i.e. the antiferromagnetic coupling is very strong. This discrepancy between the way the different fields depend on M_{s1} and M_{s2} is one major difference between the AFC and single wire cases. In the single wire case, all the torques depend on M_s.

Damping torque

Our system includes energy loss that has to be represented under the form of a torque. The damping parameters in the wires can be different, they will be noted α_1 and α_2. According the the LLG equation (2.1), the damping torque applied on the top macrospin can be expressed as:

$$\mathbf{\Gamma}_{damping,1} = -\frac{\alpha_1}{\gamma M_{s1}}\mathbf{M}_1 \times \frac{d\mathbf{M}_1}{dt} = \frac{\alpha_1 M_{s1}}{\gamma} \begin{bmatrix} \dot{\phi}\cos\theta\cos\phi\sin\theta + \dot{\theta}\sin\phi \\ \dot{\phi}\cos\theta\sin\phi\sin\theta - \dot{\theta}\cos\phi \\ -\dot{\phi}\sin^2\theta \end{bmatrix}. \tag{3.35}$$

Similarly the damping torque applied on the bottom macrospin is:

$$\mathbf{\Gamma}_{damping,2} = -\frac{\alpha_2}{\gamma M_{s2}}\mathbf{M}_2 \times \frac{d\mathbf{M}_2}{dt} = \frac{\alpha_2 M_{s2}}{\gamma}\begin{bmatrix} \dot{\phi}\cos\theta\cos\phi\sin\theta + \dot{\theta}\sin\phi \\ \dot{\phi}\cos\theta\sin\phi\sin\theta - \dot{\theta}\cos\phi \\ -\dot{\phi}\sin^2\theta \end{bmatrix}. \tag{3.36}$$

Once again we can get the total torque in spherical coordinates by summing (3.35) and (3.36) and applying the transfer matrix (3.23):

$$\mathbf{\Gamma}_{damping,(r,\theta,\phi)} = \frac{M_{s1}\alpha_1 + M_{s2}\alpha_2}{\gamma}\begin{bmatrix} 0 \\ \dot{\phi}\sin\theta \\ -\dot{\theta} \end{bmatrix}. \tag{3.37}$$

The dependence on $\alpha_1 M_{s1} + \alpha_2 M_{s2}$ of the damping torque is different from the ones calculated for the external field torque and for the demagnetizing torque, which shows that contrarily to the single wire case, each torque will vary very differently when M_{s1} or M_{s2} is modified.

Spin transfer torque

In this part we write the domain wall mobility u_i of sublayer i as[69]:

$$u_i = \frac{gJ_e\mu_B P}{2eM_{si}}, \tag{3.38}$$

where J_e is the electrical current density, g is the Land factor, μ_B is the Bohr magneton, e is the electron charge and P is the polarization factor.

The spin transfer torque can be divided in two parts: the adiabatic and non-adiabatic torques. Using (3.16), the adiabatic torques in the top and bottom sublayers can be written as[43]:

$$\mathbf{\Gamma}_{adiab,1} = \frac{u_i}{\gamma}\frac{\partial}{\partial\theta}\mathbf{M}_1\frac{\partial}{\partial z}\theta = \frac{gJ_e\mu_B P}{2e\gamma}\frac{\sin\theta}{\Delta}\mathbf{e}_\theta; \tag{3.39}$$

$$\mathbf{\Gamma}_{adiab,2} = \frac{u_i}{\gamma}\frac{\partial}{\partial\theta_2}\mathbf{M}_2\frac{\partial}{\partial z}\theta_2 = -\frac{gJ_e\mu_B P}{2e\gamma}\frac{\sin\theta}{\Delta}\mathbf{e}_\theta\,. \tag{3.40}$$

These torques are compensating each other, leading to:

$$\mathbf{\Gamma}_{adiab,(r,\theta,\phi)} = \mathbf{\Gamma}_{adiab,1} + \mathbf{\Gamma}_{adiab,2} = 0\,. \tag{3.41}$$

The adiabatic torques of the two sublayers are compensating each other. This is one of the main differences when comparing the single wire case and the AFC case: the adiabatic torque plays no role in the latter. This peculiar property will have a major effect on the behavior of the domain wall when driven by a current. Indeed the adiabatic torque is related to the way the magnetic moments are precessing about the direction of the incoming electron spins which is one of the factors to take into account when considering the triggering of the Walker breakdown causing the slowdown of the DW propagation.

The non-adiabatic torques are written as:

$$\mathbf{\Gamma}_{non-adiab,1} = -\frac{\beta_1 u_1}{\gamma M_{s1}}\mathbf{M}_1\times\left(\frac{\partial}{\partial z}\mathbf{M}_1\right) = -\frac{\beta_1 gJ_e\mu_B P}{2e\gamma M_{s1}^2}\mathbf{M}_1\times\left(\frac{\partial}{\partial z}\mathbf{M}_1\right); \tag{3.42}$$

$$\mathbf{\Gamma}_{non-adiab,2} = -\frac{\beta_2 u_2}{\gamma M_{s2}}\mathbf{M}_2\times\left(\frac{\partial}{\partial z}\mathbf{M}_2\right) = -\frac{\beta_2 gJ_e\mu_B P}{2e\gamma M_{s2}^2}\mathbf{M}_2\times\left(\frac{\partial}{\partial z}\mathbf{M}_2\right). \tag{3.43}$$

Considering the fact that $\mathbf{M}_2 = -\frac{M_{s2}}{M_{s1}}\mathbf{M}_1$, we can rewrite (3.43) as:

$$\mathbf{\Gamma}_{non-adiab,2} = \frac{\beta_2 gJ_e\mu_B P}{2e\gamma M_{s1}^2}\mathbf{M}_1\times\left(\frac{\partial}{\partial z}\mathbf{M}_1\right). \tag{3.44}$$

which can be simplified into:

$$\mathbf{\Gamma}_{non-adiab,2} = \frac{\beta_2}{\beta_1}\mathbf{\Gamma}_{non-adiab,1}\,. \tag{3.45}$$

Then we can write the total non-adiabatic torque acting on the $\{\mathbf{M}_1, \mathbf{M}_2\}$ system as:

$$\mathbf{\Gamma}_{non-adiab,(r,\theta,\phi)} = \mathbf{\Gamma}_{non-adiab,1} + \mathbf{\Gamma}_{non-adiab,2} = \left(1 + \frac{\beta_2}{\beta_1}\right) \mathbf{\Gamma}_{non-adiab,1}\,, \tag{3.46}$$

which is equivalent to:

$$\mathbf{\Gamma}_{non-adiab,(r,\theta,\phi)} = -\left(\frac{\beta_1 + \beta_2}{2}\right) \frac{g J_e \mu_B P \sin\theta}{e\gamma\Delta} \mathbf{e}_\phi\,. \tag{3.47}$$

Contrarily to the adiabatic torque for which the components of the top and bottom nanowires are compensating each other, the components of the non-adiabatic torque act such that an effective non-adiabatic parameter $\beta_{eff} = \frac{\beta_1+\beta_2}{2}$ appears and the system behaves with respect to this torque in the same way a single nanowire with parameter β_{eff} would. This asymmetry between the behavior of the adiabatic and non-adiabatic torques is essential in differentiating the behavior of current-driven domain walls in single wires and AFC wires.

Total torques

Now that we established the formulas corresponding to each contributing torque, we need to express the θ and ϕ components of $\mathbf{\Gamma}_{total}$. From (3.29), (3.34), (3.37) and (3.47) we get:

$$\Gamma_{total,\theta} = -4\pi \sin\theta \cos\phi \sin\phi \left(M_{s1}^2 + M_{s2}^2\right)(N_x - N_y) + \frac{(M_{s1}\alpha_1 + M_{s2}\alpha_2)\,\dot{\phi}\sin\theta}{\gamma}\,; \tag{3.48}$$

$$\begin{aligned}\Gamma_{total,\phi} = {} & -4\pi \cos\theta \sin\theta \left(M_{s1}^2 + M_{s2}^2\right)\left(N_x \cos^2\phi - N_y \cos^2\phi + N_y - N_z\right) \\ & - H_{ext} \sin\theta\,(M_{s1} - M_{s2}) + \frac{(M_{s1}\alpha_1 + M_{s2}\alpha_2)\,\dot{\theta}}{\gamma} \\ & - \left(\frac{\beta_1 + \beta_2}{2}\right) \frac{g J_e \mu_B P \sin\theta}{e\gamma\Delta}\,.\end{aligned} \tag{3.49}$$

We can now plug these expressions into (3.25) and (3.26) to complete the equations describing the dynamics of the domain wall.

3.5.4 Solving the equations of motion of the AFC domain wall

Walker breakdown limit

We are interested in calculating the Walker breakdown limit of the AFC domain wall. We know that up to this limit the speed of the domain wall increases linearly with the applied current. Moreover, below the Walker breakdown limit, the domain wall motion is uniform and steady, meaning that the profile of the wall doesn't change as it progresses through the nanowire and its speed is constant. We are going to use this property, which is the same as setting:

$$\frac{d\phi}{dt} = 0\,. \tag{3.50}$$

According to (3.47), this means:

$$\Gamma_{total,\phi} = 0\,. \tag{3.51}$$

We define the speed as the domain wall as the speed of its center. Focusing on the center of the domain wall is the same as setting:

$$\theta = \frac{\pi}{2}\,. \tag{3.52}$$

This greatly simplifies (3.49) as $\sin\theta = 1$ and $\cos\theta = 0$ at the center of the domain wall. In the end, the criterion we are looking for can be extracted by combining (3.51) and (3.49) into:

$$-H_{ext}\left(M_{s1}-M_{s2}\right)-\frac{M_{s1}\alpha_1+M_{s2}\alpha_2}{M_{s1}-M_{s2}}\left(2\sin\left(2\phi\right)\pi\left(M_{s1}^2+M_{s2}^2\right)\left(N_x-N_y\right)\right) - \frac{\beta_{eff}gJ_e\mu_B P}{e\gamma\Delta}=0\,. \tag{3.53}$$

This equation can be rewritten by isolating the term that depends on ϕ, giving:

$$\sin\left(2\phi\right)=\frac{H_{ext}\left(M_{s1}-M_{s2}\right)+\frac{\beta_{eff}gJ_e\mu_B P}{e\gamma\Delta}}{2\pi\left(M_{s1}\alpha_1+M_{s2}\alpha_2\right)\frac{M_{s1}^2+M_{s2}^2}{M_{s1}-M_{s2}}\left(N_y-N_x\right)}\,. \tag{3.54}$$

This equation has to be true if $\frac{d\phi}{dt}=0$ so it must be true for the domain wall to have a steady displacement behavior within the nanowire. (3.54) can be true only if $|\sin 2\phi|\leq 1$, otherwise we know that steady progression of the domain wall is impossible, i.e. the Walker breakdown regime has been triggered. The Walker breakdown regime condition has been found: it happens when the absolute value of the right-hand side of (3.54) becomes greater than 1, which is equivalent to setting:

$$\left|H_{ext}\left(M_{s1}-M_{s2}\right)+\frac{\beta_{eff}gJ_e\mu_B P}{e\gamma\Delta}\right|>\left|2\pi\left(\alpha_1 M_{s1}+\alpha_2 M_{s2}\right)\frac{M_{s1}^2+M_{s2}^2}{M_{s1}-M_{s2}}\left(N_y-N_x\right)\right|\,. \tag{3.55}$$

The left-hand side of (3.55) has two components respectively corresponding the applied field an current. The right-hand side only depends on material parameters and aspect ratio. This equation determines what is the maximum combination of applied field and current that can be applied to the $\{\mathbf{M}_1,\mathbf{M}_2\}$ system before triggering the Walker breakdown.

Equation (3.55) is a general equation that works for any combination of fields, currents and damping parameters but we can simplify it by distinguishing a few particular cases. For example, if we consider only applied field or only applied current, we can get clear expressions for the corresponding Walker breakdown limits. The critical field to trigger the Walker breakdown

in an AFC nanowire when no current is applied can be expressed as:

$$|H_{c,WB}| = \left| 2\pi \left(\alpha_1 M_{s1} + \alpha_2 M_{s2}\right) \frac{M_{s1}^2 + M_{s2}^2}{\left(M_{s1} - M_{s2}\right)^2} \left(N_y - N_x\right) \right| . \tag{3.56}$$

We can notice that $\lim_{M_{s1} \to M_{s2}} H_{c,WB} = +\infty$, meaning that a fully compensated AFC nanowire could lead to the suppression of the Walker breakdown limit. However, doing so would also make the effective saturation magnetization of the nanowire 0, thus making it insensitive to external fields. In such a case, it would be impossible to drive the domain wall with an applied field. It also seems that wires with large saturation magnetization have higher Walker breakdown limits, but the efficiency of the domain wall transport must also take into account the velocity of the domain wall, which will be studied in the next subsection.

If we consider the case where only current is applied, we can find the critical current density that triggers the Walker breakdown from (3.55) as:

$$|J_{c,WB}| = \left| \frac{2\pi e \gamma \Delta}{\beta_{eff} g \mu_B P} \left(\alpha_1 M_{s1} + \alpha_2 M_{s2}\right) \frac{M_{s1}^2 + M_{s2}^2}{M_{s1} - M_{s2}} \left(N_y - N_x\right) \right| . \tag{3.57}$$

Similarly to the case where only applied field is applied, we find that $\lim_{M_{s1} \to M_{s2}} H_{c,WB} = +\infty$. However, the difference is that nothing prevents the spin-transfer torque from pushing the domain wall even though the magnetization is fully compensated. It seems then that this case would allow for complete suppression of the Walker breakdown, as suggested by the micromagnetic simulations. This result can be a great asset to speed up the data transmission speed in future devices.

The last case we can consider is the case where $\alpha_1 = \alpha_2 = \alpha$. This case is interesting because it makes an effective domain wall mobility appear. Indeed, we can write:

$$u_{eff} = \frac{g J_e \mu_B P}{2 e M_{s,ave}} , \tag{3.58}$$

with $M_{s,ave} = \frac{M_{s1} + M_{s2}}{2}$ to simplify (3.55) into:

$$\left| H_{ext}\frac{M_{s1}-M_{s2}}{M_{s1}+M_{s2}}+\frac{\beta_{eff}u_{eff}}{\gamma\Delta}\right| > \left|2\pi\alpha\frac{M_{s1}^2+M_{s2}^2}{M_{s1}-M_{s2}}\left(N_y-N_x\right)\right|. \tag{3.59}$$

Interestingly, when $\alpha_1 = \alpha_2$, we find that part of the left-hand side that expresses the applied current $\frac{\beta_{eff}u_{eff}}{\gamma\Delta}$ has the same form as in the single wire case[66], only using the effective values of the non-adiabatic parameter and domain wall mobility instead, that are based on average of the values of the two sublayers.

Now that we have expressions for the Walker breakdown limit of AFC nanowires with applied field and applied current, we can determine what is the velocity of the domain wall below this limit, and thus getting the maximum speed of the domain wall in this regime, which will be attained just before the critical point.

Domain wall velocity below the Walker breakdown

To calculate the speed of the domain wall below the Walker breakdown limit, we still take into account the steady motion condition described in (3.51). This condition turns (3.49) into an equation on $\frac{d\theta}{dt}$ that can be written as:

$$\begin{aligned}-\frac{\left(M_{s1}\alpha_1+M_{s2}\alpha_2\right)}{\gamma}\dot{\theta} = &-4\pi\cos\theta\sin\theta\left(M_{s1}^2+M_{s2}^2\right)\left(N_x\cos^2\phi-N_y\cos^2\phi+N_y-N_z\right)\\ &-H_{ext}\sin\theta\left(M_{s1}-M_{s2}\right)-\left(\frac{\beta_1+\beta_2}{2}\right)\frac{gJ_e\mu_B P\sin\theta}{e\gamma\Delta}.\end{aligned} \tag{3.60}$$

Once again we are interested in the behavior of the center of the domain wall so we set $\theta = \frac{\pi}{2}$. Moreover we can deduce from (3.16) that:

$$\upsilon = -\frac{\Delta}{\sin\theta}\dot{\theta}, \tag{3.61}$$

so the equation giving the velocity of the domain wall as a function of the applied field, applied

current and material parameters becomes:

$$\upsilon = \gamma\Delta\left(H_{ext}\frac{M_{s1}-M_{s2}}{\alpha_1 M_{s1}+\alpha_2 M_{s2}}+\frac{\beta_{eff}gJ_e\mu_B P}{e\gamma\Delta\left(\alpha_1 M_{s1}+\alpha_2 M_{s2}\right)}\right). \tag{3.62}$$

The right-hand side is composed of two parts: one describing how the velocity of the domain wall depends on the external field and the other how it depends on the applied current. If no current is applied, the velocity of the domain wall under applied field is:

$$\upsilon_{field} = \gamma\Delta H_{ext}\frac{M_{s1}-M_{s2}}{\alpha_1 M_{s1}+\alpha_2 M_{s2}}. \tag{3.63}$$

As expected, we can see that $\lim_{M_{s1}\to M_{s2}}\upsilon_{field} = 0$. This is due to the fact that as M_{s1} becomes close to M_{s2} the total saturation magnetization of the nanowire tends to 0, making the system insensitive to external fields. (3.56) showed that the critical Walker breakdown field could be pushed to infinity by compensating the saturation magnetizations of the two sublayers, but (3.63) shows that this purpose is cancelled by the fact that the wire can not be pushed by an applied field in such a system. AFC nanowires don't show any significant advantage compared to single nanowires when it comes to field-driven domain walls.

If no external field is applied, we can write the velocity of the domain wall below the Walker breakdown limit as:

$$\upsilon_{current} = \frac{\beta_{eff}gJ_e\mu_B P}{e\left(\alpha_1 M_{s1}+\alpha_2 M_{s2}\right)}. \tag{3.64}$$

Contrarily to the behavior observed for field-driven domain walls, the velocity of current-driven domain walls does not become 0 when the total saturation magnetization of the AFC nanowire becomes 0, i.e. when $M_{s1} = M_{s2}$. Moreover we can draw further analogy with the single wire system if we study the case where $\alpha_1 = \alpha_2 = \alpha$. Then, using the effective domain wall mobility as defined in the equation can be simplified as (3.58):

$$\upsilon_{current,\alpha_1=\alpha_2} = \alpha\frac{\beta_{eff}}{u_{eff}}, \tag{3.65}$$

which is the same form as what is obtained for the single wire, only replacing the non-adiabatic parameter β and the domain wall mobility u by their effective values over the AFC system. It means that the velocity of the domain wall below the Walker breakdown shows the same dependence on the applied current in the AFC and single wire cases so only the value of the Walker breakdown critical current appears to be modified.

This fact illustrates the importance of the result obtained in (3.57). Indeed, we showed that the Walker breakdown critical current could be suppressed for fully compensated AFC nanowires, and now we prove that the velocity of the domain wall is not impaired in this case. These taken together lead to the conclusion that AFC systems are of major importance in order to control and accelerate domain wall motion in nanowires because of its ability to entirely suppress the Walker breakdown limit, allowing for high velocity at low current densities. This analytical study confirms what could be inferred from the micromagnetic simulations and gives greater insight into how to tune M_{s1} and M_{s2} to reach expected performances. This result could be extended to other structures as well, such as skyrmions which are given increasing interest as candidates to propagate information through magnetic nanowires.

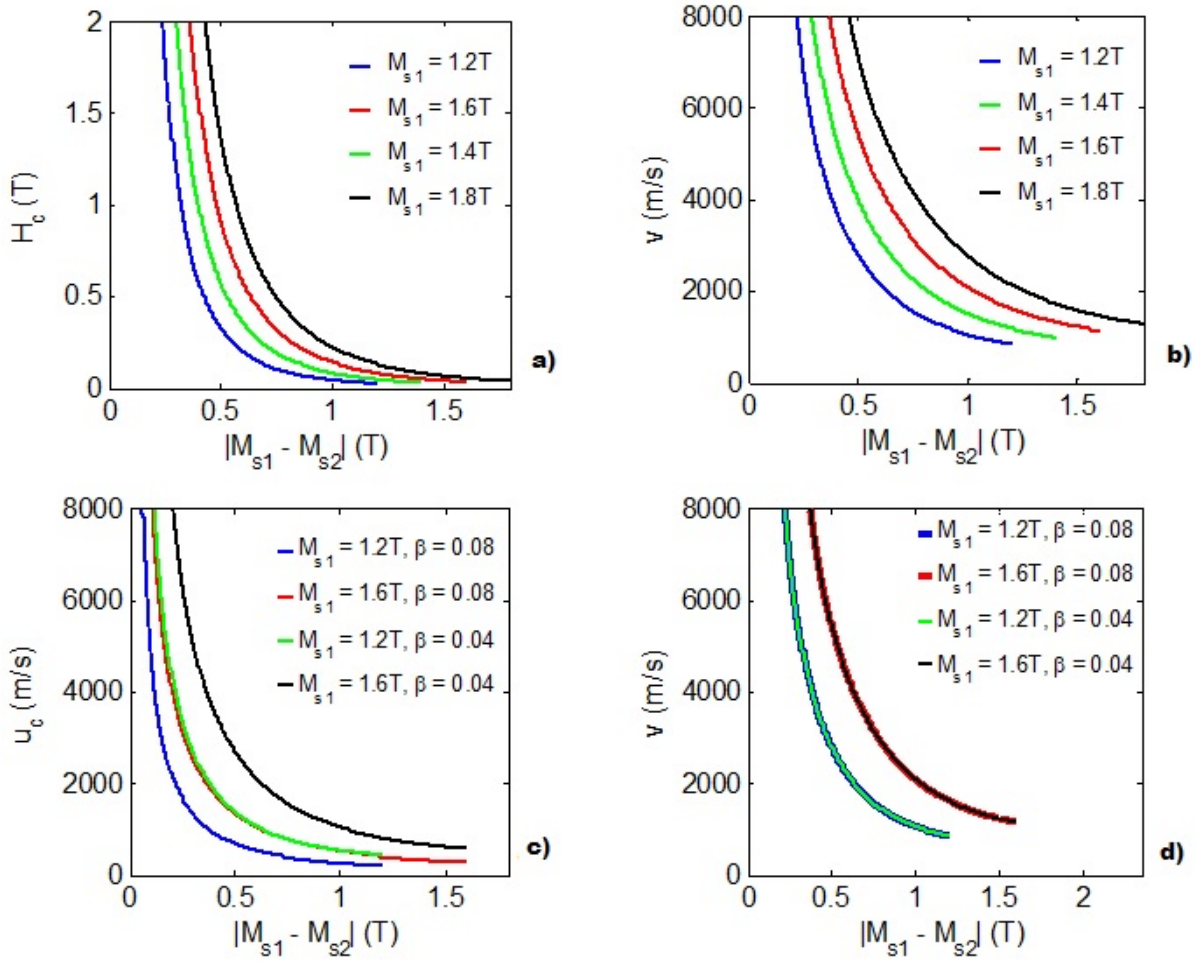

Figure 3.9: a) Analytical prediction for the Walker breakdown critical field in AFC nanowires as a function of the difference in saturation magnetization between the sublayers. Four different values of M_{s1} are chosen and M_{s2} varies continuously. b) Analytical computation of the maximum domain wall speed corresponding to parameters used in graph a). c) Analytical prediction for the Walker breakdown critical current in AFC nanowires as a function of the difference in saturation magnetization between the sublayers. Two different values of the non-adiabatic parameter β and Two different values of M_{s1} are chosen and M_{s2} varies continuously. d) Analytical computation of the maximum domain wall speed corresponding to parameters used in graph c). In all these cases, it is assumed that $\alpha_1 = \alpha_2$ and $\beta_1 = \beta_2$.

3.6 Conclusion

We have shown that the maximum achievable domain velocity in AFC nanowires under field or current bias can far exceed velocities attainable using single-layer nanowire systems. This result is not a consequence of a reduced average moment of the AFC-nanowire. We attributed this effect to the particular symmetry of the described system under a given bias, and the consequent compensation of torque terms that are responsible for structural instability. The expressions of these torque terms reflect the fact that interlayer exchange mediates domain wall dynamics in AFC nanowires. It was demonstrated that the Walker breakdown field could be significantly deferred by choosing saturation magnetizations of the two layers to be comparable. The characteristics of domain wall motion under field and current bias were demonstrated using micromagnetic simulations and further justified by an analytical model which predicts the Walker breakdown field, peak velocity under field and current bias, and wall mobility in AFC systems. It was shown that it is possible to suppress the Walker breakdown limit for current-driven domain wall motion without affecting its mobility by using similar or identical values of the saturation magnetization in both layers of the AFC nanowire. This can be done for any value of the damping parameter α or the non-adiabatic spin-transfer torque β.

It is expected that such results could translate well towards structures other than domain walls. In particular, propagation of skyrmions [70, 71] in antiferromagnetically coupled nanowires could take advantage of this effect to reach increased performance.

Aknowledgement: this chapter is a more detailed version of the work presented in a journal article [1] written in collaboration with M. V. Lubarda, S. Fu, R. Chang, M. A. Escobar, S. Mangin, E. E. Fullerton and V. Lomakin.

Chapter 4

Composite magnetic free layers under an applied current

4.1 Interface spin transfer torque

Spin valves are a common type of structure encountered in micromagnetics [72, 73]. They are the basic component of systems like magnetosresistive random access memory devices (MRAM). They consist in two layers, a reference layer and a free layer (fig. 4.1). The reference layer usually has a fixed magnetization, this requires the magnetic material composing it to display a high perpendicular magnetocrystalline anisotropy. The free layer has a controllable magnetization that can be switched along both directions of its uniaxial anisotropy axis. These two directions represent a 0 or a 1 bit. The information on the direction of the free layer can be gathered using the properties of giant magnetoresistance (GMR) [74], stating that the resistance measured depends on the orientation of the magnetization in the layers. When the layers have parallel magnetization the measured resistance is low. Respectively, when the layers have anti-parallel magnetization orientation the measure resistance is high.

Originally the free layer was conceived to be switched with an external field, however,

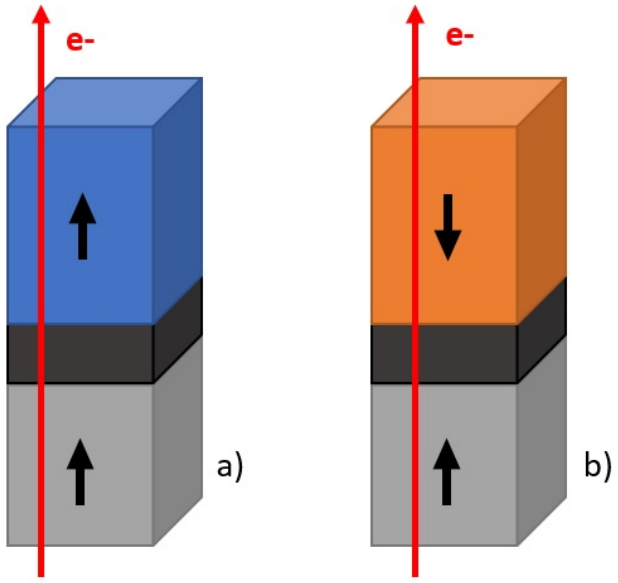

Figure 4.1: Two spin valves with perpendicular magnetocrystalline anisotropy composed of a reference layer (grey), a non-magnetic spacer (black) and a free layer. a) The magnetization of the free layer is parallel to the reference layer, the measured resistance is low. b) The magnetization of the free layer is anti-parallel to the reference layer, the measured resistance is high.

this leads to difficulties in terms of scaling. The fields have to be focused on a small area and the anisotropy should be low enough to allow for the switching, while still being high enough to provide reasonable thermal stability. Recently, efforts are focusing on an alternative way to switch the magnetization of the free layer: interface spin transfer torque. As described in section 3.1, the electrons traveling through the reference layer get polarized in the direction of its magnetization. Since the spacing layer is thin enough, this polarization is not lost when they enter the free layer. The momentum can then be transferred from the electrons to the free layer. This way the free layer can be switched by applying only a current, using the same channel as the current employed to read the orientation of the bit through GMR.

This technique does not require any external field and thus provides much better scalability. However, in terms of computation, the equations described in section 3.1 can not be used here. Indeed, the considered system is not continuously magnetic anymore because of the spacing

layer. In most cases the magnetization of the layers are considered uniform therefore only the spin transfer occurring at the interface is relevant to the dynamics. To simulate the interface spin exchange, the model requires a specific format: the meshes of the surfaces composing this interface have to be the same so the nodes can be made to correspond two by two. Each couple of nodes will compute part of the spin transfer through an additional torque. The torque exerted by layer 2 on layer 1 can be written as [75]:

$$\boldsymbol{T}_{STT,2\to1} = -\eta(\theta)\gamma\frac{p_0 p_1 \hbar J}{2\delta_1 e}\mathbf{M}_1 \times \mathbf{M}_1 \times \mathbf{M}_2 - \eta(\theta)\beta\gamma\frac{p_0 p_1 \hbar J}{2\delta_1 e}\mathbf{M}_1 \times \mathbf{M}_2\,, \tag{4.1}$$

and respectively the torque exerted by layer 1 on layer 2 is:

$$\boldsymbol{T}_{STT,1\to2} = -\eta(\theta)\gamma\frac{p_0 p_2 \hbar J}{2\delta_2 e}\mathbf{M}_2 \times \mathbf{M}_2 \times \mathbf{M}_1 - \eta(\theta)\beta\gamma\frac{p_0 p_2 \hbar J}{2\delta_2 e}\mathbf{M}_2 \times \mathbf{M}_1\,, \tag{4.2}$$

where $\mathbf{M}_1$ and $\mathbf{M}_2$ are the magnetizations of the nodes on layer 1 and 2, γ is the gyromagnetic ratio, p_0 is the polarization efficiency of the spacing layer, p_0 and p_1 are the polarization efficiency of layer 1 and layer 2, $\hbar$ is the reduced Plank constant, J is the current density, δ_1 and δ_2 are the effective thicknesses of the considered nodes on layer 1 and layer 2, e is the electron charge and β is the adiabatic parameter. η is a parameter that describes the angular dependence of the spin-transfer torque efficiency and can be expressed:

$$\eta(\theta) = \frac{q_+}{A + B\cos\theta} + \frac{q_-}{A - B\cos\theta}\,, \tag{4.3}$$

where q_+, q_-, A and B are parameters and $\cos\theta$ is the angle between the magnetizations of layer 1 and layer 2, $\cos\theta = \mathbf{M}_1 \cdot \mathbf{M}_2$. In many models of spin valves, the angular dependence is regarded as flat and we consider $\eta(\theta) = \eta_0$.

The current density at these nodes has to be calculated from the total current density. Indeed, GMR has to be taken into account, meaning that depending on the uniformity of the orientation of the magnetization, the current density might not be the same at every node. Each interface node couple corresponds to a self resistance given by:

$$\rho = 1 + r_{MR}\frac{1-\cos\theta}{2}, \tag{4.4}$$

where r_{MR} is the giant magnetoresistance ratio defined as:

$$r_{MR} = \frac{R_{AP} - R_P}{R_P}, \tag{4.5}$$

where R_{AP} and R_P are the resistances of the system in the anti-parallel and parallel configurations respectively.

The spin-transfer torques (4.1) and (4.2) have to be added to the LLG equation (2.1) when computing the dynamics of surface nodes. However, for convenience, it is possible to rewrite the STT torques in the explicit form of the LLG equation as effective fields. (4.1) would become:

$$\mathbf{H}_{STT,1\to2} = \eta(\theta)\frac{p_0 p_1 \hbar}{2e\delta_1 M_{s1}}\mathbf{M}_1 \times \mathbf{M}_2 + \beta\eta(\theta)\frac{p_0 p_1 \hbar}{2e\delta_1 M_{s1}}\mathbf{M}_2 . \tag{4.6}$$

Finally, the LLG equation including interface spin-transfer torque for a node on the surface of layer 1 would be written:

$$\frac{d\mathbf{M}}{dt} = -\frac{\gamma}{1+\alpha^2}\mathbf{M}\times(\mathbf{H}+\mathbf{H}_{STT,1\to2}) - \frac{\alpha\gamma}{1+\alpha^2}\mathbf{M}\times\mathbf{M}\times(\mathbf{H}+\mathbf{H}_{STT,1\to2}) . \tag{4.7}$$

4.2 Switching efficiency

Section 4.1 established that due to spin transfer torque (STT), a polarized current can induce magnetization switching or precession. Those effects are promising technologies for two different application STT-MRAM (magnetic random access memories) and STT-NO (nano-oscillators). One of the present challenges to implement STT-MRAM lies on the reduction of the critical current whereas STT-NO depends on the maximum output power and the narrower frequency bandwidth of the oscillations possible. To improve these two technologies many studies have been performed to find optimal materials and geometries. For instance perpendicular magnetic anisotropy materials have shown to improve both switching current for STT-MRAM[76, 77] and the output power for STT-NO[78, 79]. However up to now, most of the studies have considered free layers with uniform magnetization. More complex structures like hard/soft magnetic bilayers were studied for their interesting magnetic properties[80, 81] and magnetic recording performance[82, 83, 84, 85]. In this case using an external magnetic field and depending on the bilayer structure a domain wall nucleated in the soft layer can be pinned or propagate through the hard layer. If pinned the domain wall can then be compressed on the energy barrier created by the hard layer[80]. For applications, it was shown using a macrospin model that such structures could provide a lower switching field for a given thermal stability[86]. In this section, we are studying the effect of spin transfer torque on a perpendicular hard/soft structure. Our goal is to answer basic questions such as can a domain wall be nucleated, pinned, and compressed by a polarised current as it is possible with a magnetic field? Do we have to consider both interface and bulk spin transfer torques? As well as more technology related questions such as how is the switching current affected by the hard/soft structure?

We used the FastMag micromagnetics code[64] to simulate the behaviour of a spin valve containing a hard/soft composite free layer under an applied polarized current. The z axis is defined as the direction along the magneto-crystalline anisotropy axis, perpendicular to the film

plan. Current is regarded as positive when electrons are flowing in the $+z$ direction. The first sample geometry considered is a pillar structure with a $5x5nm^2$ section (fig. 4.2). Its magnetic structure is divided in two blocks: a 5nm-thick polarizer (reference layer) and a 7 to 20 nm-thick composite free layer, separated from each other by a 1 nm non-magnetic spacer. The reference and free layers are considered fully decoupled with respect to the exchange interaction, which allows us to focus on the influence of the polarized current flowing through the composite free layer. All layers have perpendicular magnetocrystalline anisotropy along the z axis. The composite free layer is made of a soft and hard sublayer having respectively a uniaxial magnetic anisotropy constants $K_S = 1.5 \times 10^4 erg/cm^3$ and $K_H = 1.5 \times 10^7 erg/cm^3$, and a saturation magnetization $M_S = 800 emu/cm^3$ and $M_H = 200 emu/cm^3$, respectively. The damping parameter was chosen to be $\alpha = 0.05$. The initial magnetization of the reference layer and the free layer are along $-z$ and $+z$ directions, correspondingly.

The micromagnetic simulations are based on the solution of the Landau-Lifshitz-Gilbert-Slonczewsky equation modified to take into account the effect of both the spin-transfer torque in the bulk, as defined in section 3.1, as well as the spin-transfer torque at the interface defined in section 4.1. The finite elements simulations were done using a cell size of 1 nm.

For purposes of later comparison, we first consider the magnetization response of a 15-nm-thick soft layer and a 5-nm-thick hard layer under the influence of an external magnetic field and in the absence of current through the stack. Figure 4.3 shows that an external field applied to this structure can lead to a domain wall nucleation in the free layer, compression of the domain wall when the field is increased, represented by the fact that the average z component of magnetization gets lower, and eventually its propagation through the hard layer when the field becomes strong enough. All these observations are in accordance with typical calculations involving applied magnetic fields[80, 87].

Figure 4.4 shows that similarly to an applied field, current can lead to domain wall nucleation, compression and propagation owing to spin transfer torque. Since the magnetization

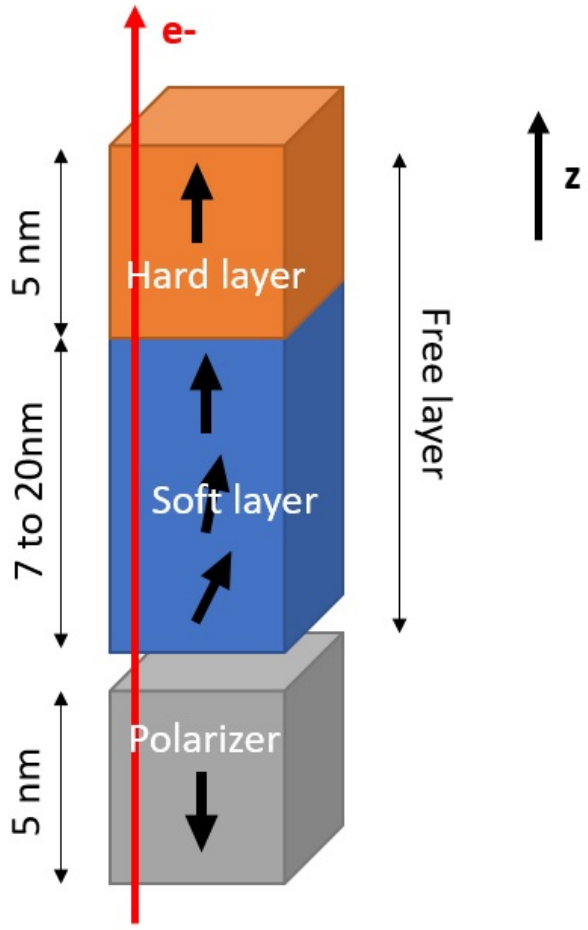

Figure 4.2: Stack composed of a reference layer (polarizer) and a composite free layer (hard layer and soft layer). The cross section is $5x5nm^2$.

along the thickness of the free layer is not uniform, continuous spin transfer torque within this layer has to be accounted for in the calculations. In our model, the interface and bulk contributions to the spin transfer torque are modulated separately by introducing an efficiency coefficients for the STT in the bulk of the layers and for STT at the interface. Two distinct STT polarizations, therefore, appear in the model: p_i for the interfacial STT and p_b for the bulk STT. The relative efficiency of bulk STT with respect to interfacial STT we represent using the ratio $p_r = \frac{p_b}{p_i}$. For these cases p_i was chosen to be 1. The physical behavior of the domain wall is qualitatively similar for various values of p_r. However, this parameter can be tuned to adapt the device to

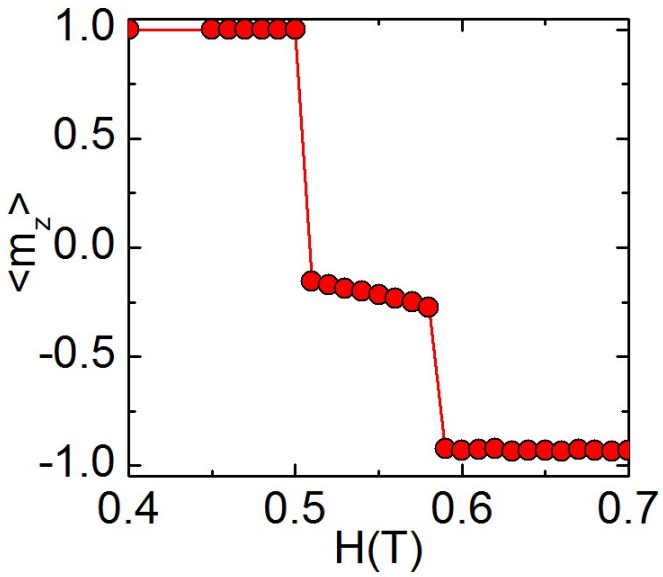

Figure 4.3: Average of the z component of the magnetization in the $5x5x20nm^3$ composite free layer as a function of a field applied along the z axis, in the absence of current.

adequate values of applied current depending on different technology and materials.

From the reversal curves in fig. 4.4, two characteristic current values can be extracted: the nucleation current I_n that corresponds to the minimum current required to nucleate a domain wall in the structure corresponding to $\langle M_z \rangle < 1$, and the propagation current I_p that indicates the complete reversal of the free layer. Between the two stages, the pillar is in a current-sustained state which exhibits a domain wall in the soft part of the free layer. The bulk STT tends to push the domain wall towards the hard layer and compress it, while the exchange interaction opposes this compression. Similarly to what happens under an applied field, domain wall compression becomes greater when the current (and hence bulk STT) is increased. The bulk STT, therefore, has a large impact on I_p where larger values of p_r will lead to reversal at less current.

Figure 4.5 highlights the influence of the soft sublayer thickness t_S on I_n and I_p for two values of p_r while keeping the hard sublayer thickness constant to 5 nm. Increasing the soft layer thickness from a small value strongly decreases I_n and I_p as the switching is facilitated. For $t_S > 10nm$, I_n becomes relatively stable. The nucleation of a tilt in the free layer essentially comes

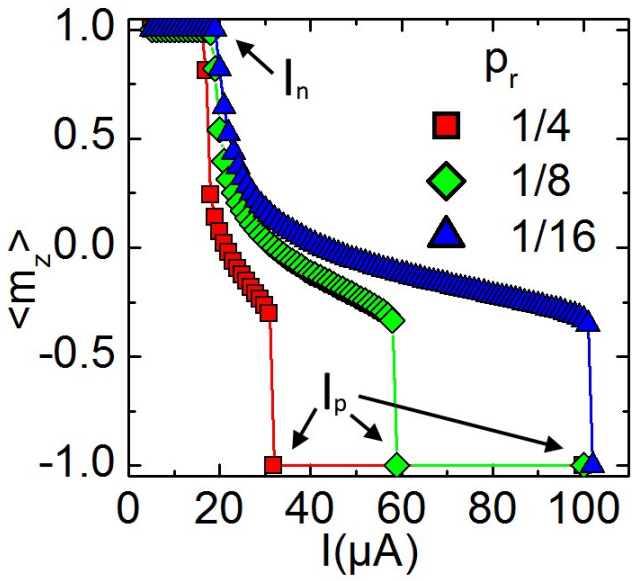

Figure 4.4: Average of the z component of the magnetization in the $5x5x20nm^3$ composite free layer as a function of applied current for different polarization ratios p_r.

from the interface spin transfer interaction with the reference layer, hence the small difference between $p_r = \frac{1}{4}$ and $p_r = \frac{1}{8}$. On the other hand, I_p strongly depends on bulk STT to push the domain wall through the hard sublayer. For this reason I_p is greatly reduced for $p_r = \frac{1}{4}$. We can observe that I_p saturates for large enough values of t_S. This is explained by the fact that once a domain wall is fully nucleated, it can be pushed through an arbitrarily long distance by bulk STT in an ideal case with no defect.

In the case of magnetic field-driven reversal, composite structures can improve the efficiency of the switching process[85, 87, 88, 89, 90, 91]. Calculations were performed in order to investigate the role of hard and soft thicknesses on optimization of switching current and thermal stability of such systems. The model involves a 7-nm-thick free layer with t_S ranging from 0 to 7 nm and $t_H = 7nm - t_S$. The cross sectional area of the stack is $5 \times 5nm^2$ and the reference layer is 3-nm thick. The anisotropies for the hard and soft layers being used are $K_H = 1.5 \times 10^7 erg/cm^3$ and $K_S = 1.5 \times 10^6 erg/cm^3$, respectively. The anisotropy of the reference layer is $K_R = 1.0 \times 10^8 erg/cm^3$. The saturation magnetization of the free and reference

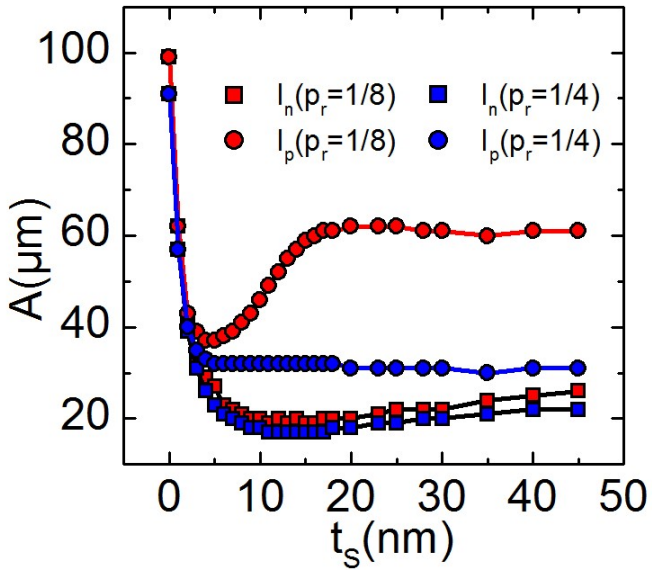

Figure 4.5: Evolution of the nucleation current I_n and the propagation current I_p depending on the soft sublayer thickness for two values of the polarization ratio p_r. The cross section is $5x5nm^2$ and the hard sublayer thickness is $5nm$.

layer are 800 emu/cc and 200 emu/cc, respectively. The damping parameters were chosen to be $\alpha_f = 0.02$ for the free layer and $\alpha_r = 1$ for the reference layer.

For each structure corresponding to the different values of t_S, the thermal stability was calculated by the nudged-elastic-band (NEB) method using the FastMag simulator[64, 92]. This method finds the minimum energy path between the initial (free layer up) and final (free layer down) states of the stack, from which we obtain the energy barrier ΔE (fig. 4.6a). This barrier gives the thermal stability of the system. It corresponds to the minimum amount of thermal energy required to switch the free layer. The mode of thermally driven reversal for the modelled structures is uniform rotation of the magnetization, and ΔE decreases linearly with t_S, as expected.

The critical current density for switching J_c was obtained by solving the LLG equation for two cases: in one case, the bulk STT polarization was set to 1, and in the other case, it was ignored (polarization set to 0). In both cases the interfacial STT polarization was set to 1. Comparison of the two cases will highlight the effect of the bulk STT on the reversal process.

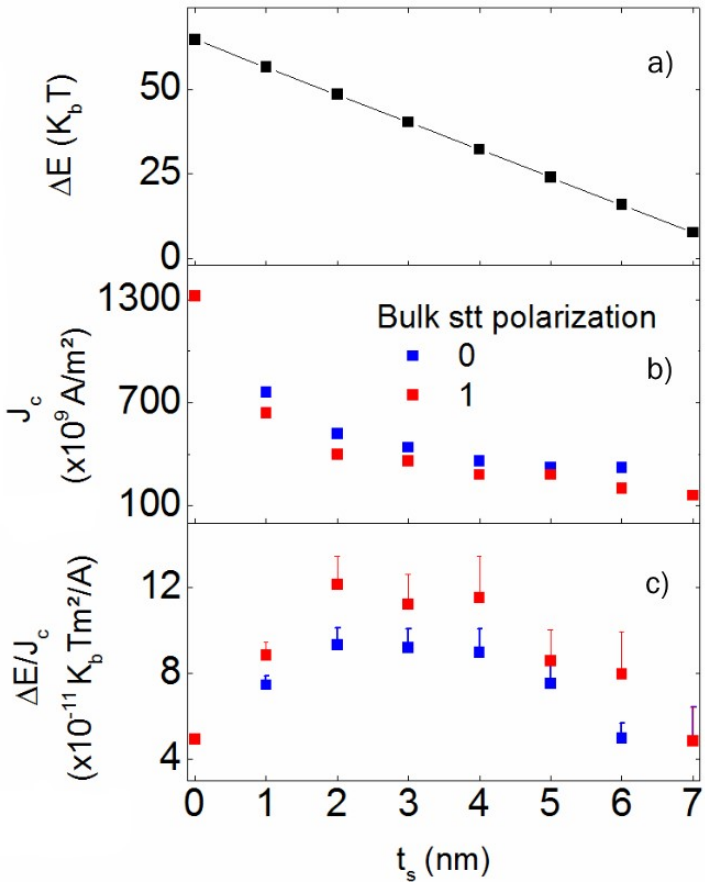

Figure 4.6: a) Energy barrier ΔE of the minimum energy path for the reversal of the composite free layer as a function of soft layer thickness. b) Critical current density J_c for reversal of the free layer as a function of soft layer thickness for a bulk stt polarization of 0 and 1. c) switching efficiency defined as $\frac{\Delta E}{J_c}$. Figures obtained for the case of a $5 \times 5 \times 7nm^3$ free layer.

For $t_S = 0$ or $t_S = 7$ (completely hard or completely soft free layer) there is no magnetization gradient along the thickness during the reversal of the layer. For this reason the bulk STT has no effect on this process and the critical current densities are identical for the two cases considered. For intermediate values of t_S, non-uniformities of magnetization can develop, due to the interface between the soft and hard layers. In these cases, bulk STT helps the magnetization configuration of the free layer to propagate into the hard layer, making it easier to switch. As a result, J_c is smaller when the bulk STT polarization is 1 instead of 0 (fig. 4.6b). Figure 4.6c shows $\frac{\Delta E}{J_c}$ as a function of t_S. This ratio is commonly regarded as the switching efficiency[93]: a high value indicates a device less effected by the trade-off between thermal stability and critical

current necessary for switching (power consumption). For both considered polarization values, it is shown that there is a peak in switching efficiency for t_S between 2 and 4 nm. The efficiency is greater when bulk STT is taken into account. This can be explained by looking at the reversal mechanism. The polarizer is interfaced with the soft part of the free layer, where the electrons induce the switching. In these cases the exchange interaction keeps the magnetization uniform through the soft layer, however the difference in anisotropy with the hard layer creates a small angle between both magnetization vectors: it takes longer for the hard layer to switch. When bulk STT is added to the system, the electrons tend to polarize the hard layer (into which they flow) towards the same direction as the soft layer (from which they come), thus effectively helping the switching process.

Hard/soft composite structures with a larger cross sectional area of $50 \times 50nm^2$ have been studied as well, in order to highlight the effect of lateral size on device characteristics (see fig. 4.7). The same thickness of 3 nm was kept for the reference layer. The free layer thickness, as in the earlier case was 7 nm, with t_S ranging from 0 to 7nm and $t_H = 7 - t_S$. The anisotropies for the hard and soft layers were $K_H = 3.0 \times 10^7 erg/cm^3$ and $K_S = 3.0 \times 10^6 erg/cm^3$, respectively. The anisotropy of the reference layer, saturation magnetization and damping constant were kept the same as the previous case.

The minimum energy paths for the reversal of these structures were calculated by the NEB method as for the smaller model, from which the energy barriers ΔE we obtained (fig. 4.7a). Unlike the results for the $5 \times 5nm^2$ cross-section model, the thermal reversal mode for the larger structures is no longer uniform magnetization rotation, except for $t_S = 7nm$ where the entire free layer is magnetically soft. As soon as the hard sublayer is introduced, the optimal reversal path involves domain wall propagation across the pillar in the lateral direction, as detailed elsewhere[94]. As a consequence, the gain in switching efficiency is much less apparent. When the bulk STT polarization is set to 1, a maximum can be observed for a soft layer thickness around 3 nm. However, the efficiency is only slightly decreased if bulk STT is excluded all together.

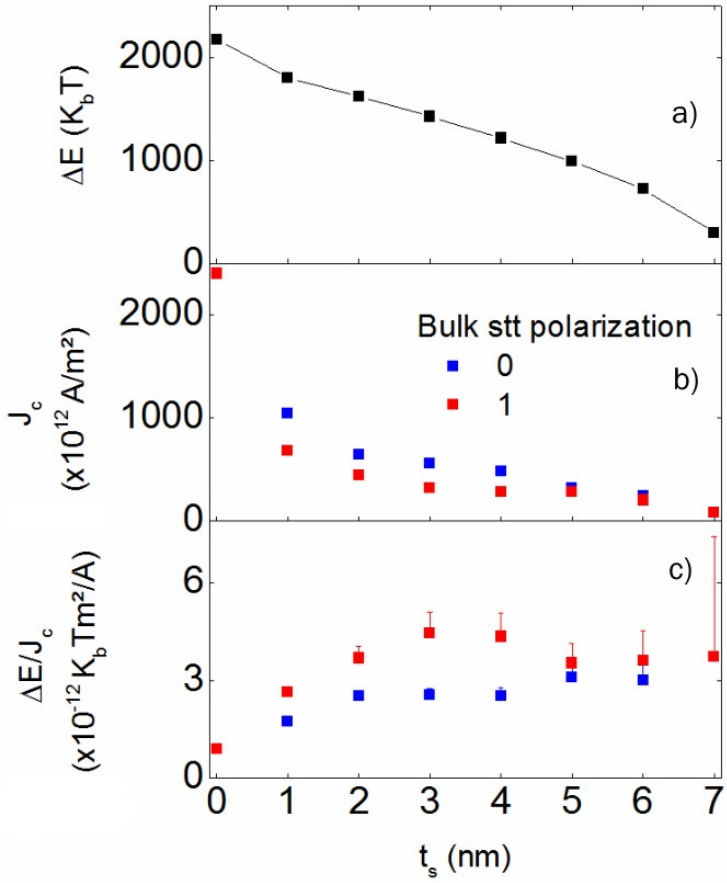

Figure 4.7: a) Energy barrier ΔE of the minimum energy path for the reversal of the composite free layer as a function of soft layer thickness. b) Critical current density J_c for reversal of the free layer as a function of soft layer thickness for a bulk stt polarization of 0 and 1. c) Switching efficiency defined as $\frac{\Delta E}{J_c}$. Figures obtained for the case of a $50 \times 50 \times 7nm^3$ free layer.

These results emphasize how the reversal mode, properties of each sublayer, and their interaction can come to bear in the design of devices optimized for low power consumption and high thermal stability.

In conclusion we have shown that composite layers made of sublayers with different anisotropy values can enhance the switching properties under an applied current in order to reduce the critical switching current and keep a good thermal stability. Moreover, the switching threshold and range of domain wall stabilization depend on the bulk spin transfer torque polarization as well as the interface spin-transfer torque polarization coefficients. The gain in current efficiency in hard/soft structures studied is larger when lateral sizes are smaller and the current-driven reversal

is more uniform.

4.3 Oscillation frequency

In the previous section we were focusing on the impact of composite free layers on the switching efficiency. In this section we will focus on the oscillation regime, which exists for currents such that $I_n < I < I_p$ as shown in fig. 4.4. Indeed, for such values of the applied current, a domain wall has been nucleated but not yet propagated. In this situation, the spins composing the domain wall are oscillating together about the vertical axis of the device (fig. 4.8).

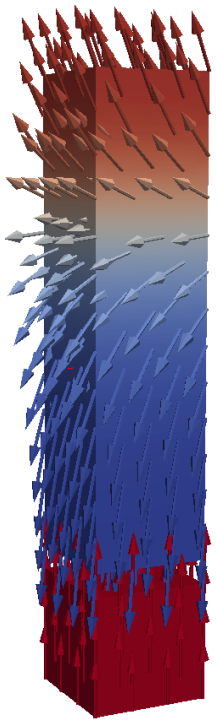

Figure 4.8: Structure of a stabilized domain wall within a composite free layer as simulated by FastMag and represented using ParaView.

The studied model was similar to the first system used in the previous section, with a cross-section of $5 \times 5\text{nm}^2$, a soft free layer with a thickness of 15nm and uniaxial anisotropy $K_S = 1.5 \times 10^4 \text{erg/cm}^3$ and a hard free layer with a thickness of 5nm and uniaxial anisotropy

$K_H = 1.5 \times 10^7 \text{erg/cm}^3$. Once again we consider the polarization ratio $p_r = \frac{p_b}{p_i}$ where p_b is the polarization efficiency of the bulk spin-transfer torque and p_i is the polarization efficiency of the interface spin-transfer torque.

The behavior of the oscillation frequency in a spin valve is well known. If we do not take into account the bulk spin-transfer torque such that $p_r = 0$, we get the results shown in fig. 4.9. Increasing the current density increases the oscillation frequency up to a certain point, after which it starts decreasing.

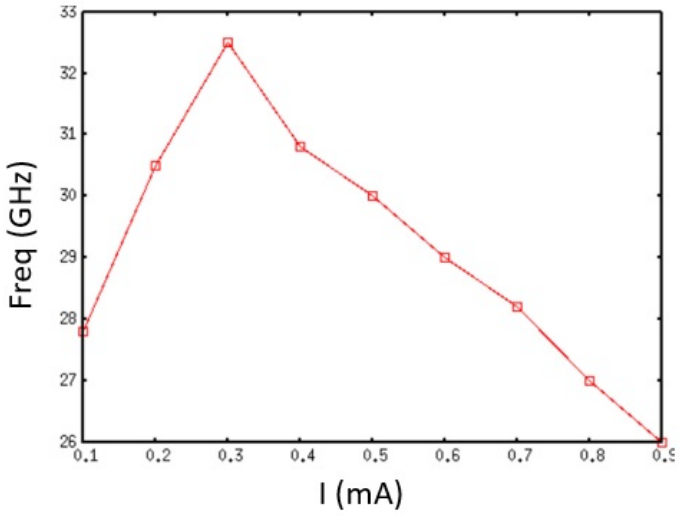

Figure 4.9: Frequency of an oscillating domain wall within a composite free-layer when $p_r = 0$. The limit of the frequency for very low and very high currents is 0.

This result can be understood by looking at what happens at the limits. If no current is applied, there is no precession so the oscillation frequency has to tend to 0. Inversely, if a very strong current is applied, the spin at the bottom of the free layer will be perfectly polarized in the direction determined by the reference layer. If these spins are colinear there can be no precession of one about the other, so the oscillation frequency has to be 0. In between, precession can exist and there must be a critical point where the frequency is at a maximum.

Figure 4.10 shows the frequency of oscillations for different values of p_r when the bulk spin-transfer torque polarization is not 0.

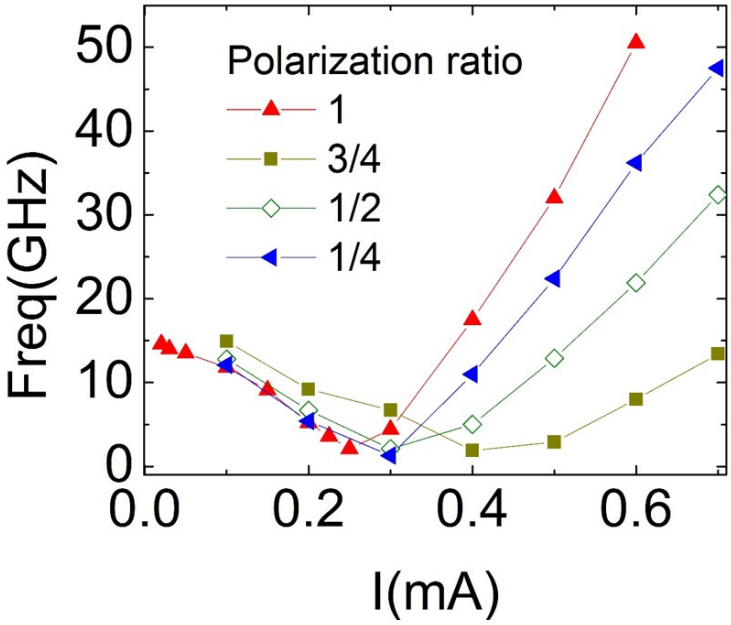

Figure 4.10: Frequency of an oscillating domain wall within a composite free-layer for different values of the polarization ratio p_r.

The results are drastically different from those observed previously. In this case, the frequency first goes down with increasing current, and then goes up. We can complete the analysis by looking at the direction of oscillation of the domain wall. Indeed, the rotation about the central axis before and after the critical point happens in opposite directions. What happens then is that when increasing current, the oscillation frequency progressively slows down, then crosses 0 and the oscillations start again in the other direction. It seems that this methods allows not only for frequency control but also oscillation direction only by fine tuning of the applied current.

To get more insight into this phenomenon and the properties linked to it, it is interesting to study the domain wall profile when the system is in steady-precession mode. This is shown in fig. 4.11.

For each considered polarization ratio, the angle of the magnetization at the bottom of the free-layer is independent from the applied current. This surprising result comes from the fact that

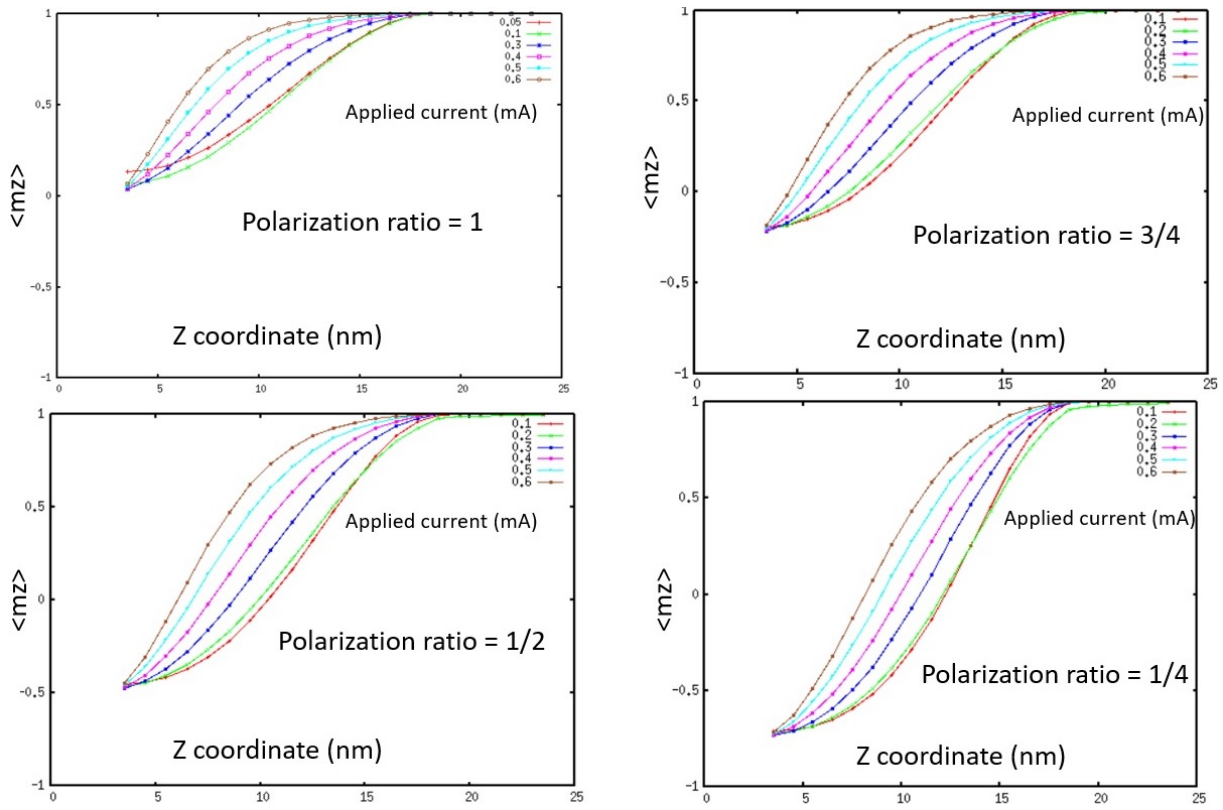

Figure 4.11: Profile of oscillating domain walls for different values of applied current and p_r. The profile is representing the evolution of the z component of the magnetization as a function of the position of the spin along the vertical axis of the free-layer.

the bulk spin-transfer torque and the interface spin-transfer torque compete with each other, and when the applied current is increased their respective contributions are proportionally increased in the same way. Because of this constant angle at the bottom of the free-layer, the explanation for the curve of the domain wall oscillation frequency presented for fig. 4.9 does not hold here. It is to note however that the domain wall becomes more and more compressed as the current is increased, which was expected from the results obtained in section 4.2.

It is clear from these results that the competition between the bulk and interface spin-transfer torque plays a major role in the behavior of domain wall oscillations. To get a better understanding of these results, analytical calculations were performed. A 1-D model for the stack was created, representing it as a single line of exchange-coupled macrospins (fig. 4.12). The dependence of the different interactions on the profile of the domain wall can then be examined.

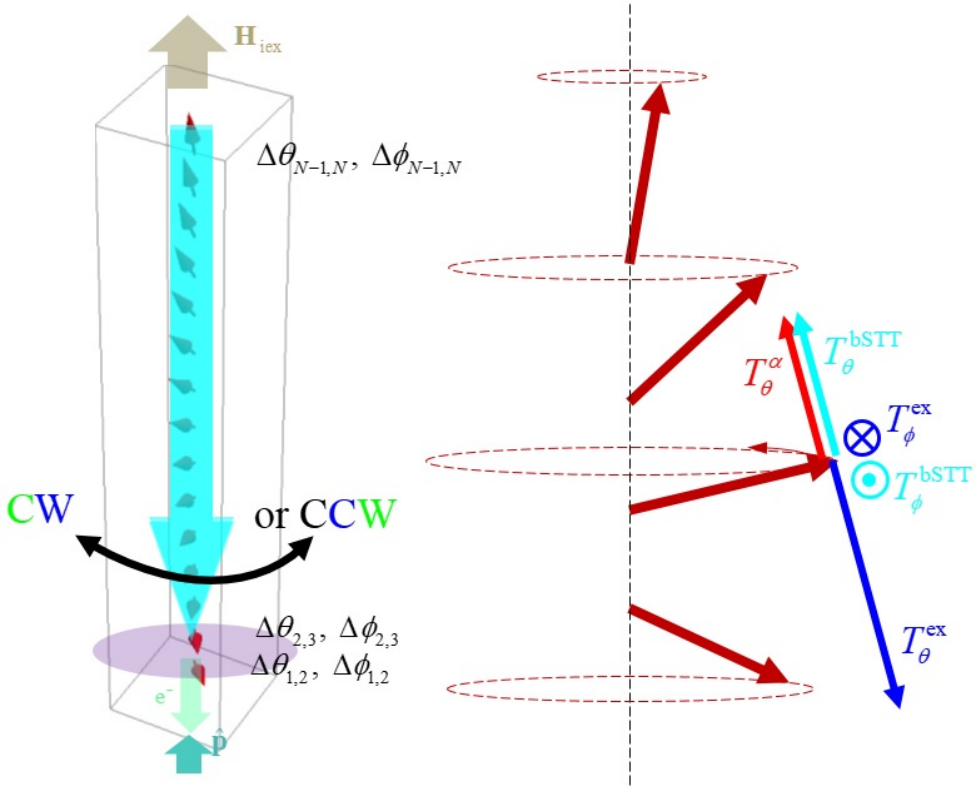

Figure 4.12: 1-D macrospin representation of an oscillating domain wall. The direction of the torques corresponding to the different interactions is represented. The direction of oscillation of the domain wall, clockwise (CW) or counter-clockwise (CCW), depends on the relative strength of the exchange and bulk spin-transfer torques. An external field applied to the last spin of the chain is used to account for the exchange coupling between the soft and hard parts of the free-layer.

The domain wall profile can be expressed through two variables $\Delta\theta_{i,j}$ which is the difference in polar angle between two consecutive spins i and j and $\Delta\phi_{i,j}$ which is the difference in azimuthal angle between these spins. Figure 4.12 shows the orientation of the torques applied on a spin within the domain wall. These torques are decomposed into their polar and azimuthal components. The torques acting on the polar angle are the damping torque T_θ^{α}, the bulk spin-transfer torque T_θ^{bSTT} and the exchange torque T_θ^{ex}. The torques acting on the azimuthal angle, which determines the oscillation speed and direction are the exchange torque T_ϕ^{ex} and the bulk spin-transfer torque T_ϕ^{bSTT}. We know that the dependence on $\Delta\theta_{i,j}$ and $\Delta\phi_{i,j}$ of T^{ex} and T^{bSTT} is not the same because of their theoretical expressions. Indeed, the azimuthal component T_ϕ^{ex} of

T^{ex} becomes greater with $\Delta\theta_{i,j}$ whereas T_{ϕ}^{bSTT} becomes greater with $\Delta\phi_{i,j}$. Inversely, T_{θ}^{ex} gets greater with $\Delta\phi_{i,j}$ and T_{θ}^{bSTT} get greater with $\Delta\theta_{i,j}$. For steady-state precession to exist, the polar angle has to be constant which means that the torques pushing the spins up or down have to compensate each other, leading to $T_{\theta}^{\alpha} + T_{\theta}^{bSTT} = T_{\theta}^{ex}$. The sustained precession then originates from the azimuthal terms T_{ϕ}^{ex} and T_{ϕ}^{bSTT}. When the applied current is increased from a small value for which $T_{\phi}^{ex} > T_{\phi}^{bSTT}$, T_{θ}^{bSTT} becomes greater and helps the damping torque. To counterbalance both of these torques in a steady-state precession, the polar exchange torque has to become greater. Because of this, the azimuthal angle between the spins $\Delta\phi_{i,j}$ increases. Because of its dependence on both the applied current and azimuthal angle difference, T_{ϕ}^{bSTT} becomes larger and contributes more to the compensation of T_{ϕ}^{ex}, effectively reducing the oscillation frequency. There exists a critical current for which $T_{\phi}^{bSTT} = T_{\phi}^{ex}$, in which case the azimuthal torque is completely compensated and the domain wall is not oscillating anymore. For even larger currents, T_{ϕ}^{bSTT} becomes greater than T_{ϕ}^{ex} and now drives the oscillation direction. Increasing the applied current further more will only make the driving torque larger, increasing the oscillation frequency. The phenomenon observed in fig. 4.10 can then be entirely explained by the competition between the torques within the free-layer. The main competing torques are the bulk spin-transfer torque and the exchange torque.

4.4 Conclusion

We have shown that spin valves with composite free-layers exhibit interesting properties that can be taken advantage of under an applied current. The soft sublayer is a way to get low-current domain wall nucleation, while the hard sublayer provides the stability. The presence of bulk spin-transfer torque is important to help the switching by pushing the nucleated domain wall through the hard sublayer therefore the bulk spin-transfer torque polarization efficiency must be maximized to reach high efficiency. Fine tuning of the thicknesses of the soft and hard parts of

the free-layer also play a part in increasing the device performance. This can be done by carefully selecting the materials and growing the device. Any current leak to materials adjacent to the free-layer would impair the device and its efficiency. Another main parameter is the anisotropy properties of the sublayers.

Between the nucleation current at which the domain wall is created in the composite free-layer and the propagation current at which the free-layer switches, there exists an intermediate regime where a domain wall is stabilized into a steady-precession state. In composite spin-valves these domain walls exhibit peculiar properties with their oscillation frequency first going down with increasing current, then stopping and going back up with a reversed oscillation direction. This phenomenon is due to the competition beteween the different torques within the structure, mostly the bulk spin-transfer torque and the exchange torque.

Chapter 5

Influence of the Dzialoshinskii-Moriya interaction on the thermal stability of magnetic spin valves

5.1 Dzialoshinskii-Moriya interactions in micromagnetics

5.1.1 Dzialoshinskii-Moriya interactions

A skyrmion, named after nuclear physicist Tony Skyrme, is represented by a specific local configuration of the magnetization into a bubble shape (fig. 5.1). This pseudo-particle has sparkled a great interest in the last couple of years due to its interesting properties [70, 71, 95]. Indeed it generally has a topological number of 1, meaning that it is a very stable structure that can not be easily destroyed by external perturbations [96, 97, 98]. As such, it makes a great alternative and competitor to domain walls as an elementary bit container in devices like the racetrack memory. Its ability to avoid pinning and escape defects make it one of the best candidates to perfect this technology.

Such a structure, however, is not favored in traditional magnetic systems due to its high

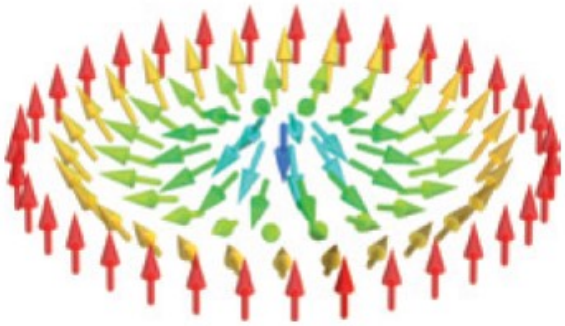

Figure 5.1: Representation of the magnetic configuration in a skyrmion as described in the reference [70].

cost in exchange energy. They are usually stabilized in systems that contain chiral magnetic interactions called Dzialoshinskii-Moriya interactions (DMI). The analytical expression of the DMI energy between two spins $\mathbf{S}_1$ and $\mathbf{S}_2$ is:

$$E_{DMI} = \mathbf{D}_{1,2} \cdot (\mathbf{S}_1 \times \mathbf{S}_2) \,, \tag{5.1}$$

where $\mathbf{D}_{1,2}$ is the DMI vector that depends on the spin orbit torque due to the atoms in the lattice [99]. Contrary to the exchange field that tends to align neighboring spins along the same direction, DMI tends to favor angles between the directions of the spins, creating adequate conditions for skyrmions to exist.

The origins of DMI can be of multiple nature, but the most common one is the interface DMI due to the breaking of symmetry of the lattice at the interface between the magnetic material and a metal with large spin-orbit coupling (fig. 5.3). The magnitude of DMI can reach up to 30% of the exchange interaction [100, 101].

In order to get an expression for the DMI field, we can write (5.1) under its form for a continuous magnetic thin film with a DMI vector along the z axis to get the DMI energy density as [102, 103]:

$$E_{DMI} = D\left(M_z\frac{\partial M_x}{dx} - M_x\frac{\partial M_z}{dx} + M_z\frac{\partial M_y}{dy} - M_y\frac{\partial M_z}{dy}\right) . \tag{5.2}$$

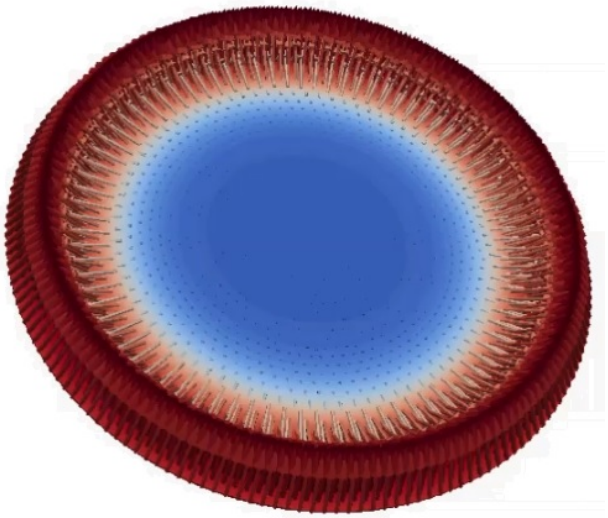

Figure 5.2: Skyrmion inside a 80nm magnetic dot as simulated by FastMag. The blue color indicates down orientation for the magnetization whereas the red color indicates up orientation.

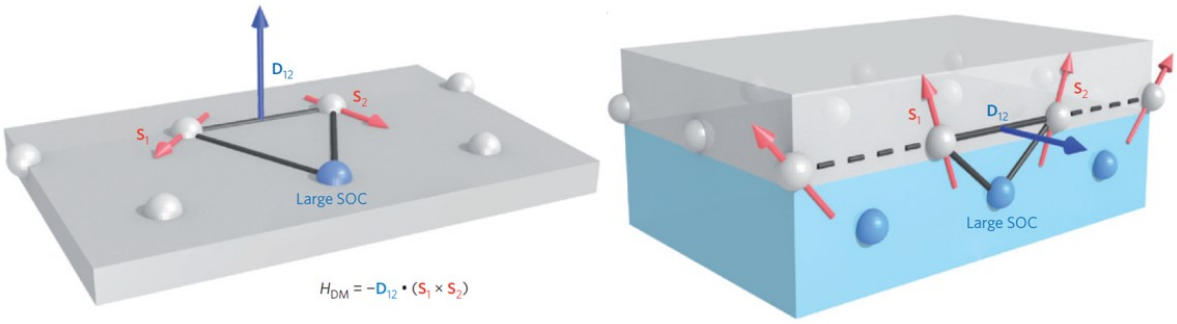

Figure 5.3: Interactions between large spin-orbit coupling metals and magnetic materials give rise to DMI. The direction of the DMI vector depends on the lattice properties. [70]

We can combine (5.2) with (2.7) to derive the DMI field as:

$$\mathbf{H}_{DMI} = \frac{2D}{\mu_0 M_s t} \left[(\boldsymbol{\nabla}_T \cdot \mathbf{M})\, \mathbf{e}_z - \boldsymbol{\nabla}_T M_z \right], \tag{5.3}$$

where D is the DMI energy density in erg/cm^2, μ_0 is the vacuum permeability, M_s is the saturation magnetization, t is the thickness of the magnetic layer and $\boldsymbol{\nabla}_T$ is the gradient operator along the transverse (x and y) directions. This field can be generalized to any DMI vector direction by changing $\mathbf{e}_z$ correspondingly, in which case the transverse directions of $\boldsymbol{\nabla}_T$ are not x and y anymore.

5.1.2 Implementing Dzialoshinskii-Moriya interactions

DMI has been implemented as a part of finite difference solvers for a few years [104]. The method used in these solvers is to consider DMI to be affecting all nodes in the system as if it were a volume interaction, in which case only ultra-thin films can be simulated with accuracy. For FastMag, the choice was made to consider DMI as a surface interaction, as its most common origin is the interface between the magnet and a large spin-orbit coupling metal. This makes the software more flexible and allows for the simulation of DMI applied on thicker models.

Considering the plane containing the interface to be $\{x,y\}$ and its normal being z, the surface formulation of the DMI energy requires the implementation of boundary conditions expressed as [104]:

$$\begin{cases} \frac{\partial M_x}{\partial z} = \varepsilon_i \frac{D_i}{A} \frac{\partial M_z}{\partial x} \\ \frac{\partial M_y}{\partial z} = \varepsilon_i \frac{D_i}{A} \frac{\partial M_z}{\partial y} \\ \frac{\partial M_z}{\partial z} = \varepsilon_i \frac{D_i}{A} \left(\frac{\partial M_x}{\partial x} + \frac{\partial M_y}{\partial y} \right) \end{cases}, \tag{5.4}$$

where i can be either top or bottom to denote if the surface where DMI is applied is at the top or the bottom of the structure and $\varepsilon_{top} = -1$, $\varepsilon_{bottom} = 1$, D is the DMI parameter in erg/cm with $D_{top} = -D_{bottom}$ and A is the exchange constant in erg/cm.

These boundary conditions require the computation of surface magnetization gradients. Let us consider a surface triangle with three nodes n_1, n_2 and n_3 and three sides $\mathbf{l}_i = n_j \vec{n}_k$ (fig. 5.4).

If the surface has an arbitrary orientation the normal unit vector $\mathbf{e}_n$ can be computed as:

$$\mathbf{e}_n = \frac{\boldsymbol{l}_1 \times \boldsymbol{l}_2}{\|\boldsymbol{l}_1 \times \boldsymbol{l}_2\|}. \tag{5.5}$$

Once the normal vector has been calculated the gradient vector corresponding to each side can be found as:

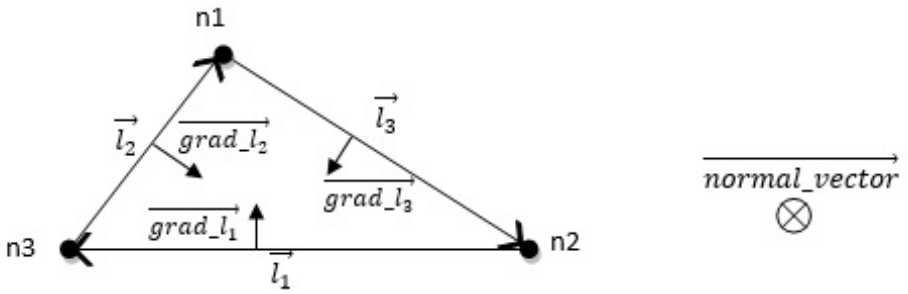

Figure 5.4: Surface triangle for the computation of gradients. $\vec{l_i}$ is the gradient corresponding to node i.

$$\mathbf{grad}_{l_i} = -\frac{1}{h_i}\boldsymbol{l}_i \times \mathbf{e}_n\,, \tag{5.6}$$

where h_i is the height corresponding to node i defined as $\frac{2A}{\|\vec{l_i}\|}$ where A is the area of the triangle.

Let us now consider a node n surrounded by N_T triangles. The contribution of triangle k to the gradient of the x component of the magnetization along the x axis at node n can be expressed using (5.6) as:

$$\frac{\partial M_x|_k}{\partial x} = \sum_{i=1}^{3} M_x(i)\, grad_{l_i,x}|_k\,. \tag{5.7}$$

The total gradient can then be found by summing the values (5.7) corresponding to all surrounding triangles as:

$$\frac{\partial M_x}{\partial x}(n) = \sum_{k=1}^{N_T} \frac{A_k}{A_n}\frac{\partial M_x|_k}{\partial x}\,, \tag{5.8}$$

where A_n is the effective area of node n defined as the sum of all surrounding triangles divided by 3 and A_k is the part of the effective area of node n corresponding to triangle k. $\frac{\partial M_x}{\partial y}$, $\frac{\partial M_y}{\partial x}$, $\frac{\partial M_y}{\partial y}$, $\frac{\partial M_z}{\partial x}$ and $\frac{\partial M_z}{\partial y}$ are found the same way by changing the indices.

The calculation of the magnetization gradients at the surface where DMI is applied allows for the direct computation of the DMI field defined in 5.3 for the relevant nodes. However, boundary conditions still need to be included in the model. If the node is at the edge of the

considered surface, the following boundary conditions applies based on (5.4):

$$\frac{\partial \mathbf{M}}{\partial \mathbf{e}_{n,edge}} = \frac{D}{2At}\left(\mathbf{e}_{n,surface} \times \mathbf{e}_{n,edge}\right) \times \mathbf{M}, \tag{5.9}$$

where $\mathbf{e}_{n,edge}$ is a unit vector in a direction normal to the surface edge and t is the effective thickness.

In order to find the nodes that are at the edge, the sum of all angles from triangles surrounding each node is calculated. It the total edge of a node is less than 360 degrees, we know that this angle is at the edge and we need to apply the condition defined in (5.9).

Result validation

In order to validate the results obtained by DMI simulations, three standard tests have been performed. The first one is based on a well known phenomenon that is that the introduction of DMI favors Néel walls over Bloch walls in thin nanowires [102, 105, 106, 107]. To reproduce this result, a model for 500nm long, 300nm wide and 0.6nm thick stripe was created with a mesh size of 2nm. The saturation magnetization M_s was 1100emu/cc, the exchange constant $A = 1.6 \times 10^{-6}$emu/cm and the perpendicular uniaxaial anisotropy was $K_u = 1.27 \times 10^7$erg/cm^3. The axis direction was the same as in fig. 2.5, meaning that a Bloch wall has its M_x component equal to 0 whereas the Néel wall has its M_y component equal to zero. In this configuration, measuring the x and y components of the average magnetization in the stripe is an efficient way to characterize the domain wall as a Bloch or Néel wall. A domain wall is simulated in the stripe with different values for the D factor regulating the magnitude of the DMI interaction. For each of these values, the M_x and M_y components of the average magnetization are extracted to characterize the domain wall (fig. 5.5).

For a low value of D, $M_x = 0$ meaning that the domain wall is in a perfect Bloch state. When D increases the influence of DMI becomes larger and the domain wall enters a hybrid state with both M_x and M_y being non-zero. For $D > 0.15$mJ/m^2, DMI is strong enough to force the

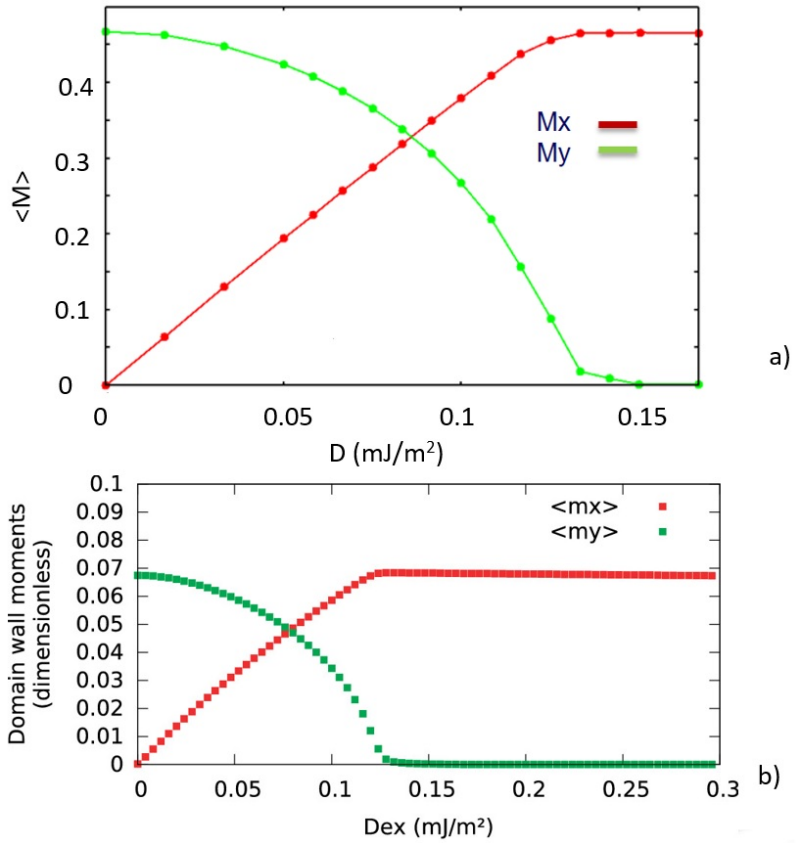

Figure 5.5: Average magnetization of a domain wall in a stripe under the influence of DMI. The stripe is oriented along the y axis and its normal is the z axis. When the D factor increases, the domain wall shifts from a Bloch state ($M_x = 0$) into a Néel state ($M_y = 0$). a) Result obtained from FastMag simulations. b) Result from the reference [105]. The parameters are similar and the shift from Bloch to Néel occurs for similar values of D. The difference in total average x and y magnetization comes from the difference in length considered for the domain wall.

domain wall into a perfect Néel wall state. These results correspond perfectly to those reported in [105] for similar parameters.

The second test consists in evaluating the tilt of the magnetization angle due to DMI at the edge of a magnetic stripe [104]. This test is useful to control the correct implementation of boundary conditions in our DMI simulation. Indeed, these boundary conditions state that the angle of tilting of the magnetization at the edge of a thin stripe oriented along the y axis and normal to the z axis depends on the exchange constant A, the perpendicular uniaxial magnetocrystalline anisotropy K_u and the DMI factor D as follows [104]:

$$M_x = \frac{D}{2\sqrt{AK_u}} = \frac{\Delta}{\xi}, \tag{5.10}$$

where $\Delta = \sqrt{\frac{A}{K_u}}$ is the characteristic domain wall length and $\xi = \frac{2A}{D}$ is the characteristic DMI length.

The model chosen for this test was a 500nm long, 100nm wide and 1nm thick magnetic stripe with a mesh size of 2nm. The saturation magnetization M_s was 1100emu/cc, the exchange constant $A = 1.6 \times 10^{-6}$emu/cm and the perpendicular uniaxaial anisotropy was $K_u = 1.27 \times 10^7$erg/cm^3.

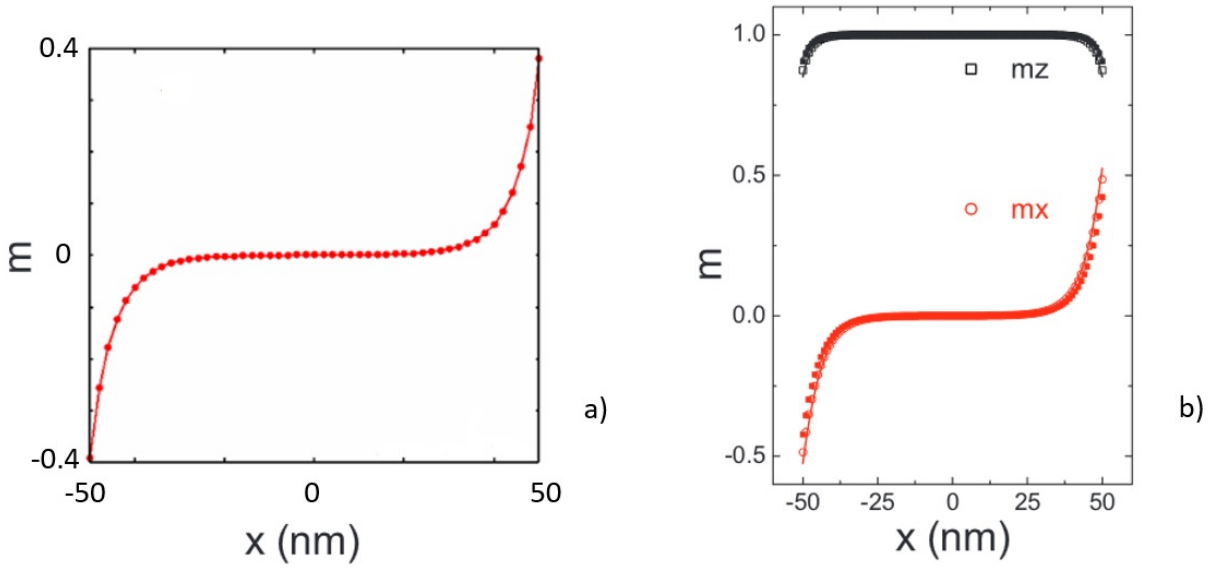

Figure 5.6: Transverse profile of the magnetization within a 100nm wide stripe under the effect of DMI. The tilt of the magnetization at the edge of the stripe depends on the value of the D factor. In this case, $D = 3$mJ/m^2. a) Profile of the normalized x component of the magnetization obtained through FastMag simulations. b) Profile of the normalized x and z components of the magnetization presented in [104]. The results are identical for similar parameters.

The first step is to verify the transverse profile of the magnetization across the stripe. To do so, a fixed value of $D = 3$mJ/m^2 is chosen and the normalized x component of the magnetization is plotted against the x coordinate (along the width of the stripe) on fig. 5.6. DMI tilts the magnetization out of the stripe, leading to negative x component of magnetization at $x = -50$nm

and positive x component of magnetization at $x = 50$nm. The profile observed with the FastMag simulation is identical to the reference, using the same parameters.

The second step is to look at how the tilt of the magnetization at the edge of the structure evolves with the D factor. (5.11) shows that the theory predicts the x component of the magnetization at the edge to be exactly equal to $\frac{\Delta}{\xi}$. The result of the simulation is presented in fig. 5.7.

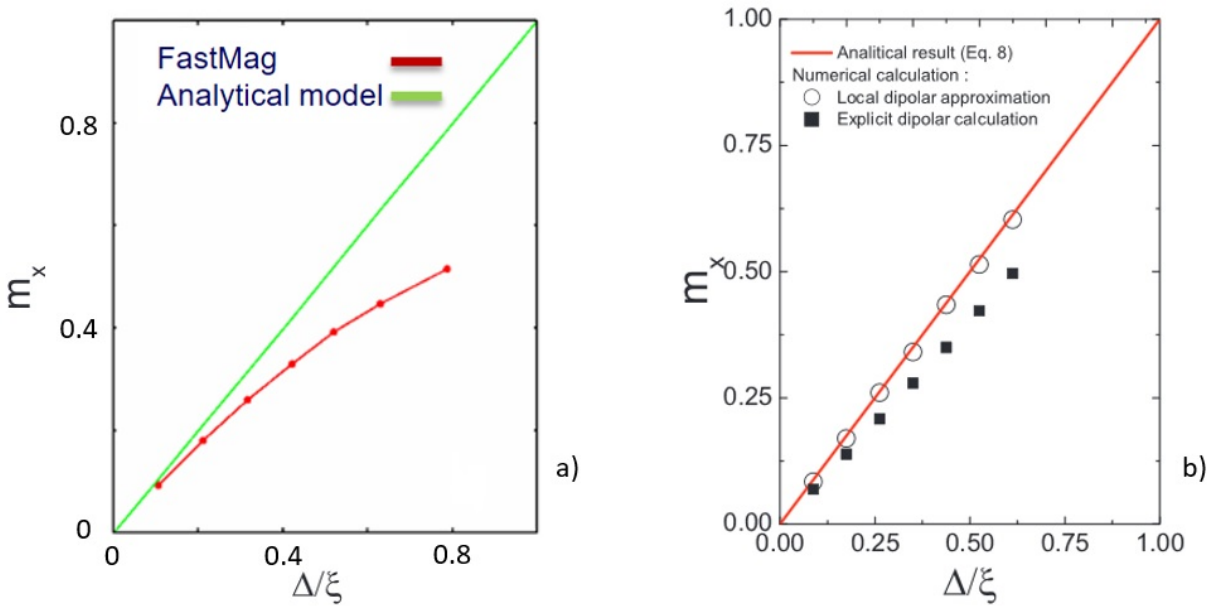

Figure 5.7: Tilting of the magnetization at the edge of a stripe as a function of the DMI factor. The change in the x component of the magnetization at the edge of the structure is shown as a function of $\frac{\Delta}{\xi} = \frac{D}{2\sqrt{AK}}$. a) Result obtained with FastMag compared with the analytical solution. The discrepancy comes from the inclusion of dipolar fields in the FastMag simulation. b) Result presented in [104].

$\frac{\Delta}{\xi} = \frac{D}{2\sqrt{AK_u}}$ is varied by keeping the exchange parameter A constant and changing the D factor from 0 to 5 mJ/mm^2. When no DMI is applied, M_x at the edge of the thin stripe is 0, meaning that the magnetization is perfectly perpendicular to the plane due to the influence of the magnetocrystalline anisotropy. When the D factor is increased, the M_x progressively increases, denoting a tilting of the magnetization. The magnitude of the normalized x component of the magnetization approximately follows the theoretical prediction which is $\frac{\Delta}{\xi}$. However there is a

small discrepancy due to the fact that dipolar fields are not taken into account in the theoretical prediction. The result obtained from the reference [104] presented in fig. 5.7b) shows the presence of the same discrepancy when dipolar fields are computed. Moreover, the results are similar to those obtained with FastMag.

The last test consists in verifying the energy of a system under the influence of DMI. A domain wall in a magnetic stripe with perpendicular anisotropy is a good candidate for such a test. Indeed, when taking into account DMI, the domain wall energy density becomes [102]:

$$\sigma_{DW} = 4\sqrt{AK} - \pi D\,, \tag{5.11}$$

The energy test can be performed by simulating a domain wall in a stripe for different values of D and outputting the computed domain wall energy density. We can then compare the obtained slope with the theoretical value expected from (5.11): the slope of the energy density as a function of D should be $-\pi$. The model was a 100nm long, 30nm wide and 0.6nm thick stripe with a perpendicular uniaxial anisotropy $K_u = 5.1 \times 10^6$erg/cm^3 and a exchange constant $A = 1.6 \times 10^{-6}$emu/cm. The effects of the dipolar field are neglected for this test to get result as close to the theory as possible. The results are shown in fig. 5.8.

For $D = 0$, the expected value of the domain wall energy density of $4\sqrt{AK_u}$ is obtained. When D is increased, the domain wall energy density is proportionally decreased with a slope of -3.06 which is very close to the theoretical value of $-\pi$. This way, we demonstrate that the DMI energy is correctly computed with FastMag.

Another possible test could be to measure the total energy of a magnetic disk in a uniformly magnetized state and in a skyrmion state for different values of D. [103] provides a reference for such a test.

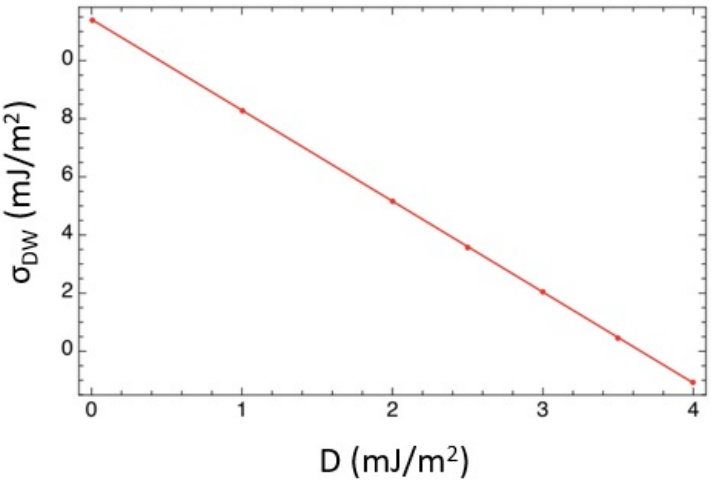

Figure 5.8: Energy density of a domain wall simulated by FastMag as a function of the DMI factor. The slope obtained is approximately $-\pi$, corresponding to the theoretical value.

5.2 Effects of Dzialoshinskii-Moriya interactions on the thermal stability

DMI is known for stabilizing complex structures as skyrmions and providing interesting material properties. However, in a more pragmatic sense, it is useful to study cases in which DMI can be viewed as parasitic. STT-MRAM stacks are an interesting subject in this case. An STT-MRAM system usually consists in a magnetic reference layer for spin polarization and a magnetic free layer for bit writing typically based on CoFeB, separated by a non-magnetic metal, typically MgO. Various other layers can usually exist, including capping layers on top of the free-layer and antiferromagnetically coupled layers used to compensate the stray field. To enhance the thermal stability of the system, additional high-spin orbit coupling elements are often introduced, such as Ir, W or Pt. However, as shown in section 5.1, interfaces between ferromagnets and high spin orbit coupling metals create favorable conditions for the appearance of DMI in the system. It becomes then important to understand what effect DMI yields on the performance of STT-MRAM stacks in terms of switching current and in terms of thermal stability [2]. Simulations were performed with FastMag to address this point. The nudged elastic band

method described in section 2.6 can be used to calculate the variations in energy barrier due to DMI in a STT-MRAM stack, thus understanding how it impacts the thermal stability.

The energy barrier for the switching of an MRAM free layer usually corresponds to the difference between the energy of the uniformly magnetized state (lowest possible energy) and the state where a domain wall exists at the center of the layer (highest possible energy). The first step is to simulate the influence of DMI on the energy of these two states, to see if the energy barrier is modified. In order to perform these simulations, a MRAM stack model was created with a diameter of 32nm, a thickness of 1nm, a perpendicular uniaxial magnetocrystalline anisotropy $K_u = 7.7 \times 10^6 \text{erg/cm}^3$, a saturation magnetization $M_s = 1030$ emu/cc and an exchange constant $A = 10^6$ erg/cm. The results are shown in fig. 5.9.

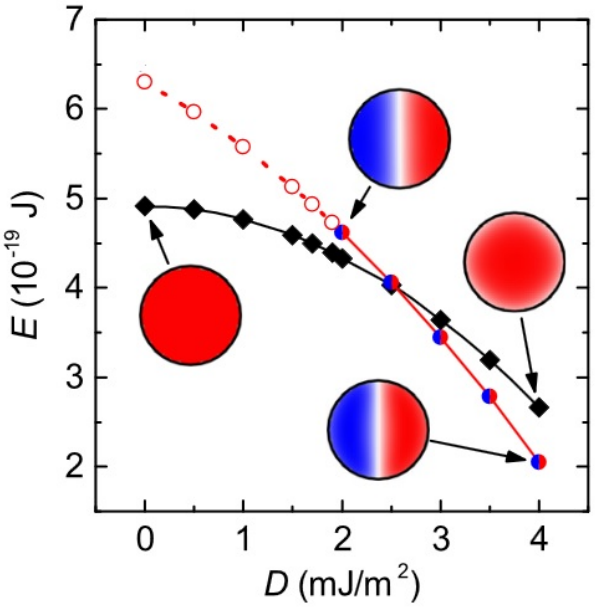

Figure 5.9: Energy of the uniform state and the domain wall state in an MRAM free layer as a function of the DMI factor as simulated by FastMag. The black line corresponds to the energy of the uniform states whereas the red line corresponds to the domain wall state. Open circles denote metastable states. Insets represent the magnetic configuration of the dot.

For $D = 0$ the domain wall is a metastable state and its energy is much higher than the energy of the uniform state, ensuring that the free-layer is always either in the up or down uniform state. When D increases, the energy difference between these states decreases, showing that the

energy barrier becomes smaller, thus impacting the thermal stability of the device. For $D > 2$, the domain wall state becomes stable, meaning that it can be pinned within the layer during the switching. This case would be very detrimental to actual MRAM devices because it would result in greatly increasing writing errors. When D is further increased, the domain wall state becomes more stable than the uniform state, leading to non-functioning devices. Controlling the magnitude of DMI appears to be important for such applications where it yields a parasitic effect and can greatly decrease the efficiency of the device.

Additional insight can be gained by computing the full path taken by the magnetization to go from one uniform magnetization state to the opposite one. This work is presented in fig. 5.10.

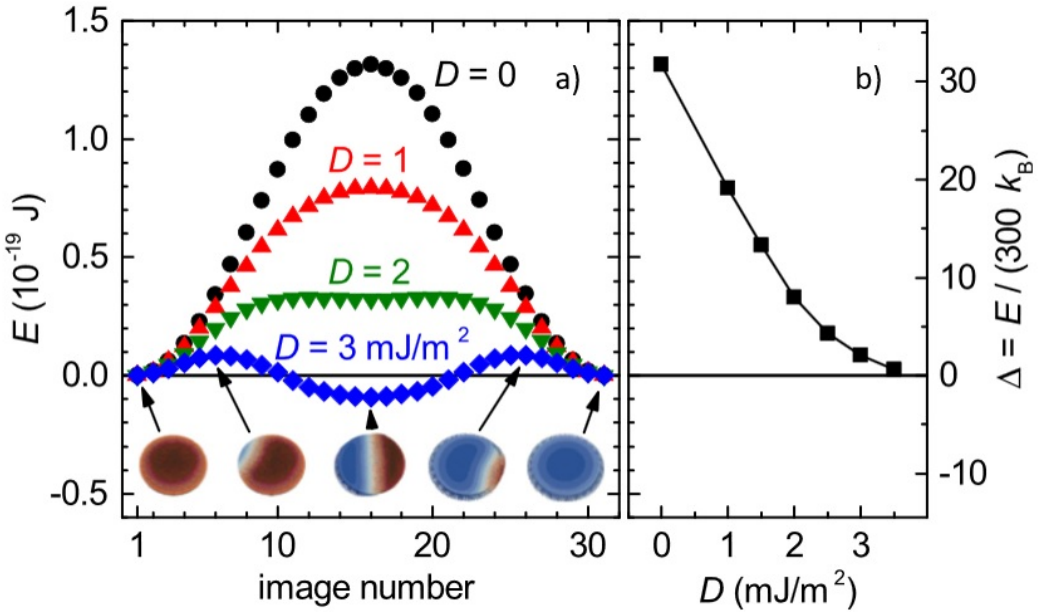

Figure 5.10: a) Energy profile for the switching of a free layer for different values of the D factor as computed using the nudged elastic band method on FastMag. Insets show the magnetization state at different stages of the reversal process. b) Energy barrier calculated from a).

Figure 5.10a) shows the shape of the energy barrier for different values of the D parameter. When $D = 0$, the barrier has a classical bell shape with a maximum energy value corresponding to the state where a domain wall is located at the center of the magnetic dot. When D is increased, the barrier goes down and the top of the bell shape flattens, meaning that the domain wall state

becomes more and more stable. For $D = 2$, the states for which a domain wall exists in the dot almost all have the same energy. Moreover, a domain wall centered in the dot is stable, i.e. a small amount of energy has to be brought to the system for it to go back to a uniform state. Finally, for larger values of D, the domain wall state becomes more stable than the uniform state, which corresponds to negative total energy in the figure. It is interesting to note that there is a barrier separating the uniform and domain wall states, corresponding to some energy required to nucleate the domain wall. By symmetry, this barrier appears twice. Figure 5.10b) shows the evolution of the energy barrier as a function of the d parameter. For small values of D, this barrier decreases linearly with the DMI factor. However, when the domain wall state becomes stable (for $D > 2$), the computed barrier now has a different meaning since the maximum of energy corresponds to the domain wall nucleation. This required energy progressively tends to 0 in a non-linear fashion.

This study shows that DMI introduces two negative effects when evaluating the performances of STT-MRAM. It contributes to reducing the energy barrier, and this way it reduces the thermal stability and memory lifetime of the device, impacting on its reliability. Moreover, it tends to make domain wall states more stable within the free-layers, potentially creating issues with badly-written bits that are stuck in intermediate states. Interfaces between the free layer and high spin orbit metals can exist in such systems, however the DMI induced by these materials can be of variable magnitude: 7 mJ/m^2 in the case of Ir/Fe monolayers[101], 1.2 mJ/m^2 for Pt/CoFe/MgO[108] or 0.053 mJ/m^2 for Ta/CoFe/MgO[108]. According to our results, values as small as 0.5 mJ/m^2 for the D factor can already have a considerable impact on the perforamce of the device with a thermal stability decreased by more than 10% (fig. 5.10b)), which is why particular care has to be taken when selecting the materials.

Aknowledgement: This chapter is based on the contribution I have brought to the journal article authored by J. Sampaio [2], with the following co-authors: A. V. Khvalkovskiy, M. Cubukcu, D. Apalkov, V. Lomakin, V. Cros and N. Reyren.

Chapter 6

Forward flux sampling method with applied currents

Thermal stability is one of the key parameters to evaluate and improve when designing STT-based devices such as MRAM. In these systems in particular, write error rates (WER) that correspond to the applied current failing to correctly switch the magnetization in the free-layer, and RER (read error rates) that correspond to the reading current unexpectedly switching the free-layer, are critical temperature-dependent metrics that need to be controlled. As shown in section 2.6, NEB can be an efficient method to compute energy barriers from which this thermal stability can be assessed. However, it is not enough to have the full picture. Indeed, the behavior of a device under the influence of a thermal fields depends not only on the shape of the energy landscape in the magnetic configuration space, but also on the type of reversal process involved. An example is shown in fig. 6.1.

In these simulations, two cases are compared: one is a $5 \times 5 \times 5\text{nm}^3$ cube and the other one is an elliptical free-layer with radii of 20nm and 60nm. The saturation magnetoresistance and perpendicular magnetocrystalline anisotropy are chosen such that both of these cases present the same energy barrier of $78k_BT$. The write error rate is then computed by counting the number of

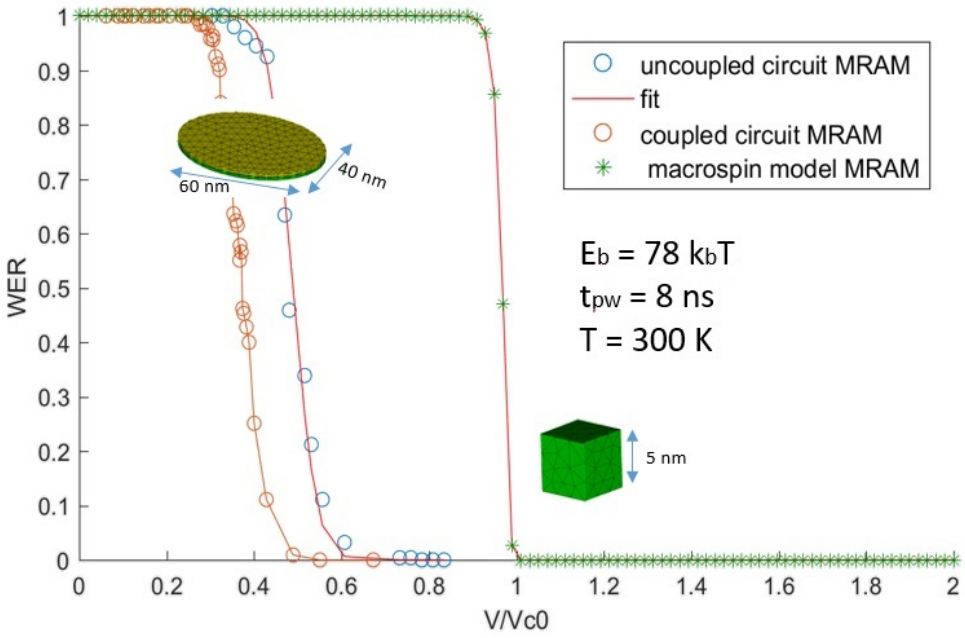

Figure 6.1: FastMag simulations of the write error rates at 300K as a function of the applied voltage for systems with the same energy barrier but different shapes. A $5 \times 5 \times 5\text{nm}^3$ cube and an elliptical free-layer with radii of 20nm and 60nm are compared. Their energy barrier is the same: $78k_BT$ but their thermal behavior is different. The elliptical model is simulated for two different cases: with and without taking into account the response of the circuit to the change of its magnetoresistance.

cases that switch for each given voltage under a temperature of 300K. The higher the voltage, the higher the chances to switch. Thermal fields contribute to the switching by adding some randomness to the behavior of the spins, which can in some cases kick them past the energy barrier. Despite this barrier being the same, the WER observed for both models is very different. Indeed, the current needed to switch the elliptical free-layer is about half the one needed for the cube. Moreover the influence of the temperature is much more pronounced in the case of the cube, the WER appearing to be more vertical. This difference in behavior is due to the reversal process. Indeed, while the $5 \times 5 \times 5\text{nm}^3$ cube is small enough so that the switching of its magnetization happens uniformly, the switching within the ellipse takes the form of a propagating domain wall. The critical factor in this second kind of switching is the domain wall nucleation which can be greatly facilitated by thermal activation. These cases show that the energy barrier does not yield

all the information required to understand the thermal stability of a system, but other factors such as its shape or reversal process have to be taken into account.

Using a simple model, the thermal relaxation time τ of an MRAM stack can be expressed as:

$$\tau = \frac{1}{f_0} e^{\frac{\Delta E}{k_B T}}, \tag{6.1}$$

where f_0 is the attempt frequency with a typical magnitude of 10^9 to 10^{11} Hz, ΔE is the energy barrier of the system, k_B is the Boltzmann constant and T is the temperature. The NEB method can be used to evaluate ΔE. However, the attempt frequency f_0 cannot be found by these means. Moreover the analytical calculation of this parameter can be very complicated for non-trivial cases[109, 110]. For this reason, the forward flux sampling method[111, 112] was introduced to micromagnetics[113], allowing for simpler evaluation of the thermal relaxation time of systems through a probabilistic analysis.

6.1 Forward flux sampling method

The forward flux sampling is a method used to compute directly the thermal rate constant k_{AB}, invert of the thermal relaxation time described in (6.1), that can be expressed as:

$$k_{AB} = f_0 e^{-\frac{\Delta E}{k_B T}}. \tag{6.2}$$

This rate quantifies the thermal stability of the system considering two stable states A and B and the energy barrier ΔE separating them.

In order to do so, n intermediate magnetic configurations $\lambda_0 ... \lambda_{n-1}$ between the A and B states called interfaces are created. Usually, the NEB method provides a good way to create these intermediate states by picking them along the minimum energy path between A and B. A distance

function evaluates how far a given magnetic state is from A. This distance d_A is calculated as:

$$d_A = \sum_{i=1}^{N_{nodes}} \frac{V_{eff}\,|\mathbf{M}(i) - \mathbf{M}_A(i)|}{V_{tot}}, \tag{6.3}$$

where N_{nodes} is the number of nodes in the model, $\mathbf{M}(i)$ is the normalized magnetization vector of the considered magnetic configuration at node i, $\mathbf{M}_A(i)$ is the normalized magnetization vector of the A state at node i, V_{eff} is the effective volume of node i defined as $\sum^{tet} V(\text{thetrahedron})/4$ over all the surrounding tetrahedrons and V_{tot} is the total volume of the model. Using this distance function, $d_A \in [0,2]$.

As an initial step, the initial magnetization is set to be state A. N_0 simulations are run under non-zero temperature. The average time t_{λ_0} required by these simulations to reach a distance $d_A(\lambda_0)$ corresponding the distance to the first interface is calculated. The final states, all corresponding to a magnetic states with a distance $d_A(\lambda_0)$, are recorded.

For the next step, the initial magnetization of each of the N_0 simulations is picked randomly among the pool of states previously calculated with a distance $d_A(\lambda_0)$. For each of these simulations, two cases exist due to the thermal fluctuations: either they relax back to state A, corresponding to a failure, or they reach a distance equal to $d_A(\lambda_1)$, corresponding to a success. The ratio of successes among the N_0 simulations is computed as $P_{\lambda_0}(\lambda_1)$ and the magnetization states of successes are recorded.

This step is repeated to compute $P_{\lambda_i}(\lambda_{i+1})$ up to $P_{\lambda_{n-1}}(\lambda_n)$ where λ_n is the B state (fig. 6.2). Once all of these are known, the relaxation rate k_{AB} can be calculated as:

$$k_{AB} = \frac{1}{t_{\lambda_0}} \prod_{i=0}^{n-1} P_{\lambda_i}(\lambda_{i+1})\,. \tag{6.4}$$

In order for this method to be reliable, the number of simulation per interface N_0 and the distance between the interfaces must be chosen carefully. Indeed, the probabilities $P_{\lambda_i}(\lambda_{i+1})$ need to be computed with a reasonable degree of confidence. An ideal value for $P_{\lambda_i}(\lambda_{i+1})$ should be

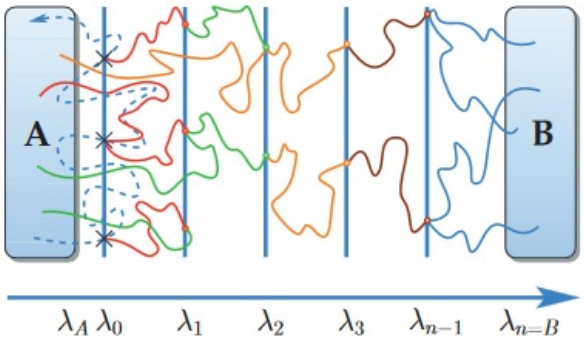

Figure 6.2: Representation of the interfaces in forward flux sampling from [113]. Two states A and B are separated by n interfaces $\lambda_0 ... \lambda_{n-1}$. The probabilities to reach λ_{i+1} from λ_i are multiplied to find the relaxation rate.

around 0.3 and the distance between interfaces have to be adjusted as a consequence. The number of simulations per interface used in this work was $N_0 = 10000$.

The forward flux sampling method was tested with FastMag by comparing the results obtained for a pseudo-macrospin model to the analytical solution. In order to do so, a cube of dimensions $5 \times 5 \times 5\text{nm}^3$ was created with a mesh size of 1nm. It presents a uniaxial anisotropy normal to one of its faces and the parameters were selected such that its energy barrier between one and the other direction of this anisotropy axis is $9k_BT$. Fields of different magnitudes were applied and the forward flux sampling method was used to compute the thermal relaxation time. The results are presented in table 6.1, using H_C as the critical field required to switch the magnetization in the cube for $T = 0K$.

Table 6.1: Comparison of the relaxation time obtained for the forward flux sampling method using FastMag and the analytical calculation.

Applied field (H/H_C)	0	0.1	0.2	0.3	0.4
τ, forward flux sampling (ns)	92	64	62	59	50
τ, analytical (ns)	90	60	58	54	45

6.2 Introducing applied currents

Write and read error rates are major parameters that need to be controlled in order to produce reliable MRAM devices. Because of thermal fluctuations, these operations are not fully deterministic. A simple model for the switching probability P_{SW} of a free layer at a given current I under temperature can be written as:

$$P_{SW} = 1 - \exp\left\{ -\frac{t_{PW}}{\tau_0} \exp\left[-\frac{\Delta E}{k_B T} \left(1 - \frac{I}{I_{C0}} \right)^{\alpha} \right] \right\}, \tag{6.5}$$

where t_{PW} is the current pulse duration, $\tau_0 = \frac{1}{f_0}$ and f_0 is the attempt frequency, ΔE is the energy barrier, k_B is the Boltzmann constant, T is the temperature, I_{C0} is the critical switching current for $T = 0K$ and α is a system parameter. This α parameter also appears in the thermal relaxation time under an applied current that can be written:

$$\tau = \frac{1}{f_0} \exp\left[\frac{\Delta E}{k_B T} \left(1 - \frac{I}{I_{C0}} \right)^{\alpha} \right]. \tag{6.6}$$

Calculating the thermal relaxation time parameters for a system would then give us the full information regarding its switching probability under a given temperature. The energy barrier ΔE can be found using the NEB method, however the forward flux sampling method can be used to find f_0 and α. Indeed, f_0 can be found in the way described in section 6.1 by setting the applied current to 0. Once f_0 is known, α can be computed by simulating the thermal relaxation time for different values of I and performing a fit.

This method was first tested for a macrospin model, as shown on fig. 6.3. The model used for the finite element simulations with FastMag is a $5 \times 5 \times 5\text{nm}^3$ cube with an energy barrier of $5.16 k_B T$. In this simple case, the thermal activation time τ_0 is computed to be 0.38ns and the α parameter is 2.

This method is then applied to a complex structure, which is an ellipse with a domain wall reversal process instead of a macrospin. This ellipse has radii of 20nm and 15nm and a thickness

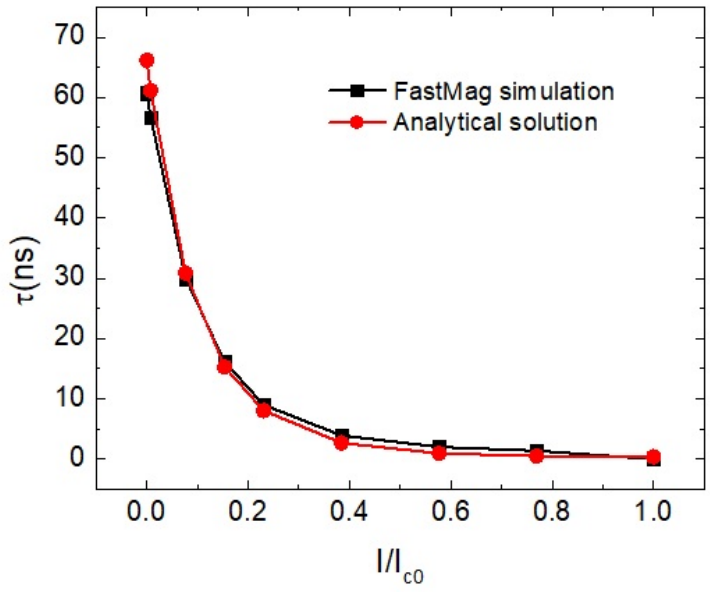

Figure 6.3: Thermal relaxation time of a macrospin calculated from the forward flux sampling and analytical formula. The model used for finite elements simulations is a $5 \times 5 \times 5\text{nm}^3$ cube with an energy barrier of $5.16 k_B T$. The computed thermal activation time is $\tau_0 = 0.38\text{ns}$ and $\alpha = 2$.

of 1nm. The chosen mesh size is 1nm. There is perpendicular magnetocrystalline anisotropy such that the energy barrier corresponds to $12.9 k_B T$. The results are presented in fig. 6.4.

This analytical formula still gives a good approximation for the thermal relaxation time of the elliptical model. The thermal activation time τ_0 is computed to be 8×10^{-4}ns, corresponding to an attempt frequency $f_0 = 1250$GHz. The difference in magnitude observed compared to the macrospin case is notable. This might be due to the reversal process which is a domain wall propagation. Indeed, the key to the reversal lies in the domain wall nucleation, which is a simpler operation than the whole uniform reversal. Moreover the α parameter is found to be 1.6, whereas it was 2 for the macrospin case.

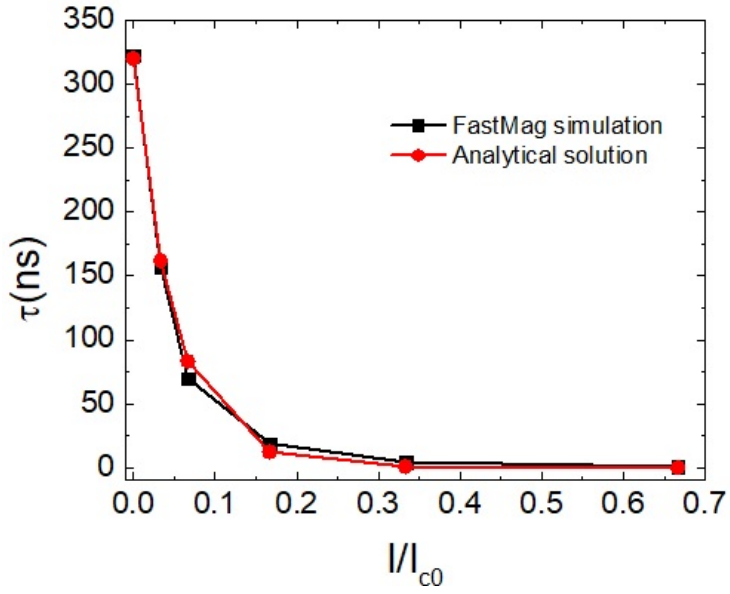

Figure 6.4: Thermal relaxation time of an ellipse calculated from the forward flux sampling and analytical formula. The model used for finite elements simulations is an ellipse with radii of 20nm and 15nm and an energy barrier of $12.9 k_B T$. The computed thermal activation time is $\tau_0 = 8 \times 10^{-4}$ns and $\alpha = 1.6$.

6.3 Conclusion

We have shown that the forward flux sampling is an efficient method to compute the parameters defining the properties of the thermal activated reversal of free-layers, both in a simple macrospin model and for more complex models such as ellipses with domain-wall propagation reversal. While the NEB method is very efficient to find the energy barriers, the forward flux sampling method can be used to get the attempt frequency and the power of the current dependence of the thermal activation time.

Chapter 7

Conclusion

Through this work we have explored different areas related to spin-currents-powered devices such as magnetoresistive random access memories or racetrack memories, mainly looking at ways to tune their behavior under an applied current or ways to improve their thermal properties. A special type of racetrack memory involving antiferromagnetic coupling was analyzed. Several components of spin-valves were studied, including their reaction to the introduction of Dzialoshinskii-Moriya interactions in the system and the impact on switching efficiency induced by free-layers with composite magnetocrystalline anisotropy. Finally, the forward flux sampling method to study the switching properties of spin-valves under non-zero temperature was described.

In the field of magnetic nanotechnologies, micromagnetic simulations are essential to the research and design processes. Indeed, they are the fastest and cheapest way to test new ideas and get quick answers to complex questions. The continued development of micromagnetic simulation softwares, implementation of new interactions and increase in computing power are a sign that these methods will become even more important in the future.

Bibliography

[1] M. Kuteifan, M. V. Lubarda, S. Fu, R. Chang, M. A. Escobar, S. Mangin, E. E. Fullerton, and V. Lomakin, "Large exchange-dominated domain wall velocities in antiferromagnetically coupled nanowires," *AIP Advances*, vol. 6, 2016.

[2] J. Sampaio, A. V. Khvalkovskiy, M. Kuteifan, M. Cubukcu, D. Apalkov, V. Lomakin, V. Cros, and N. Reyren, "Disruptive effect of dzyaloshinskii-moriya interaction on the magnetic memory cell performance," *Appl. Phys. Lett.*, vol. 108, 2016.

[3] W. F. Brown, *Micromagnetics*. Krieger Pub Co, 1978.

[4] L. Landau and E. Lifschitz, "On the theory of the dispersion of magnetic permeability in ferromagnetic bodies," *Phys. Z. Sowjet.*, vol. 8, no. 153, p. 101, 1935.

[5] T. Gilbert, "A phenomenological theory of damping in ferromagnetic materials," *IEEE Trans. on Magn.*, vol. 40, p. 3443, 2004.

[6] D. V. Berkov, "Magnetization dynamics including thermal fluctuations: Basic phenomenology, fast remagnetization processes and transitions over high-energy barriers," *Handbook of Magnetism and Advanced Magnetic Materials*, vol. 2, 2007.

[7] A. Iserles, *A First Course in the Numerical Analysis of Differential Equations*. Cambridge texts in Applied Mathematics, 1996.

[8] U. M. Ascher and L. R. Petzold, *Computer Methods for Ordinary Differential Equations and Differential-Algebraic Equations*. SIAM, 1998.

[9] R. Moskowitz and E. D. Torre, "Theoretical aspects of demagnetization tensors," *IEEE Trans. on Magn.*, vol. 2, p. 739, 1966.

[10] A. Aharoni, "Demagnetizing factors for rectangular ferromagnetic prisms," *J. Appl. Phys.*, vol. 83, p. 3432, 1998.

[11] S. Li, B. Livshitz, and V. Lomakin, "Graphics processing unit accelerated o(n) micromagnetic solver," *IEEE Trans. on Magn.*, vol. 46, no. 6, 2010.

[12] B. Livshitz, A. Boag, H. N. Bertram, and V. Lomakin, "Non-uniform grid algorithm for fast calculation of magnetostatic interactions in micromagnetics," *J. Appl. Phys.*, vol. 105, 2009.

[13] A. Boag and B. Livshitz, "Adaptive nonuniform grid (ng) algorithm for fast capacitance extraction," *IEEE Trans. Microw. Theory Tech.*, vol. 54, p. 3365, 2006.

[14] S. Fu, R. Chang, S. Couture, M. Menarini, M. A. Escobar, M. Kuteifan, M. Lubarda, D. Gabay, and V. Lomakin, "Micromagnetics on high-performance workstation and mobile computational platforms," *J. Appl. Phys.*, vol. 117, no. 17.

[15] NVIDIA, *Compute Unified Device Architecture Programming Guide*, 2017.

[16] S. Li, B. Livshitz, and V. Lomakin, "Fast evaluation of helmholtz potential on graphics processing units (gpus)," *J. of Comp. Phys.*, vol. 229, no. 22, p. 8463, 2010.

[17] M. DAquino, *Nonlinear Magnetization Dynamics in Thin-films and Nanoparticles. PhD thesis*, 2004.

[18] S. S. P. Parkin, N. More, and K. P. Roche, "Oscillations in exchange coupling and magnetoresistance in metallic superlattice structures - co/ru, co/cr, and fe/cr," *Phys. Rev. Let.*, vol. 64, no. 19, 1990.

[19] P. Bruno and C. Chappert, "Ruderman-kittel theory of oscillatory interlayer exchange coupling," *Phys. Rev. B*, vol. 46, no. 1, 1992.

[20] J. Unguris, R. J. Celotta, and D. T. Pierce, "Observation of 2 different oscillation periods in the exchange coupling of fe/cr/fe(100)," *Phys. Rev. Let.*, vol. 67, no. 1, 1991.

[21] T. N. G. Meier, M. Kronseder, and C. H. Back, "Domain-width model for perpendicularly magnetized systems with dzyaloshinskii-moriya interaction," *Phys. Rev. B*, vol. 96, 2017.

[22] S. Middelhoek, "Domain walls in thin nife films," *J. Appl. Phys.*, vol. 34, 1963.

[23] V. D. Nguyen, O. Fruchart, S. Pizzini, J. Vogel, J.-C. Toussaint, and N. Rougemaille, "Third type of domain wall in soft magnetic nanostrips," *Sci. Rep.*, vol. 5, 2015.

[24] K. Yakushiji, S. Yuasa, T. Nagahama, A. Fukushima, H. Kubota, T. Katayama, and K. Ando, "Spin-transfer switching and thermal stability in an fept/au/fept nanopillar prepared by alternate monatomic layer deposition," *Appl. Phys. Exp.*, vol. 1, 2008.

[25] S. S. P. Parkin, M. Hayashi, and L. Thomas, "Magnetic domain-wall racetrack memory," *Science*, vol. 320, 2008.

[26] M. Hayashi, L. Thomas, B. Moriya, C. Rettner, and S. S. P. Parkin, "Current-controlled magnetic domain-wall nanowire shift register," *Science*, vol. 350, 2008.

[27] D. A. Allwood, G. Xiong, M. D. Cooke, C. C. Faulkner, D. Atkinson, N. Vernier, and R. Cowburn, "Submicrometer ferromagnetic not gate and shift register," *Science*, vol. 296, 2002.

[28] D. A. Allwood, G. Xiong, C. C. Faulkner, D. Atkinson, D. Petit, and R. Cowburn, "Magnetic domain-wall logic," *Science*, vol. 309, 2005.

[29] D. A. Allwood, G. Xiong, and R. Cowburn, "Magnetic domain wall serial-in parallel-out shift register," *App. Phys. Let.*, vol. 89, 2006.

[30] D. J. Dunlop and O. Ozdemir, *Rock Magnetism, Cambridge Studies in Magnetism*, p. 52, 1997.

[31] D. A. Garanin, "Fokker-planck and landau-lifshitz-bloch equations for classical ferromagnets," *Phys. Rev. B*, vol. 55, no. 5, 1997.

[32] N. Kazantseva, D. Hinzke, U. Nowak, R. W. Chantrell, U. Atxitia, and O. Chubykalo-Fesenko, "Towards multiscale modeling of magnetic materials: Simulations of fept," *Phys. Rev. B*, vol. 77, no. 18, 2008.

[33] J. Barker, R. F. L. Evans, R. W. Chantrell, D. Hinzke, and U. Nowak, "Atomistic spin model simulation of magnetic reversal modes near the curie point," *Appl. Phys. Lett.*, vol. 97, 2010.

[34] T. Bose, R. Cuadrado, R. F. L. Evans, R. V. Chepulskii, D. Apalkov, and R. W. Chantrell, *J. Phys. Condens. Mat.*, vol. 28, 2016.

[35] D. V. Berkov, "Numerical calculation of the energy barrier distribution in disordered many-particle systems: the path integral method," *J. Magn. Magn. Mat*, vol. 186, no. 1, p. 199, 1998.

[36] E. Paz, F. Garcia-Sanchez, and O. Chubykalo-Fesenko, "Numerical evaluation of energy barriers in nano-sized magnetic elements with lagrange multiplier technique," *Phys. B: Cond. Mat.*, vol. 403, no. 2, p. 330, 2008.

[37] D. Sheppard, R. Terrell, and G. Henkelman, "Optimization methods for finding minimum energy paths," *J. Chem. Phys.*, vol. 128, no. 13, p. 134, 2008.

[38] H. Jónsson, G. Mills, and K. W. Jacobsen, "Nudged elastic band method for finding minimum energy paths of transitions," *Classical And Quantum Dynamics In Condensed Phase Simulations, World Scientific, Singapore*, 1998.

[39] G. Henkelman, B. P. Uberuaga, and H. Jónsson, "A climbing image nudged elastic band method for finding saddle points and minimum energy paths," *J. Chem. Phys.*, vol. 113, no. 22, p. 9901, 2000.

[40] P. Maragakis, S. A. Andreev, Y. Brumer, D. R. Reichman, and E. Kaxiras, "Adaptive nudged elastic band approach for transition state calculation," *J. Chem. Phys.*, vol. 117, p. 4651, 2002.

[41] R. Dittrich, T. Schrefl, A. Thiaville, J. Miltat, V. Tsiantos, and J. Fidler, "Comparison of langevin dynamics and direct energy barrier computation," *J. Magn. Magn. Mat.*, vol. 272, p. 747, 2004.

[42] S. Zhang and Z. Li, "Roles of nonequilibrium conduction electrons on the magnetization dynamics of ferromagnets," *Phys. Rev. Lett.*, vol. 93, no. 12, 2004.

[43] A. Thiaville, Y. Nakatani, J. Miltat, and Y. Suzuki, "Micromagnetic understanding of current-driven domain wall motion in patterned nanowires," *Europhys. Lett.*, vol. 69, no. 6, 2005.

[44] C. Burrowes, A. P. Mihai, D. Ravelosona, J.-V. Kim, C. Chappert, L. Vila, A. Marty, Y. Samson, F. Garcia-Sanchez, L. D. Buda-Prejbeanu, I. Tudosa, E. E. Fullerton, and J.-P. Attan, "Non-adiabatic spin-torques in narrow magnetic domain walls," *Nature Phys.*, no. 6, p. 17, 2010.

[45] S.DuttaGupta, S. Fukami, C. Zhang, H. Sato, M. Yamanouchi, F. Matsukura, and H. Ohno, "Adiabatic spin-transfer-torque-induced domain wall creep in a magnetic metal," *Nature Phys.*, vol. 12, p. 333, 2016.

[46] G. Tatara and H. Kohno, "Theory of current-driven domain wall motion: Spin transfer versus momentum transfer," *Phys. Rev. Lett.*, vol. 92, no. 8, 2004.

[47] G. Tatara, H. Kohno, and J. Shibata, "Theory of domain wall dynamics under current," *J. Phys. Soc. Jpn.*, vol. 77, 2008.

[48] J. Xiao, A. Zangwill, and M. D. Stiles, "Spin-transfer torque for continuously variable magnetization," *Phys. Rev. B*, no. 73, 2006.

[49] A. Vanhaverbeke and M. Viret, "Simple model of current-induced spin torque in domain walls," *Phys. Rev. B*, vol. 75, 2007.

[50] A. Malozemo and J. Slonczewski, *Magnetic domain walls in bubble materials*. Academic Press, 1979.

[51] G. Beach, C. Nistor, C. Knutson, M. Tsoi, and J. Erskine, "Dynamics of field-driven domain-wall propagation in ferromagnetic nanowires," *Nature Mat.*, vol. 4, 2005.

[52] E. Salhi and L. Berger, "Currentinduced displacements and precession of a bloch wall in nife thin films," *J. Appl. Phys.*, vol. 73, 1993.

[53] J. Slonczewski, "Current-driven excitation of magnetic multilayers," *J. Magn. Magn. Mat*, vol. 159, 1996.

[54] L. Berger, "Emission of spin waves by a magnetic multilayer traversed by a current," *Phys. Rev. B*, vol. 54, p. 9353, 1996.

[55] D. C. Ralph and M. D. Stiles, "Spin transfer torques," *J. Magn. Magn. Mat.*, vol. 320, p. 1190, 2008.

[56] N. Schryer and J. Walker, "The motion of 180 domain walls in uniform dc magnetic fields," *J. Appl. Phys.*, vol. 45, p. 5406, 1974.

[57] I. Miron, T. Moore, H. Szambolics, L. Buda-Prejbeanu, S. Auffret, B. Rodmacq, S. Pizzini, J. Vogel, M. Bonfim, A. Schuhl, and G. Gaudin, "Fast current-induced domain-wall motion controlled by the rashba effect," *Nature Mat.*, vol. 10, p. 419, 2011.

[58] M. Yan, C. Andreas, A. Kkay, F. Garca-Snchez, and R. Hertel, "Fast domain wall dynamics in magnetic nanotubes: Suppression of walker breakdown and cherenkov-like spin wave emission," *Appl. Phys. Lett.*, vol. 99, 2011.

[59] H. Saarikoski, H. Kohno, C. H. Marrows, and G. Tatara, "Beating the walker limit with massless domain walls in cylindrical nanowires," *Phys. Rev. Lett.*, vol. 104, 2010.

[60] T. Schrefl, D. Atkinson, and D. A. Allwood, "Magnetic domain wall propagation in nanowires under transverse magnetic fields," *J. Appl. Phys.*, vol. 103, 2008.

[61] S. Parkin, L. Thomas, and S.-H. Yang, "Domain wall motion in perpendicularly magnetized wires having artificial antiferromagnetically coupled multilayers with engineered interfaces," *US patent*, vol. 8,687,415 B2, 2014.

[62] Y. Saad and M. H. Schultz, "Gmres: A generalized minimal residual algorithm for solving nonsymmetric linear systems," *SIAM J. Sci. and Stat. Comput*, vol. 7, 1986.

[63] Y. Saad, *Iterative Methods for Sparse Linear Systems, 2nd edition, Society for Industrial and Applied Mathematics*. Society for Industrial and Applied Mathematics, 2003.

[64] R. Chang, S. Li, M. Lubarda, B. Livshitz, and V. Lomakin, "Fastmag: Fast micromagnetic simulator for complex magnetic structures," *J. Appl. Phys.*, vol. 109, 2011.

[65] M. Donahue and D. Porter, "Oommf user's guide," *Interagency Report NISTIR*, vol. 6376, 1999.

[66] A. Mougin, M. Cormier, J. P. Adam, P. J. Metaxas, and J. Ferr, "Domain wall mobility, stability and walker breakdown in magnetic nanowires," *Europhys. Lett.*, vol. 78, no. 5, 2007.

[67] D. G. Porter and M. J. Donahue, "Velocity of transverse domain wall motion along thin, narrow strips," *J. Appl. Phys.*, vol. 95, 2004.

[68] E. Pardo, D.-X. Chen, and A. Sanchez, "Demagnetizing factors for square bars," *IEEE transaction on magnetics*, vol. 40, 2004.

[69] A. Thiaville, Y. Nakatani, J. Miltat, and N. Vernier, "Domain wall motion by spin-polarized current: a micromagnetic study," *J. Appl. Phys.*, vol. 95, no. 11, 2004.

[70] A. Fert, V. Cros, and J. Sampaio, "Skyrmions on the track," *Nature Nanotech.*, vol. 8, p. 152, 2013.

[71] A. Fert, N. Reyren, and V. Cros, "Magnetic skyrmions: advances in physics and potential applications," *Nature Rev. Mat.*, vol. 2, 2017.

[72] R. E. F. J. R. Childres and, "Magnetic recording read head sensor technology," *Comptes rendus - Phys.*, vol. 6, no. 9, p. 997, 2005.

[73] A. V. Khvalkovskiy, D. Apalkov, S. Watts, R. Chepulskii, R. S. Beach, A. Ong, X. Tang, A. Driskill-Smith, W. Butler, and P. Visscher, "Basic principles of stt-mram cell operation in memory arrays," *J. Phys. D: App. Phys.*, vol. 13, 2013.

[74] T. Valet and A. Fert, "Theory of the perpendicular magnetoresistance in magnetic multilayers," *Phys. Rev. B*, vol. 48, 1993.

[75] J. Xiao, A. Zangwill, and M. D. Stiles, "Macrospin models of spin transfer dynamics," *Phys. Rev. B*, vol. 72, no. 1, 2005.

[76] S. Mangin, D. Ravelosona, J. A. Katine, M. J. Carey, B. D. Terris, and E. E. Fullerton, "Current-induced magnetization reversal in nanopillars with perpendicular anisotropy," *Nature Mat.*, vol. 5, p. 210, 2006.

[77] S. Mangin, Y. Henry, D. Ravelosona, J. A. Katine, and E. E. Fullerton, "Reducing the critical current for spin-transfer switching of perpendicularly magnetized nanomagnets," *Appl. Phys. Lett.*, vol. 94, 2009.

[78] D. Houssameddine, U. Ebels, B. Delaët, B. Rodmacq, I. Firastrau, F. Ponthenier, M. Brunet, C. Thirion, J.-P. Michel, L. Prejbeanu-Buda, M.-C. Cyrille, O. Redon, and B. Dieny, "Spin-torque oscillator using a perpendicular polarizer and a planar free layer," *Nature Mat.*, vol. 6, p. 447, 2007.

[79] Z. Zeng, G. Finocchio, B. Zhang, P. K. Amiri, J. A. Katine, I. N. Krivorotov, Y. Huai, J. Langer, B. Azzerboni, K. L. Wang, and H. Jiang, "Ultralow-current-density and bias-field-free spin-transfer nano-oscillator," *Scientific Reports 3*, vol. 3, no. 1426, 2013.

[80] S. Mangin, G. Marchal, C. Bellouard, W. Wernsdorfer, and B. Barbara, "Magnetic behavior and resistivity of the domain-wall junction gdfe(1000 å)/tbfe/gdfe(500 å)," *Phys. Rev. B*, vol. 58, no. 5, 1998.

[81] E. E. Fullerton, J. S. Jiang, M. Grimsditch, C. H. Sowers, and S. D. Bader, "Exchange-spring behavior in epitaxial hard/soft magnetic bilayers," *Phys. Rev. B*, vol. 58, 1998.

[82] N. Supper, D. Margulies, A. Moser, A. Berger, H. Do, and E. Fullerton, "Writability enhancement using exchange spring media," *IEEE Trans. on Magn.*, vol. 41, no. 10, p. 3238, 2005.

[83] E. E. Fullerton, H. V. Do, D. T. Margulies, and N. Supper, "Incoherently-reversing magnetic laminate with exchange coupled ferromagnetic layers," *U.S. patent 7,425,377*, 2008.

[84] R. Victora and X. Shen, "Exchange coupled composite media for perpendicular magnetic recording," *IEEE Trans. on Magn.*, vol. 41, no. 10, p. 2828, 2005.

[85] D. Suess, T. Schre, M. Kirschner, G. Hrkac, F. Dorfbauer, , and F. Fider, "Exchange spring media for perpendicular recording," *Appl. Phys. Lett.*, vol. 87, 2005.

[86] I. Yulaev, M. V. Lubarda, S. Mangin, V. Lomakin, and E. E. Fullerton, "Spin-transfer-torque reversal in perpendicular anisotropy spin valves with composite free layers," *Appl. Phys. Lett.*, vol. 99, 2011.

[87] A. Y. Dobin and H. J. Richter, "Domain wall assisted magnetic recording," *Appl. Phys. Lett.*, vol. 89, 2006.

[88] D. Goll, S. Macke, and H. Krönmller, "Exchange coupled composite layers for magnetic recording," *Phys. B*, vol. 403, no. 2, p. 338, 2008.

[89] S.-S. Yan, R. Schreiber, P. Grünberg, and R. Schäfer, "Magnetization reversal in (0 0 1)fe thin films studied by combining domain images and moke hysteresis loops," *J. Magn. Magn. Mat.*, vol. 210, no. 1, p. 309, 2000.

[90] J.-P. Wang, W. K. Shen, J. M. Bai, R. H. Victora, J. H. Judy, and W. L. Song, "Composite media (dynamic tilted media) for magnetic recording," *Appl. Phys. Lett.*, vol. 86, 2005.

[91] K.Mibu, T.Nagahama, and T.Shinjo, "Reversible magnetization process and magnetoresistance of soft-magnetic (nife) /hard-magnetic (cosm) bilayers," *J. Magn. Magn. Mat.*, vol. 163, no. 1, p. 75, 1996.

[92] D.Suess, J. Lee, J.Fidler, and T.Schrefl, "Exchange-coupled perpendicular media," *J. Magn. Magn. Mat.*, vol. 321, no. 6, p. 545, 2009.

[93] J. Z. Sun, S. L. Brown, W. Chen, E. A. Delenia, M. C. Gaidis, J. Harms, G. Hu, X. Jiang, R. Kilaru, W. Kula, G. Lauer, L. Q. Liu, S. Murthy, J. Nowak, E. J. OSullivan, S. S. P. Parkin, R. P. Robertazzi, P. M. Rice, G. Sandhu, T. Topuria, and D. C. Worledge, "Spin-torque switching efficiency in cofeb-mgo based tunnel junctions," *Phys. Rev. B*, vol. 88, 2013.

[94] I. Tudosa, J. A. Katine, S. Mangin, and E. E. Fullerton, "Perpendicular spin-torque switching with a synthetic antiferromagnetic reference layer," *Appl. Phys. Lett.*, vol. 96, 2010.

[95] L. M. Sandratskii, "Insight into the dzyaloshinskii-moriya interaction through first-principles study of chiral magnetic structures," *Phys. Rev. B*, vol. 96, 2017.

[96] N. Nagaosa and Y. Tokura, "Topological properties and dynamics of magnetic skyrmions," *Nature Nanotech.*, vol. 8, p. 899, 2013.

[97] M. Jalil, S. Tan, Z. Siu, W.Gan, I.Purnama, and W.S.Lew, "Stability of topological charge of magnetic skyrmion configurations," *J. Magn. Magn. Mat.*, vol. 399, p. 155, 2016.

[98] R. Ozawa, S. Hayami, and Y. Motome, "Zero-field skyrmions with a high topological number in itinerant magnets," *Phys. Rev. Lett.*, vol. 118, 2017.

[99] A. Fert, *Magnetic and Transport Properties of Metallic Multilayers*. Materials Science Forum, 1990, vol. 59.

[100] A. Fert and P. M. Levy, "Role of anisotropic exchange interactions in determining the properties of spin-glasses," *Phys. Rev. Lett.*, vol. 44, 1980.

[101] S. Heinze, K. von Bergmann, M. Menzel, J. Brede, A. Kubetzka, R. Wiesendanger, G. Bihlmayer, and S. Blügel, "Spontaneous atomic-scale magnetic skyrmion lattice in two dimensions," *Nature Phys.*, vol. 7, p. 713, 2011.

[102] A. Thiaville, S. Rohart, E. Jué, V. Cros, and A. Fert, "Dynamics of dzyaloshinskii domain walls in ultrathin magnetic films," *Europhys. Lett.*, vol. 100, no. 5, p. 57002, 2012.

[103] J. Sampaio, V. Cros, S. Rohart, A. Thiaville, and A. Fert, "Nucleation, stability and current-induced motion of isolated magnetic skyrmions in nanostructures," *Nature Nanotech.*, vol. 8, p. 839, 2013.

[104] S. Rohart and A. Thiaville, "Skyrmion confinement in ultrathin film nanostructures in the presence of dzyaloshinskii-moriya interaction," *Phys. Rev. B*, vol. 88, 2013.

[105] A. Vansteenkiste, J. Leliaert, M. Dvornik, M. Helsen, F. Garcia-Sanchez, and B. V. Waeyenberge, "The design and verification of mumax3," *AIP Advances*, vol. 4, 2014.

[106] G. J. Vida, E. Simon, L. Rózsa, K. Palotás, and L. Szunyogh, "Domain-wall profiles in co/ir/pt(111) ultrathin films: Influence of the dzyaloshinskii-moriya interaction," *Phys. Rev. B*, vol. 94, 2016.

[107] M. D. DeJong and K. L. Livesey, "Domain walls in finite-width nanowires with interfacial dzyaloshinskii-moriya interaction," *Phys. Rev. B*, vol. 95, 2017.

[108] S. Emori, E. Martinez, K.-J. Lee, H.-W. Lee, U. Bauer, S.-M. Ahn, P. Agrawal, D. C. Bono, and G. S. D. Beach, "Spin hall torque magnetometry of dzyaloshinskii domain walls," *Phys. Rev. B*, vol. 90, 2014.

[109] H.-J. Suh, C. Heo, C.-Y. You, W. Kim, T.-D. Lee, and K.-J. Lee, "Attempt frequency of magnetization in nanomagnets with thin-film geometry," *Phys. Rev. B*, vol. 78, 2008.

[110] G. Fiedler, J. Fidler, J. Lee, T. Schrefl, R. L. Stamps, H. B. Braun, and D. Suess, "Direct calculation of the attempt frequency of magnetic structures using the finite element method," *J. App. Phys.*, vol. 111, 2012.

[111] R. J. Allen, D. Frenke, and P. R. ten Wolde, "Forward flux sampling-type schemes for simulating rare events: Efficiency analysis," *J. Chem. Phys.*, vol. 124, 2006.

[112] R. J. Allen, C. Valeriani, and P. R. ten Wolde, "Forward flux sampling for rare event simulations," *J. Phys.: Cond. Mat.*, vol. 21, no. 46, 2009.

[113] C. Vogler, F. Bruckner, D. Suess, and C. Dellago, "Calculating thermal stability and attempt frequency of advanced recording structures without free parameters," *J. App. Phys.*, vol. 117, 2015.